

© 2010 Reza Abedi

SPACETIME DAMAGE-BASED COHESIVE MODEL FOR
ELASTODYNAMIC FRACTURE WITH DYNAMIC CONTACT

BY

REZA ABEDI

DISSERTATION

Submitted in partial fulfillment of the requirements
for the degree of Doctor of Philosophy in Theoretical and Applied Mechanics
in the Graduate College of the
University of Illinois at Urbana-Champaign, 2010

Urbana, Illinois

Doctoral Committee:

Professor Robert Haber, Chair
Professor Glaucio H. Paulino
Associate Professor Gustavo Gioia
Assistant Professor C. Armando Duarte

Abstract

Dynamic material failure is important in a number of scientific and engineering applications and a variety of numerical methods for its modeling have been proposed. This thesis presents the formulation and implementation of an interfacial-damage, cohesive-fracture model, including contact and friction effects, for dynamic failure of brittle materials. The model is implemented within a spacetime discontinuous Galerkin (SDG) finite element method. An adaptive meshing procedure generates spacetime grids that satisfy a special *causality constraint* to enable an efficient patch-by-patch, advancing-front solution scheme with $\mathcal{O}(N)$ computational complexity. Per-element balance properties, local adaptive operations, and the use of Riemann fluxes provide to the SDG method the extreme accuracy and efficiency required to solve multiscale fracture problems.

A dimensional analysis of linear elastodynamics, with extensions to fracture models based on cohesive traction–separation laws, supports the formulation. The problem is formulated and analyzed using differential forms and the exterior calculus in spacetime. The analysis demonstrates that the velocity scalings implied by the spatial and temporal coordinate scalings and by the scalings of the material properties must be identical to obtain a self-similar scaling of an elastodynamic process. The use of differential forms reveals intrinsic structure and relations between the spacetime mechanics fields which are otherwise obscured by conventional tensorial analysis. For example, only four distinct scalings are required to define a scaled elastodynamic process when we work directly with forms, while eight are required when tensorial analysis is used. In the context of dynamic cohesive fracture, the analysis shows that, among the nondimensional variables, the ratio of the stress-loading scale to the cohesive strength is proportional to the ratio of the radius of the singularity-dominant zone from Linear Elastodynamic Fracture Mechanics (LEFM), to the cohesive-process-zone size. These ratios

are, in turn, useful indicators of whether the small-scale-yielding caveat of LEFM is satisfied.

A novel continuum formulation of the linear elastodynamic contact problem also supports the SDG finite element model. In contrast to previous contact models that invoke quasi-static contact conditions, the proposed model enforces dynamic contact conditions by prescribing momentum flux and compatibility conditions obtained from the local Riemann problems for bonded, separation, contact–stick, and contact–slip modes. This approach preserves the characteristic structure of the underlying equations at the contact interface, a property that is lacking in previous formulations. The fully-bonded and contact–stick conditions are identical, as expected, so the non-penetration and tangential slip constraints are treated exactly in the new continuum formulation. Furthermore, the direction of the tangential contact traction (friction) is shown to be continuous through transitions between contact–stick and contact-slip modes. These favorable properties, which improve the accuracy of and facilitate numerical implementations of the proposed model, are not obtained in many existing models which, for example, replace the non-penetration constraint with a large interfacial stiffness in the normal direction. The transition between separation and contact modes retains its physically discontinuous character, and a regularization of this transition is introduced to facilitate and reduce the cost of numerical implementations. A discretization and numerical implementation within the adaptive SDG framework demonstrate the effectiveness of the new contact model in a numerical setting.

A new two-scale cohesive fracture model replaces the usual traction-separation law with a damage model that represents mesoscale processes of void growth and coalescence. The evolution of a single damage parameter D , which represents the debonded area fraction on cohesive interfaces, is governed by an irreversible, time-delay evolution law characterized by a cohesive strength and a relaxation time τ that determines the maximum damage rate. Riemann fluxes for the fully-bonded condition are enforced in the undamaged area fraction $(1 - D)$ of the cohesive interface, while the Riemann fluxes for the contact–stick, contact–slip or separation conditions determine the fluxes in the debonded area fraction. These mesoscale Riemann values are averaged to derive macroscopic cohesive conditions. The damage-based cohesive model is implemented within the adaptive SDG fi-

nite element framework to produce a numerical model that efficiently and accurately resolves the multi-scale response associated with dynamic fracture and transitions between contact, separation, stick and slip conditions in the event of crack closure. Beyond ensuring solution accuracy, the model uses the SDG scheme's adaptive meshing capabilities to freely nucleate and extend cohesive interfaces to capture solution-dependent crack paths. The SDG adaptive meshing aligns the boundaries of spacetime elements with crack-path trajectories having arbitrary position and orientation, and two adaptive error indicators ensure the accurate rendering of both the cohesive model and the bulk solution. Thus, the present model does not suffer the limited resolution and mesh-dependent effects encountered in most other numerical fracture models. Numerical results obtained with the proposed model demonstrate crack propagation, microcrack formation and crack branching phenomena.

To my parents

Acknowledgments

I would like to express my gratitude to Professor Robert Haber for serving as my advisor and providing guidance, mentorship, and motivation for this work. I would also like to acknowledge Professors Glaucio Paulino, Gustavo Gioia, and Armando Duarte for serving on my committee.

I would also thank my fellow graduate students: Scott Miller, Jayandran Palaniappan, Yong Fan, Morgan Hawker and Boris Petracovici. They have provided invaluable advice, and collaborations during my PhD research projects. I would also like to acknowledge Professors Jeff Erickson and Michael Garland and their graduate students for their work on spacetime meshing and visualization.

I am enormously grateful to my parents for their continuous encouragement specifically through my academic education. I could not have fulfilled my promises without their support.

I gratefully acknowledge financial support from the Center for Process Simulation & Design, University of Illinois at Urbana Champaign under U.S. National Science Foundation grants DMR-01-21695 and DMR 03-25939.

Table of Contents

List of Figures	ix
Chapter 1 Introduction	1
Chapter 2 Spacetime dimensional analysis of linear elasto- dynamics and cohesive, dynamic fracture	4
2.1 Introduction	4
2.2 Formulation	6
2.3 Dimensional analysis	18
2.4 Comparative analyses of cohesive and linear elastic models of dynamic fracture	27
2.5 Numerical parametric study of the CFM model	37
2.6 Conclusions	51
Chapter 3 Riemann conditions for elastodynamic contact with SDG implementation	54
3.1 Introduction	54
3.2 Formulation	58
3.3 Spacetime discontinuous Galerkin formulation and implemen- tation	80
3.4 Numerical results	84
3.5 Conclusions	91
Chapter 4 A two-scale, delayed-damage cohesive model for dynamic fracture and contact problems	95
4.1 Introduction	95
4.2 Formulation	98
4.3 Probabilistic crack growth in brittle solids with random defects	105
4.4 Spacetime discontinuous Galerkin discretization and imple- mentation	110
4.5 Numerical results	120
4.6 Conclusions	124
Chapter 5 Conclusion	136

Author's Biography	140
References	141

List of Figures

2.1	Cylindrical spacetime domain and boundary partition for $d = 2$.	14
2.2	Local coordinate system on a vertical 2-manifold.	16
2.3	Local coordinate system at a crack tip.	28
2.4	Infinite domain containing a half-plane crack.	38
2.5	Cohesive model for middle-crack tension specimen.	43
2.6	Crack-tip velocity histories and trajectories for low-amplitude loads.	46
2.7	Early stages of crack-tip velocity histories and trajectories for low-amplitude loads.	47
2.8	Crack-tip velocity histories and trajectories for high-amplitude loads.	48
2.9	Evolution of energy release rate as a function of load amplitude.	49
2.10	Evolution of cohesive process zone size.	50
3.1	Alternative partitions of $\partial\mathcal{Q}$.	60
3.2	The local coordinate system at a jump manifold.	61
3.3	Riemann problem with data prescribed on only one side of a vertical material interface.	65
3.4	Riemann problem with distinct initial data on opposing sides, α and β , of a material interface Γ .	66
3.5	Traction and velocity vectors on opposite sides of an interface in the contact–slip mode.	69
3.6	Sectors with distinct Riemann solutions used to classify the inclination of a d -manifold Γ with arbitrary orientation.	73
3.7	Mesoscale contact-mode hierarchy and area fractions in the neighborhood $N(\mathbf{x})$ of a macroscopic location $\mathbf{x} \in \tilde{\Gamma}$.	76
3.8	Identification and regularization of the contact and separation modes.	77
3.9	Geometry and load description for contact/separation example.	85
3.10	The solution on contact interface for $r_c = -10^{-3}$ mm, $r_s = 0$, $s^c = 0$, and $s^s = 600$ kPa.	86
3.11	The solution on contact interface for $r_c = -10^{-4}$ mm, $r_s = 0$, $s^c = 0$, and $s^s = 60$ kPa.	88

3.12	Geometry and load description for contact stick and slip example.	90
3.13	Visualization of slip along the contact surface on the deformed geometry.	92
4.1	Mesoscale region hierarchy for the combined damage–contact model.	99
4.2	Probability density function for nucleation strength at defects.	106
4.3	The crack propagation criterion.	108
4.4	The extension of a crack in the space mesh through refinement and tent pitching operations.	116
4.5	The influence of the relative values of $\tilde{\sigma}_0$ and $\tilde{\sigma}_0^d$ on crack propagation pattern.	117
4.6	The coarsening operation on completely damaged ($D = 1$) edges of a crack.	119
4.7	Schematic representation of the geometry and boundary condition for the study of crack propagation in PMMA.	121
4.8	Crack propagation on the space mesh versus the number of patches for $\tilde{\tau} = 10^{-2} \mu s$	125
4.9	The details of the crack path around the microcrack events at $t \approx 4.96 \mu s$ for $\tilde{\tau} = 10^{-2} \mu s$	128
4.10	The crack propagation on the space mesh versus the number of patches for $\tilde{\tau} = 10^{-3} \mu s$	130
4.11	The details of the crack path at $t \approx 2.05 \mu s$ for $\tilde{\tau} = 10^{-3} \mu s$	133
4.12	Crack path at $t = 2.05 \mu s$ on deformed geometry for $\tilde{\tau} = 10^{-3} \mu s$.	134

Chapter 1

Introduction

Dynamic material failure is important in a number of scientific and engineering applications, including earthquake modeling [1] semiconductor chip manufacturing processes [2], impact and fragmentation studies [3], armor engineering [4], delamination of composite materials [5], and bone fracture [6]. A variety of numerical methods for modeling dynamic fracture have been proposed. *Cohesive* models are among the most effective, and are currently the most popular, class of continuum numerical models for dynamic fracture. In contrast to smeared damage models, cohesive fracture models represent crack surfaces as sharp material interfaces. They simulate crack initiation and extension by modeling the macroscopic effects of various nonlinear damage processes in the neighborhood of the crack tip. In this work, we study two general classes of cohesive models; those based on a *traction-separation relation*(TSR) and a new interfacial damage-based cohesive model.

In chapter 2 we present a dimensional analysis for linear elastodynamic problem. We express the governing equations in spacetime setting using differential form notation. The analysis demonstrates that the velocity scalings implied by the spatial and temporal coordinate scalings and by the scalings of the material properties must be identical to obtain a self-similar scaling of an elastodynamic process. The use of differential forms reveals intrinsic structure and relations between the spacetime mechanics fields which are otherwise obscured by conventional tensorial analysis. For example, only four distinct scalings are required to define a scaled elastodynamic process when we work directly with forms, while eight are required when tensorial analysis is used.

We specialize the dimensional analysis to cohesive elastodynamic fracture problem where the TSR, describes the tractions acting across a cohesive interface as nonlinear, bounded functions of the interface separation. We derive the dimensional scales such as length, time, and velocity that are

associated with the cohesive model. Finally, we present all the mechanical fields in terms of the nondimensional parameters derived from the cohesive scales.

Next, we present an analysis of the cohesive models within the *Linear Elastic Fracture Mechanics* (LEFM) framework. The mathematically sharp crack tips within LEFM theory result in singular stress and velocity fields. Since the material could not withstand infinite stresses, the actual solution deviates from the theory in a zone around the crack tip. Although, LEFM solutions are not valid within this zone, they accurately describe the solution outside this process zone as long as its size is much smaller than dominant radii of singular terms that are obtained from the expansion of the LEFM stress fields. That is, if the *small-scale yielding* (SSY) assumption hold. We show that, among the nondimensional cohesive variables, the ratio of the stress-loading scale to the cohesive strength is proportional to the cohesive process zone size, to the ratio of the radius of singularity from LEFM. These ratios are, in turn, useful indicators of whether the SSY caveat of LEFM is satisfied.

A novel continuum formulation of the linear elastodynamic contact problem along with an implementation in spacetime discontinuous Galerkin (SDG) framework is presented in chapter 3. In contrast to previous contact models that invoke quasi-static contact conditions, the proposed model enforces dynamic contact conditions by prescribing momentum flux and compatibility conditions obtained from the local Riemann problems for bonded, separation, contact–stick, and contact–slip modes. This approach preserves the characteristic structure of the underlying equations at the contact interface, a property that is lacking in previous formulations.

The fully-bonded and contact–stick conditions are identical, as expected, so the non-penetration constraint is treated exactly in the new continuum formulation. This eliminates the problems encountered with penalty methods that attempt to limit interface penetration by employing large penalty values. Furthermore, in contrary to Lagrange multiplier methods, no additional degrees of freedom are augmented to the problem. The transition between separation and contact modes retains its physically discontinuous character, and a regularization of this transition is introduced to facilitate and reduce the cost of numerical implementations. A discretization and numerical implementation within the adaptive SDG framework demonstrate

the effectiveness of the new contact model in a numerical setting.

Any friction relation can be employed to determine the contact-slip solution. Herein, we use the Coulomb’s law of friction to derive the Riemann solutions. The direction of the tangential contact traction (friction) is obtained from the slip velocity at the interface, which results in a discontinuous representation of the slip traction at stick/slip transitions. The discontinuous behavior is removed in our formulation without any modification to the actual form of the Coulomb law. This, for example, eliminates the need for regularization that is necessary in many numerical methods in response to the discontinuous behavior.

In chapter 4, we present a new two-scale interfacial cohesive fracture model where a single damage parameter, D , represents mesoscale processes of void growth and coalescence. The evolution of the damage parameter D , which represents the debonded area fraction on cohesive interfaces, is governed by an irreversible, time-delay evolution law characterized by a cohesive strength and a relaxation time $\tilde{\tau}$ that determines the maximum damage rate. Riemann fluxes for the fully-bonded condition are enforced in the undamaged area fraction $(1 - D)$ of the cohesive interface, while the Riemann fluxes for the contact–stick, contact–slip or separation conditions determine the fluxes in the debonded area fraction. These mesoscale Riemann values are averaged to derive macroscopic cohesive conditions. The damage model is implemented within the adaptive SDG finite element framework.

Beyond ensuring solution accuracy, the model uses the SDG scheme’s adaptive meshing capabilities to freely nucleate and extend cohesive interfaces to capture solution-dependent crack paths. The SDG adaptive meshing aligns the boundaries of spacetime elements with crack-path trajectories having arbitrary position and orientation, and two adaptive error indicators ensure the accurate rendering of both the cohesive model and the bulk solution. Thus, the present model does not suffer the limited resolution and mesh-dependent effects encountered in most other numerical fracture models. Numerical results obtained with the proposed model demonstrate crack propagation, microcrack formation and crack branching phenomena.

Chapter 2

Spacetime dimensional analysis of linear elastodynamics and cohesive, dynamic fracture

2.1 Introduction

In this chapter, we present a dimensional analysis of linear elastodynamics with extensions to dynamic fracture models based on cohesive traction–separation relations. We formulate the problem using differential forms in spacetime and show that the scaling rules expressed in terms of forms are simpler and more uniform than those obtained for tensor representations of the solution.

We extend our dimensional analysis of general elastodynamics to address dynamic fracture models based on cohesive traction–separation relations. We identify certain nondimensional groups, expressed in terms of various elastodynamic and cohesive parameters, that govern the solution. We study the influence of these groups on dynamic fracture behavior and, in particular, show that the ratio of the loading to the cohesive strength governs the relation between the distinct length scales established by the cohesive fracture model and by Linear Elastodynamic Fracture Mechanics (LEFM).

2.1.1 Related work

Cohesive models are among the most effective, and are currently the most popular, class of continuum numerical models for dynamic fracture. They developed from the cohesive zone models first introduced by Dugdale [7] and Barenblatt [8]. In contrast to smeared damage models, cohesive fracture models represent crack surfaces as sharp material interfaces. Cohesive models simulate crack initiation and extension by modeling the macroscopic effects of various nonlinear damage processes in the neighborhood of the crack tip. A constitutive relation, called a *traction–separation relation* (TSR), describes the tractions acting across a cohesive interface as nonlinear, bounded func-

tions of the interface separation.

The mathematically sharp crack tips within *Linear Elastic Fracture Mechanics* (LEFM) theory result in singular stress and velocity fields. Since the material could not withstand infinite stresses, the actual solution deviates from the theory in a zone around the crack tip. Although, LEFM solutions are not valid within this zone, they accurately describe the solution outside this process zone as long as its size is much smaller than dominant radii of singular terms. Plastic deformations or some other form of material yielding describe the solution within this zone. Cohesive models are one of such approaches to eliminate singular stress values [9].

2.1.2 Dimensional analysis of cohesive models and LEFM comparison solution

The dimensional analysis of cohesive fracture enables us to express the solution fields in terms of nondimensional variables. The solution to a problem with particular material properties and cohesive parameters can be easily generalized to a group of self-similar solutions. Moreover, it provided us with characteristic scalings for domain dimensions as well as solution fields.

Herein, we obtain characteristic values associated with cohesive fracture problem. In particular, we obtain characteristic cohesive length and time scales, \tilde{L} and $\tilde{\tau}$ respectively. The former, determines the scaling of domain spatial size as well as cohesive fracture length scales. For example, we demonstrate that cohesive process zone size is proportional to \tilde{L} . The latter, is derived from an equation which relates cohesive separation, $\tilde{\delta}$, strength, $\tilde{\sigma}$, and time scales. In fact, Ortiz *et al.* [10] derived the same value for $\tilde{\tau}$ in the context of spall strength due to varying incident waves. Furthermore, Pandolfi *et al.* [11] observed that $\tilde{\tau}$ influences minimum time step required for a convergent time stepping algorithm.

We also investigate the changes to cohesive characteristic values. For example, we elaborate on self-similar solution groups due to changes to cohesive strength, separation, work of separation, $\tilde{\phi}$, and $\tilde{\tau}$. Moreover, we introduce cohesive nondimensional parameters. The first group relate spatial and temporal scales of the domain to \tilde{L} and $\tilde{\tau}$ respectively. The second group measure the magnitude of applied loads, $\tilde{\sigma}$, relative to $\tilde{\sigma}$. The changes to these nondimensional parameters cannot be modeled through self-similar

solution scheme.

We show that the relative size of cohesive process zone to dominant singular radius from LEFM theory, Λ/r , is proportional to $(\bar{\sigma}/\tilde{\sigma})^2$. We introduce a comparison LEFM solution for cohesive models and show that as Λ/r increases the solutions from these two model start to deviate and small-scale yielding assumption [9] loses its validity. Finally, the dynamic of a moving crack in an infinite domain is numerically studies and compared to LEFM comparison solution for various ratios of $\bar{\sigma}/\tilde{\sigma}$.

We use the Spacetime Discontinuous Galerkin Finite Element method developed in [12, 13] for our numerical simulations. Several features of these method, such as element-level balance of momentum, dual adaptive control of dissipation and fracture energy error, and linear complexity of the numerical scheme enables us to obtain very accurate solutions. As we will show, the cohesive process zone size approaches zero as the crack velocity approaches Rayleigh wave speed. In our numerical scheme we directly control the error in rendering TSR and will retain numerical accuracy even under such demanding conditions. For example, the occurrence of nonphysical numerical crack speeds is documented in [14] specially for high ratios of applied load to cohesive strength. Our numerical results, however, do not exhibit such problems and crack velocity remains bounded by the Rayleigh wave speed even for very large values of applied load to $\tilde{\sigma}$.

2.2 Formulation

In this section, we formulate the initial and boundary value problem for linearized elastodynamics, and then extend it to problems that include cohesive fracture interfaces modeled with *Traction-Separation Relations*(TSRs). Our formulation systematically combines space and time quantities, and, following the development in [12, 13], it uses the notation of differential forms on spacetime manifolds. This approach provides a direct, coordinate-free notation that can be used to express fluxes across spacetime interfaces with arbitrary orientation. This leads to concise representations of the governing equations that emphasize the notion of conservation on spacetime control volumes.

Although differential forms are not widely used in solid mechanics, their

use is well justified in the spacetime setting. In contrast to traditional tensor notation, for example, we can use differential forms to express the *Rankine-Hugoniot* jump conditions without referring to unit normal vectors on spacetime manifolds. This is a significant advantage, since no objective metric is available in classical mechanics to define magnitude and the orthogonality property for spacetime vectors. Similarly, the spacetime Stokes Theorem has a simple and elegant structure when written for differential forms, but its expression for spacetime tensor fields is problematic due to the absence of an objective definition for spacetime normal vectors.

Perhaps the most important advantage of the differential forms notation is that certain intrinsic relations between the spacetime mechanics fields, while obscured by tensorial notation, become clearly evident under differential forms notation. For example, in the dimensional analysis below, the forms representation of the problem reveals only two distinct dimensional groups for the mechanical loading and response fields, while the tensorial representation generates no less than six distinct groups.

2.2.1 Spacetime analysis domain and differential forms notation

Let \mathcal{D} be the reference spacetime domain, an open $(d+1)$ -manifold in $\mathbb{E}^d \times \mathbb{R}$, where d is the spatial dimension. The coordinates $(x^1, \dots, x^d, t) = (\mathbf{x}, t)$ in \mathcal{D} are defined with respect to the ordered basis $(\mathbf{e}_1, \dots, \mathbf{e}_d, \mathbf{e}_t)$ and are understood to be material coordinates associated with the undeformed configuration of a body followed by the time coordinate. The dual basis is denoted $(\mathbf{e}^1, \dots, \mathbf{e}^d, \mathbf{e}^t)$. From here on, we adopt the standard summation convention with Latin indices ranging from 1 to d . We employ differential forms with scalar, vector, covector, tensor and cotensor coefficients and follow the convention that symbols displayed in italic bold fonts denote differential forms, while symbols in upright bold fonts denote vector, covector, tensor or cotensor fields. Thus, $\boldsymbol{\sigma}$ and $\boldsymbol{\sigma}$ denote, respectively, the differential form for stress and the stress tensor field, as explained below.

The standard basis for spacetime 1-forms is $\{dx^1, \dots, dx^d, dt\}$. The *space-time volume element* is the $(d+1)$ -form given by $\boldsymbol{\Omega} := dx^1 \wedge \dots \wedge dx^d \wedge dt$, where “ \wedge ” is the *exterior product operator* on forms; cf. [15, 16, 17]. We have the standard basis for d -forms, $\{\star dx^j, \star dt\}$, in which \star is the Hodge star op-

erator and the indices of $\star dx^j$ shall, from here on, be treated as subindices for purposes of the summation convention. These satisfy $dx^i \wedge \star dx^j = \delta^i_j \boldsymbol{\Omega}$, $dt \wedge \star dx^j = \mathbf{0}$, $dt \wedge \star dt = \boldsymbol{\Omega}$ and $dx^i \wedge \star dt = \mathbf{0}$. For example, in the case $d = 2$, we have $\boldsymbol{\Omega} = dx^1 \wedge dx^2 \wedge dt$, $\star dx^1 = dx^2 \wedge dt$, $\star dx^2 = -dx^1 \wedge dt$ and $\star dt = dx^1 \wedge dx^2$.

The *temporal insertion* is defined in terms of the standard insertion (contraction) operator as, $\mathbf{i} := \mathbf{i}_{\bar{\mathbf{e}}_t}$, in which $\bar{\mathbf{e}}_t$ is a vector field on \mathcal{D} with uniform value \mathbf{e}_t . For $d = 2$, for example, we have $\mathbf{i}\star dx^1 = -dx^2$, $\mathbf{i}\star dx^2 = dx^1$ and $\mathbf{i}\star dt = \mathbf{0}$.

Let $\boldsymbol{\alpha}$ and $\boldsymbol{\beta}$ be r - and s -forms on \mathcal{D} , respectively, let \mathbf{a} and \mathbf{b} be m - and n -tensor fields on \mathcal{D} with $m \geq n$, and let w be a scalar field on \mathcal{D} . We write $\mathbf{a}\boldsymbol{\alpha}$ and $\mathbf{b}\boldsymbol{\beta}$ to denote an r -form and an s -form with tensor coefficients of order m and n , respectively. The exterior product of $\mathbf{a}\boldsymbol{\alpha}$ and $\mathbf{b}\boldsymbol{\beta}$ is the $(r + s)$ -form with tensor coefficients of order $m - n$ given by

$$\mathbf{a}\boldsymbol{\alpha} \wedge \mathbf{b}\boldsymbol{\beta} := \mathbf{a}(\mathbf{b})(\boldsymbol{\alpha} \wedge \boldsymbol{\beta}), \quad (2.1)$$

in which $\mathbf{a}(\mathbf{b})$ is the standard tensor mapping of \mathbf{b} by \mathbf{a} into a $(m - n)$ -tensor field. We introduce a special 1-form with vector coefficients, $\mathbf{d}\mathbf{x} := \mathbf{e}_i dx^i$, and a corresponding d -form with covector coefficients, $\star \mathbf{d}\mathbf{x} := \mathbf{e}^i \star dx^i$. The case where $s - t = 1$ is of particular interest in this paper. In this case,

Let $\boldsymbol{\alpha}$ be a r -form defined on a t -manifold \mathcal{Q} , and let Γ be a s -manifold, such that $r \leq s \leq t$ and $\Gamma \subset \overline{\mathcal{Q}}$. We use $\boldsymbol{\alpha}|_\Gamma$ to denote the *restriction of $\boldsymbol{\alpha}$ to Γ* , a r -form on Γ . The interpretation of the restriction operation is straightforward when $s = t$; it only involves restriction to the submanifold Γ with no alteration of the form. It has more subtle implications when $s < t$. First, we must sometimes interpret the restriction to Γ in the sense of the trace operator. This is the case, for example, when $\mathcal{Q} \subset \mathcal{D}$ is open and $\Gamma \subset \partial\mathcal{Q}$. Second, we must account for the fact that the cotangent spaces, $T_P^* \Gamma$ and $T_P^* \mathcal{Q}$, are distinct at any $P \in \Gamma$. The cases where $t - s = 1$ and $r = 1, s$ are of particular interest in this work. In these cases, the dimension of $T_P^* \Gamma$ is one less than the dimension of $T_P^* \mathcal{Q}$, and we must use a suitably reduced basis for covectors (s -covectors) to express the restriction as a 1-form (s -form) on Γ . See 2.2.3 for a more detailed discussion of restrictions of spacetime forms on \mathcal{D} to vertical d -manifolds.

We work with forms whose coefficients might suffer jumps, so we must

interpret the exterior derivative operator weakly, in the sense of distribution theory [17]. Thus, the *exterior derivative of a form*, indicated by the exterior derivative operator \mathbf{d} , generally contains a diffuse part and a jump part. Following the convention used in Miller *et al.* [18], we use $\mathbf{d}\alpha$ to denote the diffuse part of the exterior derivative of any form α and write the jump part separately and explicitly. As shown below, the Rankine-Hugoniot jump conditions for elastodynamics arise naturally as the jump parts of exterior derivatives that appear in the spacetime governing equations for kinematic compatibility and momentum balance.

Spacetime d -manifolds play an important role in our formulation, and certain special configurations of d -manifolds are of particular interest. A d -manifold with a uniform time coordinate is *horizontal*, and a d -manifold on which the time coordinate is independent of the spatial coordinate is *vertical*. The intermediate case, *i.e.*, d -manifolds where the spatial coordinates locally parameterize the temporal coordinate, are *inclined*.

The jump part of the exterior derivative of α across any d -manifold embedded in \mathcal{D} is a function of the restriction of α from opposing sides of the manifold. For any open $\mathcal{Q} \subset \mathcal{D}$, we use undecorated symbols and symbols decorated with a superscript “+” to denote, respectively, the interior and exterior restrictions of a differential form to $\partial\mathcal{Q}$. Then, for any $\mathcal{Q} \subset \mathcal{D}$, we define the *jump in \mathbf{f} across $\partial\mathcal{Q}$* as,

$$\llbracket \mathbf{f} \rrbracket_{\partial\mathcal{Q}} := \mathbf{f}^+|_{\partial\mathcal{Q}} - \mathbf{f}|_{\partial\mathcal{Q}}. \quad (2.2)$$

2.2.2 Mechanics fields

Let the ordered set $\mathcal{P}(\mathcal{D}) = \{\mathcal{Q}_\alpha\}_{\alpha=1}^N$ be a partition of the spacetime domain \mathcal{D} into N open subdomains with regular boundaries such that $\overline{\mathcal{D}} = \overline{\bigcup_\alpha \mathcal{Q}_\alpha}$. Let $L^2(\mathcal{D})$ and $H^1(\mathcal{Q})$ be the Hilbertian Sobolev spaces of order 0 on \mathcal{D} and order 1 on \mathcal{Q} , respectively. We define a broken Sobolev space on \mathcal{P} , $\mathcal{V} := \{\mathbf{w} \in L^2(\mathcal{D}) : \mathbf{w}|_{\mathcal{Q}_\alpha} \in H^1(\mathcal{Q}_\alpha), \alpha = 1, \dots, N\}$, in which \mathbf{w} is a covector field on \mathcal{D} (*i.e.*, a 0-form with covector coefficients), and note that \mathcal{V} admits vector fields with jumps between adjacent subdomains.

Kinematic quantities

Let \mathbf{u} denote the *displacement covector field* on \mathcal{D} , $\mathbf{u} = u_i \mathbf{e}^i$. The *velocity* \mathbf{v} and the *linearized strain* \mathbf{E} are 1-forms on \mathcal{D} with covector coefficients given by $\mathbf{v} := \mathbf{v} dt = v_i \mathbf{e}^i dt$ and $\mathbf{E} := \mathbf{E} \wedge d\mathbf{x} = \mathbf{E}(\mathbf{e}_k) dx^k$, in which $\mathbf{v} = v_i \mathbf{e}^i$ is the *velocity covector field* and the *linearized strain cotensor field*, $\mathbf{E} = E_{ij} \mathbf{e}^i \otimes \mathbf{e}^j$: $E_{ij} = E_{ji}$, is defined such that the value of $\mathbf{E}(\mathbf{e}_k)$ is a covector field. The *velocity-strain* is the 1-form with covector coefficients defined by,

$$\boldsymbol{\varepsilon} := \mathbf{v} + \mathbf{E}. \quad (2.3)$$

Force-like quantities

The force-like quantities include two d -forms with vector coefficients: the *linear momentum density*, $\mathbf{p} = \mathbf{p} \star dt$, and the *stress*, $\boldsymbol{\sigma} = \boldsymbol{\sigma} \wedge \star d\mathbf{x} = \boldsymbol{\sigma}(\mathbf{e}^k) \star dx^k$. The vector field \mathbf{p} and the tensor field $\boldsymbol{\sigma}$ (under the assumption of balance of angular momentum) have the Cartesian component expansions, $\mathbf{p} = p^i \mathbf{e}_i$ and $\boldsymbol{\sigma} = \sigma^{ij} \mathbf{e}_i \otimes \mathbf{e}_j$: $\sigma^{ij} = \sigma^{ji}$, on \mathcal{D} . We combine the linear momentum density and the stress in a single d -form,

$$\mathbf{M} := \mathbf{p} - \boldsymbol{\sigma}, \quad (2.4)$$

called the *spacetime momentum flux*. The momentum flux \mathbf{M} acts on any oriented, spacetime d -manifold embedded in \mathcal{D} to deliver the flux of linear momentum flux across the manifold. We also introduce the *body force* as a $(d+1)$ -form with vector coefficients given by $\mathbf{b} = \mathbf{b} \Omega$, in which $\mathbf{b} = b^i \mathbf{e}_i$ is the vector field on \mathcal{D} for body force per unit mass. The corresponding form for body force per unit volume is given by $\bar{\mathbf{b}} := \rho \mathbf{b}$, where ρ is the mass density per unit volume in the reference configuration.

2.2.3 Governing equations

Kinematic compatibility

The kinematic compatibility relations couple the independent displacement, velocity and strain fields. The *displacement-velocity relation* requires that

for all $\mathcal{Q} \subset \mathcal{D}$,

$$[(\mathbf{d}\mathbf{u} - \mathbf{v}) \wedge \star dt]_{\mathcal{Q} \setminus \Gamma_{\mathbf{u}}^J} = \mathbf{0}, \quad (2.5a)$$

$$[[\mathbf{u}]]_{\partial\mathcal{Q}} \star dt|_{\partial\mathcal{Q}} = \mathbf{0}, \quad (2.5b)$$

where $\Gamma_{\mathbf{u}}^J$ is the jump set of \mathbf{u}^1 . The diffuse part (2.5a) enforces the characteristic relation, $\dot{\mathbf{u}} - \mathbf{v} = \mathbf{0}$. In lieu of (2.5b), we enforce the stronger condition that, for all $\mathcal{Q} \subset \mathcal{D}$,

$$(\mathbf{u}_{\partial\mathcal{Q}}^* - \mathbf{u}|_{\partial\mathcal{Q}}) \star dt|_{\partial\mathcal{Q}} = \mathbf{0}, \quad (2.6)$$

where $\mathbf{u}_{\partial\mathcal{Q}}^*$ is the restriction to $\partial\mathcal{Q}$ of a target displacement field that is uniquely defined on every non-vertical d -manifold embedded in $\overline{\mathcal{D}}$. We note that (2.5b) is trivially satisfied on any vertical d -manifold (because $\star dt|_{\partial\mathcal{Q}} = \mathbf{0}$ on vertical manifolds), and observe that summing equation (2.6) for adjacent subdomains \mathcal{Q} on opposing sides of any non-vertical manifold on the interior of \mathcal{D} implies (2.5b). That is, in addition to enforcing the jump condition across any interior non-vertical manifold, we also require the jumps from both sides to vanish independently with respect to a common target field on the manifold. Consistent with the principle of causality, the target value $\mathbf{u}_{\partial\mathcal{Q}}^*$ on non-vertical manifolds is taken as the trace of \mathbf{u} from the earlier side of the manifold or is computed directly from initial data on $\partial\mathcal{D}$ [12, 18]. The value of $\mathbf{u}_{\partial\mathcal{Q}}^*$ is immaterial, and need not be specified, on vertical parts of $\partial\mathcal{Q}$.

The tensorial representation of the *velocity–strain relation* is,

$$\tilde{\nabla}\mathbf{v} - \dot{\mathbf{E}} = \mathbf{0}, \quad (2.7)$$

in which $\tilde{\nabla}$ is the symmetric part of the spatial gradient operator. This equation holds wherever $\boldsymbol{\varepsilon}$ is continuous. However, we need an associated jump condition on $\boldsymbol{\varepsilon}$ to complete the exterior derivative. It is convenient to express the complete velocity–strain compatibility relation, including the jump part, in terms of the weak exterior derivative of $\boldsymbol{\varepsilon}$. For all open regions

¹The *jump set of a form* is the set of all points where the form’s coefficient field is discontinuous. This definition also applies to tensor fields when viewed as 0-forms.

$\mathcal{Q} \subset \mathcal{D}$ and for all symmetric, second-order tensor fields \mathbf{T} on \mathcal{D} , we have

$$(\mathbf{d}\boldsymbol{\varepsilon} \wedge \mathbf{T})|_{\mathcal{Q} \setminus \Gamma_{\boldsymbol{\varepsilon}}^J} = \mathbf{0} \quad (2.8a)$$

$$[[\boldsymbol{\varepsilon}]]_{\partial\mathcal{Q}} \wedge \mathbf{T}|_{\partial\mathcal{Q}} = \mathbf{0}, \quad (2.8b)$$

in which $\Gamma_{\boldsymbol{\varepsilon}}^J$ is the jump set of $\boldsymbol{\varepsilon}$, and $\mathbf{T} := \mathbf{T} \wedge \mathbf{i} \star \mathbf{d}\mathbf{x}$. It is easily shown that (2.8a) is equivalent to (2.7).

Let the *target velocity-strain*, $\boldsymbol{\varepsilon}_{\partial\mathcal{Q}}^*$, be a single-valued 1-form on $\partial\mathcal{Q}$, similar to $\mathbf{u}_{\partial\mathcal{Q}}^*$, but computed from prescribed initial/boundary data for $\boldsymbol{\varepsilon}$ or from the solution to a local Riemann problem, as explained later. Then, parallel to our treatment of (2.5b), we replace (2.8b) with the stronger condition, for all $\mathcal{Q} \subset \mathcal{D}$,

$$(\boldsymbol{\varepsilon}_{\partial\mathcal{Q}}^* - \boldsymbol{\varepsilon}|_{\partial\mathcal{Q}}) \wedge \mathbf{T}|_{\partial\mathcal{Q}} = \mathbf{0}. \quad (2.9)$$

In addition to enforcing initial/boundary conditions and (2.8b) across interior d -manifolds, (2.9) requires the solution to preserve the characteristic structure of the governing system across all interior interfaces between adjacent spacetime subdomains. In other words, any jumps that arise in the solution for $\boldsymbol{\varepsilon}$ must be consistent with the principle of causality.

The tensorial *strain-displacement relation* is, $(\mathbf{E} - \tilde{\nabla}\mathbf{u})|_{\mathcal{Q} \setminus \Gamma_{\mathbf{u}}^J} = \mathbf{0}$. If the initial data satisfy this condition, then (2.5) and (2.8) are sufficient to enforce the strain-displacement relation everywhere. From here on, we assume that the initial data satisfy this condition, and do not include explicitly the strain-displacement relation in our governing system of equations.

Constitutive relation

We introduce a linear transformation, denoted by \mathcal{C} , that maps 1-forms with tensor coefficients into d -forms with tensor coefficients such that

$$\mathbf{M} = \mathcal{C}(\boldsymbol{\varepsilon}(\mathbf{E}, \mathbf{v})) := \mathbf{R}(\mathbf{v}) \star dt - \mathbf{C}(\mathbf{E}) \wedge \star \mathbf{d}\mathbf{x} \text{ on } \mathcal{D} \quad (2.10)$$

in which $\mathbf{R} = \rho \delta^{ij} \mathbf{e}_i \otimes \mathbf{e}_j$: $\rho > 0$ is the scalar mass density field, and the positive fourth-order elasticity tensor field, $\mathbf{C} = C^{ijkl} \mathbf{e}_i \otimes \mathbf{e}_j \otimes \mathbf{e}_k \otimes \mathbf{e}_l$, exhibits the standard major and minor symmetries. Equations (2.3), (2.4) and (2.10) imply the familiar tensorial component relations, $p^i = \rho \delta^{ij} v_j$ and $\sigma^{ij} = C^{ijkl} E_{kl}$.

Balance of momentum

Balance of linear momentum requires that for all $\mathcal{Q} \subset \mathcal{D}$,

$$\int_{\partial\mathcal{Q}} \mathbf{M} - \int_{\mathcal{Q}} \bar{\mathbf{b}} = \mathbf{0}. \quad (2.11)$$

Equation (2.11) also implies balance of angular momentum under our a priori assumption that the stress tensor field $\boldsymbol{\sigma}$ is symmetric [12]. Let $\Gamma_{\mathbf{M}}^{\mathbf{J}}$ be the jump set of \mathbf{M} on \mathcal{D} . Then for all $\mathcal{Q} \subset \mathcal{D}$,

$$(\mathbf{dM} - \bar{\mathbf{b}})|_{\mathcal{Q} \setminus \Gamma_{\mathbf{M}}^{\mathbf{J}}} = \mathbf{0} \quad (2.12a)$$

$$\llbracket \mathbf{M} \rrbracket|_{\partial\mathcal{Q}} = \mathbf{0} \quad (2.12b)$$

enforces (2.11) via the Stokes theorem while accounting for possible jumps in \mathbf{M} . The tensorial form of (2.12a) is $[\nabla \cdot \boldsymbol{\sigma} + \bar{\mathbf{b}} - \dot{\mathbf{p}}] \boldsymbol{\Omega} = \mathbf{0}$ on $\mathcal{Q} \setminus \Gamma_{\mathbf{M}}^{\mathbf{J}}$. Thus, (2.12a) is the forms representation of the equation of motion. It can also be shown that (2.12b) is the forms representation of the Rankine-Hugoniot condition that governs shocks in \mathbf{p} and $\boldsymbol{\sigma}$. That is, the Rankine-Hugoniot condition is simply the jump part of the equation of motion.

Once again, we replace the basic jump condition (2.12b) with a stronger condition,

$$\mathbf{M}_{\partial\mathcal{Q}}^* - \mathbf{M}|_{\partial\mathcal{Q}} = \mathbf{0} \quad \forall \mathcal{Q} \subset \mathcal{D}, \quad (2.13)$$

in which the *target momentum flux* \mathbf{M}^* is defined uniquely on every d -manifold embedded in $\bar{\mathcal{D}}$ through the initial/boundary conditions [12] or the solution to a local Riemann problem. In addition to enforcing the boundary and initial conditions, writing the jump condition from each side with respect to $\mathbf{M}_{\partial\mathcal{Q}}^*$ requires that the solution for \mathbf{M} preserves the characteristic structure of the elastodynamic system across all interior d -manifolds embedded in \mathcal{D} . In other words, the solution must satisfy simultaneously the Rankine-Hugoniot condition and the principle of causality.

2.2.4 Initial and boundary data

Given suitable prescribed data for $\bar{\mathbf{b}}$ and the initial/boundary data, and subject to the symmetry constraint on the stress tensor, the governing equations, (2.5), (2.8), (2.10) and (2.12), fully define the elastodynamic initial boundary

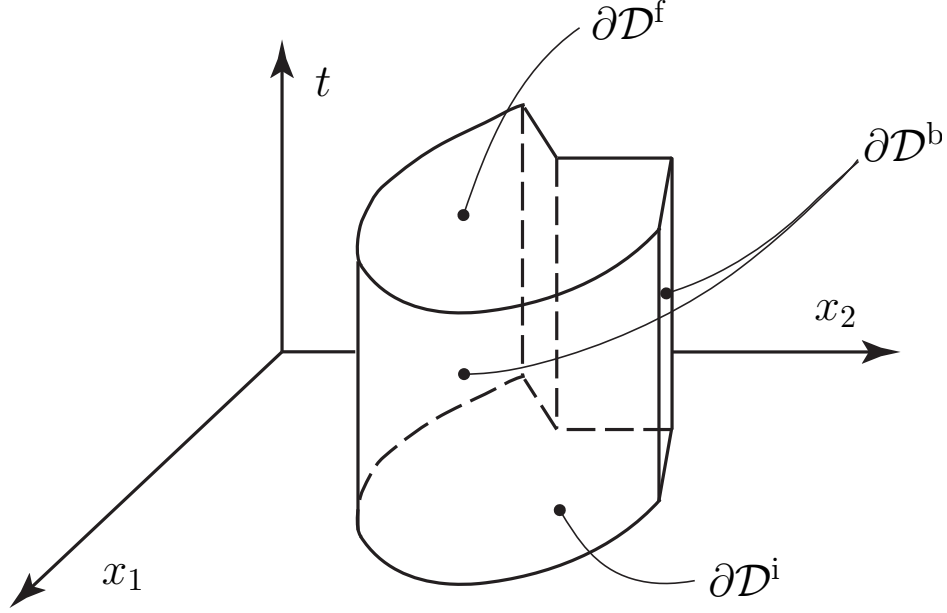


Figure 2.1: Cylindrical spacetime domain and boundary partition for $d = 2$.

value problem. In general, the spacetime domain boundary $\partial\mathcal{D}$ might include inclined segments that model moving boundaries. For simplicity, we focus here on a more typical problem, depicted in Figure 2.1, where $\partial\mathcal{D}$ is comprised of a horizontal d -manifold at the initial time, denoted by $\partial\mathcal{D}^i$, a horizontal d -manifold at the terminal (final) time, denoted by $\partial\mathcal{D}^f$, and a collection of vertical d -manifolds that connect $\partial\mathcal{D}^f$ and $\partial\mathcal{D}^i$. The latter collection, denoted by $\partial\mathcal{D}^b$, represents the spacetime extension of the boundary of a fixed reference spatial domain. In this subsection, we consider the specification of initial data on $\partial\mathcal{D}^i$, boundary data on $\partial\mathcal{D}^b$ and free, unconstrained conditions on $\partial\mathcal{D}^f$ for the simplified spacetime domain geometry. We stress, however, that the dimensional analysis to follow is valid for more general domain configurations, including those whose boundary includes inclined segments.

The restrictions of the velocity–strain and the momentum flux to the horizontal, initial boundary $\partial\mathcal{D}^i$ simplify according to, $\boldsymbol{\varepsilon}|_{\partial\mathcal{D}^i} = \mathbf{E}|_{\partial\mathcal{D}^i}$ and $\mathbf{M}|_{\partial\mathcal{D}^i} = \mathbf{p}|_{\partial\mathcal{D}^i}$. Thus, we express the initial conditions for displacement, strain and linear momentum density on $\partial\mathcal{D}^i$ through the jump conditions, (2.6), (2.9) and (2.13), by setting $\mathbf{u}_{\partial\mathcal{D}^i}^* = \bar{\mathbf{u}}$, $\boldsymbol{\varepsilon}_{\partial\mathcal{D}^i}^* = \bar{\mathbf{E}}$ and $\mathbf{M}_{\partial\mathcal{D}^i}^* = \bar{\mathbf{p}}$, in which an overbar denotes prescribed initial data. Recall that, by assumption, $\bar{\mathbf{u}}$ and $\bar{\mathbf{E}}$ are kinematically compatible.

The solution is unconstrained on the terminal boundary $\partial\mathcal{D}^f$, another horizontal d -manifold where the simplifications, $\boldsymbol{\varepsilon}|_{\partial\mathcal{D}^f} = \mathbf{E}|_{\partial\mathcal{D}^f}$ and $\mathbf{M}|_{\partial\mathcal{D}^f} = \mathbf{p}|_{\partial\mathcal{D}^f}$, hold. We model the free conditions by setting $\mathbf{u}_{\partial\mathcal{D}^f}^* = \mathbf{u}|_{\partial\mathcal{D}^f}$, $\boldsymbol{\varepsilon}_{\partial\mathcal{D}^f}^* = \mathbf{E}|_{\partial\mathcal{D}^f}$ and $\mathbf{M}_{\partial\mathcal{D}^f}^* = \mathbf{p}|_{\partial\mathcal{D}^f}$. Thus, (2.6), (2.9) and (2.13) are trivially satisfied on $\partial\mathcal{D}^f$.

The remainder of $\partial\mathcal{D}$ consists of the collection of vertical d -manifolds that comprise $\partial\mathcal{D}^b$. Since (2.6) is trivially satisfied on any vertical manifold, there is no need to specify $\mathbf{u}_{\partial\mathcal{D}^b}^*$. In preparation for enforcing the boundary conditions, we choose a disjoint partition of $\partial\mathcal{D}^b$ into a Dirichlet part $\partial\mathcal{D}^\varepsilon$ and a Neumann part $\partial\mathcal{D}^M$. On any vertical d -manifold Γ , we have $(\boldsymbol{\varepsilon} \wedge \mathbf{T})|_\Gamma = (\mathbf{v} \wedge \mathbf{T})|_\Gamma$ (for any \mathbf{T} defined as above) and $\mathbf{M}|_\Gamma = -\boldsymbol{\sigma}|_\Gamma$. Thus, we enforce the Dirichlet boundary conditions by setting $\boldsymbol{\varepsilon}_{\partial\mathcal{D}^\varepsilon}^* = \bar{\mathbf{v}}$ in (2.9) and $\mathbf{M}_{\partial\mathcal{D}^\varepsilon}^* = -\boldsymbol{\sigma}|_{\partial\mathcal{D}^\varepsilon}$ in (2.13), where $\bar{\mathbf{v}}$ is the prescribed boundary velocity. We similarly enforce the Neumann boundary conditions via (2.13) and (2.9) by setting $\mathbf{M}_{\partial\mathcal{D}^M}^* = -\bar{\boldsymbol{\sigma}}$ and $\boldsymbol{\varepsilon}_{\partial\mathcal{D}^M}^* = \mathbf{v}|_{\partial\mathcal{D}^M}$, in which $\bar{\boldsymbol{\sigma}}$ denotes the prescribed boundary traction.

2.2.5 Extension to incorporate cohesive models

Cohesive interfaces are often added to the elastodynamics problem to model crack nucleation and growth. In its most basic form, a cohesive interface is a material surface embedded in the interior of the analysis domain across which jumps in the kinematic fields are permitted and the momentum flux is described by a cohesive traction-separation relation. In the spacetime setting, as is the case for all material surfaces, cohesive interfaces are modeled as vertical d -manifolds. It is useful then, to consider the relation between the spacetime momentum flux \mathbf{M} and the tensorial representation of surface traction on vertical d -manifolds.

Let Γ be a vertical d -manifold embedded in $\mathbb{E}^d \times \mathbb{R}$, as illustrated in figure 2.2 for the case $d = 2$. To facilitate a description of the restricted cotangent space $T^*\Gamma$, we define on Γ a local frame, $\{\underline{\mathbf{e}}^i, \mathbf{e}^t\}_{i=1}^d : \underline{\mathbf{e}}^1 \perp T^*\Gamma|_{\mathbb{E}^d}$, with local coordinates $\{\underline{x}_i, t\}_{i=1}^d$, in which underlined symbols denote items referred to the local frame. In contrast to the $(d+1)$ -manifold, $\mathcal{D} \subset \mathbb{E}^d \times \mathbb{R}$, where the standard basis for d -forms in local coordinates is $\{\star d\underline{x}^k, \star dt\}_{k=1}^d$, the basis for d -forms on the d -manifold Γ is the singleton set, $\{\star d\underline{x}^1\}$. Thus, the expansion of the stress form $\boldsymbol{\sigma}$ with respect to the local frame involves a

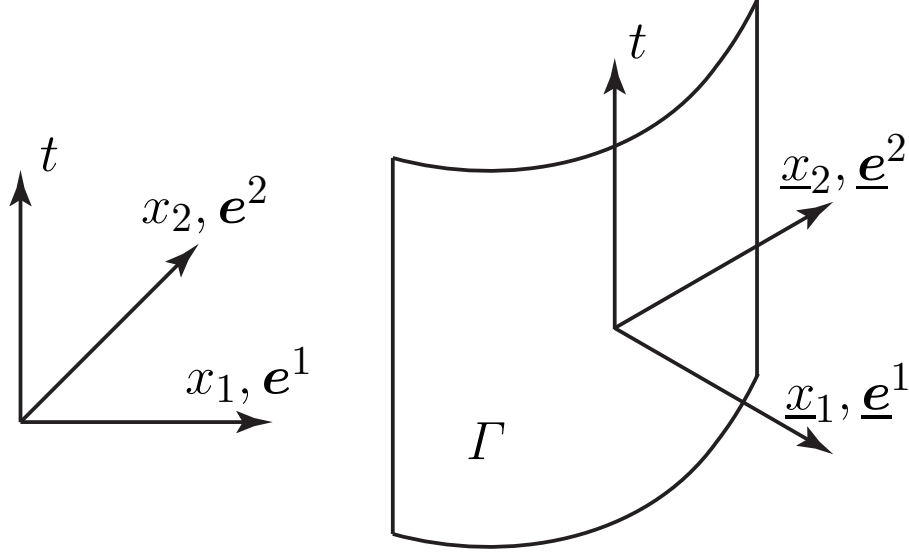


Figure 2.2: Local coordinate system on a vertical 2-manifold Γ embedded in $\mathbb{E}^2 \times \mathbb{R}$.

linear combination of d -forms:

$$\boldsymbol{\sigma} := \boldsymbol{\sigma} \wedge \star d\mathbf{x} = \boldsymbol{\sigma} \wedge \underline{e}^k \star d\underline{x}^k = \boldsymbol{\sigma}(\underline{e}^k) \star d\underline{x}^k \quad (2.14)$$

However, the restriction, $\boldsymbol{\sigma}|_\Gamma$, is a top form on Γ that involves only a single d -form:

$$\boldsymbol{\sigma}|_\Gamma = \boldsymbol{\sigma} \wedge \underline{e}^1 \star d\underline{x}^1 = \boldsymbol{\sigma}(\underline{e}^1) \star d\underline{x}^1 \quad (2.15)$$

since $\star d\underline{x}^k|_\Gamma = \star dt|_\Gamma = \mathbf{0}$ for $k \neq 1$. Recalling the Cauchy relation and that the unit covector \underline{e}^1 is everywhere normal to the cotangent space $(T^*\Gamma)|_{\mathbb{E}^d}$, it is clear that $\boldsymbol{\sigma}(\underline{e}^1)$ and $\star d\underline{x}^1$ are, respectively, the *surface traction field* and the singleton basis for top d -forms, both on the d -manifold Γ . In other words, $\boldsymbol{\sigma}|_\Gamma$ is the *surface traction d -form on Γ* . Note that the restriction operation on $\boldsymbol{\sigma}$ maps a d -form with vector coefficients on the $(d+1)$ -manifold \mathcal{D} into a top d -form with vector coefficients on the d -manifold Γ ; *i.e.*, it involves more than a simple trace operation.

Let $\tilde{\Gamma}$ denote the collection of all the cohesive interfaces in a given elastodynamic model, and consider all $\mathcal{Q} \subset \mathcal{D} \ni \partial\mathcal{Q} \cap \tilde{\Gamma} \neq \emptyset$. Since $\tilde{\Gamma}$ is entirely vertical, we have, $\mathbf{u} \star dt|_{\tilde{\Gamma}} = \mathbf{0}$ for arbitrary \mathbf{u} , $\boldsymbol{\varepsilon}|_{\tilde{\Gamma}} = \mathbf{v}|_{\tilde{\Gamma}}$ and $\mathbf{M}|_{\tilde{\Gamma}} = -\boldsymbol{\sigma}|_{\tilde{\Gamma}}$.

For each subdomain \mathcal{Q} , we choose

$$\boldsymbol{\varepsilon}_{\tilde{\Gamma} \cap \partial \mathcal{Q}}^* = \boldsymbol{v}|_{\tilde{\Gamma} \cap \partial \mathcal{Q}}. \quad (2.16)$$

Thus, the kinematic jump conditions, (2.6) and (2.9), are trivially satisfied, allowing independent motion of the material on each side of the cohesive interface. It only remains, then, to specify the function that uniquely determines $\boldsymbol{\sigma}_{\tilde{\Gamma}}^*$ on $\tilde{\Gamma}$ according to the TSR.

In general, we write,

$$\boldsymbol{\sigma}_{\tilde{\Gamma}}^* = \tilde{\mathbf{s}}(\mathbf{u}, \boldsymbol{v}, \boldsymbol{\sigma}), \quad (2.17)$$

in which $\tilde{\mathbf{s}} = \tilde{\mathbf{s}} \star d\underline{x}^1$ is a top form on the d -manifold $\tilde{\Gamma}$ whose coefficient $\tilde{\mathbf{s}}$ is the surface traction field generated by the cohesive TSR. Thus, (2.13) enforces the cohesive traction condition. From here on, but without affecting the generality of our dimensional analysis, we focus on the simplest and most common constitutive relation for $\tilde{\mathbf{s}}$, a traction–separation relation (TSR) written on $\tilde{\Gamma}$ as,

$$\tilde{\mathbf{s}}(\llbracket \mathbf{u} \rrbracket_{\tilde{\Gamma}}; \tilde{\sigma}, \tilde{\delta}, \mathbf{o}_{\tilde{\Gamma}}) = \tilde{\sigma} \mathbf{f}(\tilde{\delta}^{-1} \llbracket \mathbf{u} \rrbracket_{\tilde{\Gamma}}; \mathbf{o}_{\tilde{\Gamma}}), \quad (2.18)$$

in which \mathbf{f} is a normalized TSR function that relates normalized traction to normalized separation, the covector field $\llbracket \mathbf{u} \rrbracket_{\tilde{\Gamma}}$ is the *cohesive separation* and $\mathbf{o}_{\tilde{\Gamma}}$ is the local orientation on $\tilde{\Gamma}$. The parameters $\tilde{\sigma}$ and $\tilde{\delta}$ are reference scales for the cohesive traction and the cohesive separation. For example, $\tilde{\sigma}$ is sometimes taken to be the cohesive strength, with $\tilde{\delta}$ the cohesive separation that corresponds to $\tilde{\sigma}$ in the TSR.

We shall use (1) := *I*, (2) := *II* and (3) := *III* to map the local, coordinate directions $\underline{x}_k; k = 1, \dots, d$ on $\tilde{\Gamma}$ into the normal (*I*) and tangential (*II*, *III*) modes of cohesive separation. The cohesive modal works of separation are given by,

$$\tilde{\phi}_{(k)} = \int_0^\infty \tilde{\mathbf{s}}(\xi \underline{e}^k) \cdot \underline{e}^k d\xi \quad (\text{no sum on } k), \quad (2.19)$$

in which we have suppressed the secondary parameters in $\tilde{\mathbf{s}}$, *cf.* (2.18).

Equation (2.18) does not imply equal cohesive strengths, equal critical separations or equal works of separation across the separation modes. The cohesive parameters, $\tilde{\sigma}$ and $\tilde{\delta}$, only provide dimensional scaling for the TSR. However, (2.18) does imply fixed ratios between the modal cohesive strengths and between the modal critical separations in the dimensional analysis pre-

sented in section 2.3.

Cohesive models can also be parameterized by the work of separation and either of $\tilde{\sigma}$ or $\tilde{\delta}$. Thus, alternative forms of (2.18) are given by

$$\tilde{\mathbf{s}}(\llbracket \mathbf{u} \rrbracket_{\tilde{\Gamma}}; \mathbf{o}_\Gamma) = \tilde{\sigma} \mathbf{g}(\tilde{\sigma} \tilde{\phi}^{-1} \llbracket \mathbf{u} \rrbracket_{\tilde{\Gamma}}; \mathbf{o}_\Gamma) = \frac{\tilde{\phi}}{\tilde{\delta}} \mathbf{h}(\tilde{\delta}^{-1} \llbracket \mathbf{u} \rrbracket_{\tilde{\Gamma}}; \mathbf{o}_\Gamma), \quad (2.20)$$

where $\tilde{\phi}$ is a reference scale for work of separation, and the values of \mathbf{g} and \mathbf{h} are vector fields on $\tilde{\Gamma}$.

2.3 Dimensional analysis

2.3.1 Elastodynamic processes

We define an *elastodynamic process* as an ordered set $\{\mathbf{u}, \boldsymbol{\varepsilon}, \mathbf{M}, \mathcal{C}, \bar{\mathbf{b}}, \bar{\mathbf{u}}, \bar{\boldsymbol{\varepsilon}}, \bar{\mathbf{M}}; (\mathbf{x}, t)\}$ that satisfies the governing equations of momentum balance and kinematic compatibility subject to the the corresponding jump conditions, including the initial and boundary conditions, and the constitutive relations. We similarly define an *elastodynamic cohesive process* as an ordered set $\{\mathbf{u}, \boldsymbol{\varepsilon}, \mathbf{M}, \mathcal{C}, \tilde{\mathbf{s}}, \bar{\mathbf{b}}, \bar{\mathbf{u}}, \bar{\boldsymbol{\varepsilon}}, \bar{\mathbf{M}}; (\mathbf{x}, t)\}$ that additionally satisfies the cohesive TSR (2.18).

We categorize the members of elastodynamic processes as follows.

1. *Kinematic fields:* The kinematic solution fields are the displacements \mathbf{u} and the velocity–strain $\boldsymbol{\varepsilon} = \mathbf{v} + \mathbf{E}$. The prescribed initial/boundary data in $\bar{\mathbf{u}}$ and $\bar{\boldsymbol{\varepsilon}} = \bar{\mathbf{v}} + \bar{\mathbf{E}}$ comprise the kinematic loading.
2. *Force-like fields:* The spacetime momentum flux $\mathbf{M} = \mathbf{p} - \boldsymbol{\sigma}$, is the force-like solution field. The force-like loading includes the body force per unit volume, $\bar{\mathbf{b}} := \rho \mathbf{b}$, and the initial/boundary data in $\bar{\mathbf{M}} = \bar{\mathbf{p}} - \bar{\boldsymbol{\sigma}}$.
3. *Constitutive parameters:* These include the linear transformation \mathcal{C} , defined by the elasticity tensor \mathbf{C} and mass density ρ . When a cohesive fracture model is included, we also have the cohesive traction $\tilde{\mathbf{s}}$, whose coefficient $\tilde{\mathbf{s}}$ can be expressed in terms of the normalized TSR function \mathbf{f} and the cohesive scales, $\tilde{\sigma}$ and $\tilde{\delta}$; *cf.* (2.18).
4. *Spacetime coordinates:* The spacetime coordinates (\mathbf{x}, t) parameterize the spacetime analysis domain \mathcal{D} .

We consider below independent scalings of the members of an elastodynamic process and investigate the conditions under which the scaled system is itself an elastodynamic process. We also describe a similar dimensional analysis of elastodynamic cohesive fracture processes. These analyses identify key nondimensional groups that govern the response of elastodynamic systems in general and dynamic cohesive fracture models in particular, and we investigate the influence of each nondimensional group on the system response.

We carry out our dimensional analyses using differential forms notation, but consider scalings of both the forms overall and of just the form coefficients, as would be done in analyses using conventional tensor notation. We show that to obtain a scaled elastodynamic process, the velocity scalings implied by the spatial and temporal coordinate scalings and by the scalings of the material properties must be identical. We also find that only four distinct scalings are required to define an elastodynamic process when we work directly with forms, while eight are required when tensor notation is used. This simplification provides new evidence of the elegance and insight afforded by spacetime mechanics formulations that use differential forms and the exterior calculus.

2.3.2 Scaled elastodynamic processes

Let $\{\mathbf{u}, \boldsymbol{\varepsilon}, \mathbf{M}, \mathcal{C}, \bar{\mathbf{b}}, \bar{\mathbf{u}}, \bar{\boldsymbol{\varepsilon}}, \bar{\mathbf{M}}; (\mathbf{x}, t)\}$ be an elastodynamic process, and let $\{\mathbf{u}', \boldsymbol{\varepsilon}', \mathbf{M}', \mathcal{C}', \bar{\mathbf{b}}', \bar{\mathbf{u}}', \bar{\boldsymbol{\varepsilon}}', \bar{\mathbf{M}}'; (\mathbf{x}', t')\}$ be a scaled system defined according to the relations,

$$\alpha = \lambda_\alpha \alpha', \quad (2.21)$$

in which α and α' are members (or member components) of the original process and the scaled system, and λ_α is a scaling factor specific to α . For generality, we provide independent scalings for the components of $\boldsymbol{\varepsilon}$, \mathbf{M} and \mathcal{C} . For each member of the process, we will use the font of the subscript α to distinguish the scaling factor for the overall form from the scaling factor for its vector or tensor coefficient. For example, $\lambda_{\bar{\mathbf{b}}}$ and $\lambda_{\bar{\mathbf{b}}}$ denote, respectively, the scaling factors for the $(d + 1)$ -form $\bar{\mathbf{b}}$ and the vector field $\bar{\mathbf{b}}$. Next, we develop the necessary conditions on the set $\{\lambda_\alpha\}$ to ensure that the scaled system is also an elastodynamic process.

According to (2.21) the scalings of the spacetime coordinates are²

$$\mathbf{x} = \lambda_{\mathbf{x}} \mathbf{x}' \quad t = \lambda_t t' \quad (2.22)$$

and the resulting scalings between the bases for 1-forms, d -forms and $(d+1)$ -forms in the two systems are,

$$dx^i = \lambda_{\mathbf{x}} dx'^i \quad \mathbf{dx} = \lambda_{\mathbf{x}} \mathbf{dx}' \quad dt = \lambda_t dt', \quad (2.23a)$$

$$\star dx^i = \lambda_{\mathbf{x}}^{d-1} \lambda_t \star dx'^i \quad \star \mathbf{dx} = \lambda_{\mathbf{x}}^{d-1} \lambda_t \star \mathbf{dx}' \quad \star dt = \lambda_{\mathbf{x}}^d \star dt', \quad (2.23b)$$

$$\Omega = \lambda_{\mathbf{x}}^d \lambda_t \Omega'. \quad (2.23c)$$

Since $\frac{\partial u^i}{\partial x^j} = \frac{\partial(\lambda_{\mathbf{u}} u'^i)}{\partial(\lambda_{\mathbf{x}} x'^j)} = \frac{\lambda_{\mathbf{u}}}{\lambda_{\mathbf{x}}} \frac{\partial u'^i}{\partial x'^j}$, $\frac{\partial u^i}{\partial t} = \frac{\partial(\lambda_{\mathbf{u}} u'^i)}{\partial(\lambda_t t')} = \frac{\lambda_{\mathbf{u}}}{\lambda_t} \frac{\partial u'^i}{\partial t'}$, and according to (2.21) and (2.23), if the scaled system satisfies the kinematic compatibility relations, then the kinematic forms and their tensor coefficients must transform as,

$$\mathbf{u} = \lambda_{\mathbf{u}} \mathbf{u}' \quad \mathbf{u} = \lambda_{\mathbf{u}} \mathbf{u}', \quad (2.24a)$$

$$\mathbf{v} = \lambda_{\mathbf{u}} \mathbf{v}' \quad \mathbf{v} = \frac{\lambda_{\mathbf{u}}}{\lambda_t} \mathbf{v}', \quad (2.24b)$$

$$\mathbf{E} = \lambda_{\mathbf{u}} \mathbf{E}' \quad \mathbf{E} = \frac{\lambda_{\mathbf{u}}}{\lambda_{\mathbf{x}}} \mathbf{E}', \quad (2.24c)$$

$$\Rightarrow \boldsymbol{\varepsilon} = \lambda_{\mathbf{u}} \boldsymbol{\varepsilon}', \quad (2.24d)$$

so that $\lambda_{\mathbf{u}} = \lambda_{\mathbf{v}} = \lambda_{\mathbf{E}} = \lambda_{\boldsymbol{\varepsilon}}$, while $\lambda_{\mathbf{v}} = \lambda_{\mathbf{u}}/\lambda_t$ and $\lambda_{\mathbf{E}} = \lambda_{\mathbf{u}}/\lambda_{\mathbf{x}}$. Thus, all of the kinematic forms share a common scaling, $\lambda_{\mathbf{u}}$, while the three scalings for their vector and tensor coefficients are distinct. To ensure that the kinematic jump conditions are satisfied everywhere in the scaled system, it is necessary and sufficient that the prescribed kinematic initial/boundary data satisfy

$$\bar{\mathbf{u}} = \lambda_{\mathbf{u}} \bar{\mathbf{u}}' \quad \bar{\mathbf{u}} = \lambda_{\mathbf{u}} \bar{\mathbf{u}}', \quad (2.25a)$$

$$\bar{\mathbf{v}} = \lambda_{\mathbf{u}} \bar{\mathbf{v}}' \quad \bar{\mathbf{v}} = \frac{\lambda_{\mathbf{u}}}{\lambda_t} \bar{\mathbf{v}}', \quad (2.25b)$$

$$\bar{\mathbf{E}} = \lambda_{\mathbf{u}} \bar{\mathbf{E}}' \quad \bar{\mathbf{E}} = \frac{\lambda_{\mathbf{u}}}{\lambda_{\mathbf{x}}} \bar{\mathbf{E}}', \quad (2.25c)$$

$$\Rightarrow \bar{\boldsymbol{\varepsilon}} = \lambda_{\mathbf{u}} \bar{\boldsymbol{\varepsilon}}'. \quad (2.25d)$$

²For simplicity, we restrict our attention to equal scalings in all spatial directions. Our results can easily be extended to accommodate distinct scales for each direction. However, the scalings of the cohesive parameters introduced in 2.3.3 would then depend on the local orientation of the spacetime manifolds that model cohesive interfaces.

Next we consider conditions which guarantee that the scaled system satisfies the constitutive relations. Combining (2.10) with results from (2.23) and (2.24), we obtain scaling relations that govern the body force and the momentum-flux components,

$$\bar{\mathbf{b}} = \lambda_{\bar{\mathbf{b}}} \lambda_{\mathbf{x}}^d \lambda_t \bar{\mathbf{b}}' \qquad \bar{\mathbf{b}} = \lambda_{\rho} \lambda_{\mathbf{u}} \bar{\mathbf{b}}', \quad (2.26a)$$

$$\mathbf{p} = \frac{\lambda_{\rho} \lambda_{\mathbf{u}} \lambda_{\mathbf{x}}^d}{\lambda_t} \mathbf{p}' \qquad \mathbf{p} = \frac{\lambda_{\rho} \lambda_{\mathbf{u}}}{\lambda_t} \mathbf{p}', \quad (2.26b)$$

$$\boldsymbol{\sigma} = \lambda_{\mathbf{C}} \lambda_{\mathbf{u}} \lambda_{\mathbf{x}}^{d-2} \lambda_t \boldsymbol{\sigma}' \qquad \boldsymbol{\sigma} = \frac{\lambda_{\mathbf{C}} \lambda_{\mathbf{u}}}{\lambda_{\mathbf{x}}} \boldsymbol{\sigma}'. \quad (2.26c)$$

so that $\lambda_{\bar{\mathbf{b}}} = \lambda_{\rho} \lambda_{\mathbf{u}}$, $\lambda_{\mathbf{p}} = \lambda_{\rho} \lambda_{\mathbf{u}} / \lambda_t$ and $\lambda_{\boldsymbol{\sigma}} = \lambda_{\mathbf{C}} \lambda_{\mathbf{u}} / \lambda_{\mathbf{x}}$.

Finally, we identify conditions which ensure that the scaled system satisfies the equation of motion. We use (2.23), (2.26) and the Chain Rule to rewrite the equation of motion for the unscaled system in terms of scaled quantities:

$$[\nabla \cdot \boldsymbol{\sigma} + \bar{\mathbf{b}} - \dot{\mathbf{p}}] \boldsymbol{\Omega} = \left[\frac{\lambda_{\boldsymbol{\sigma}}}{\lambda_{\mathbf{x}}} \nabla \cdot \boldsymbol{\sigma}' + \lambda_{\bar{\mathbf{b}}} \bar{\mathbf{b}}' - \frac{\lambda_{\rho} \lambda_{\mathbf{u}}}{\lambda_t^2} \dot{\mathbf{p}}' \right] \lambda_{\mathbf{x}}^d \lambda_t \boldsymbol{\Omega}' = \mathbf{0}. \quad (2.27)$$

In order for the scaled system to be an elastodynamic process, we must have $[\nabla \cdot \boldsymbol{\sigma}' + \bar{\mathbf{b}}' - \dot{\mathbf{p}}'] \boldsymbol{\Omega}' = \mathbf{0}$. Combining this result with (2.26) and (2.27) delivers,

$$\frac{\lambda_{\mathbf{C}} \lambda_{\mathbf{u}}}{\lambda_{\mathbf{x}}^2} = \lambda_{\bar{\mathbf{b}}} = \frac{\lambda_{\rho} \lambda_{\mathbf{u}}}{\lambda_t^2} \quad (2.28a)$$

$$\Rightarrow \frac{\lambda_{\mathbf{x}}}{\lambda_t} = \sqrt{\frac{\lambda_{\mathbf{C}}}{\lambda_{\rho}}}. \quad (2.28b)$$

Combining these results with (2.26), we obtain

$$\bar{\mathbf{b}} = \lambda_{\bar{\mathbf{b}}} \bar{\mathbf{b}}' \qquad \mathbf{p} = \lambda_{\bar{\mathbf{b}}} \mathbf{p}' \qquad \boldsymbol{\sigma} = \lambda_{\bar{\mathbf{b}}} \boldsymbol{\sigma}' \qquad \Rightarrow \mathbf{M} = \lambda_{\bar{\mathbf{b}}} \mathbf{M}', \quad (2.29)$$

so that $\lambda_{\bar{\mathbf{b}}} = \lambda_{\mathbf{M}} = \lambda_{\mathbf{p}} = \lambda_{\boldsymbol{\sigma}} = \lambda_{\mathbf{C}} \lambda_{\mathbf{u}} \lambda_{\mathbf{x}}^{d-2} \lambda_t = \lambda_{\rho} \lambda_{\mathbf{u}} \lambda_{\mathbf{x}}^d / \lambda_t$. That is, all the force-like forms share a common scaling factor, $\lambda_{\bar{\mathbf{b}}}$, while the scaling factors for their vector and tensor coefficients are distinct. To ensure that the momentum flux jump conditions are satisfied everywhere in the scaled system, it is necessary and sufficient that the prescribed initial/boundary

data satisfy

$$\bar{\mathbf{M}} = \lambda_{\bar{\mathbf{b}}}\bar{\mathbf{M}}' \quad \bar{\mathbf{p}} = \lambda_{\mathbf{p}}\bar{\mathbf{p}}', \quad \bar{\boldsymbol{\sigma}}' = \lambda_{\boldsymbol{\sigma}}\bar{\boldsymbol{\sigma}}'. \quad (2.30)$$

Let $\|\mathbf{C}\|$ be a measure of the elasticity tensor; then the elastic wave speeds are proportional to $\sqrt{\|\mathbf{C}\|/\rho}$. As a result, $\lambda_{c_1} := \sqrt{\lambda_{\mathbf{C}}/\lambda_{\rho}}$ is the scaling factor for the elastic wave speeds due to the scaling of the material properties. Let us also define $\lambda_{c_2} := \lambda_{\mathbf{x}}/\lambda_t$ as the velocity scaling implied by the spacetime coordinate mapping. For the scaled problem to be an elastodynamic process, (2.28b) requires $\lambda_{c_1} = \lambda_{c_2}$. That is, the scaling of the elastic wave speeds due to scaling the material properties must match the velocity scaling implied by the scaling of the spacetime coordinates. From here on, we write this common scaling as $\lambda_c = \sqrt{\lambda_{\mathbf{C}}/\lambda_{\rho}}$.

In summary, the scaled system is an elastodynamic process if the scalings of the spacetime coordinates and the tensorial representations of the mechanical fields satisfy

$$\lambda_{\mathbf{x}} = \lambda_c \lambda_t, \quad (2.31a)$$

$$\lambda_{\bar{\mathbf{u}}} = \lambda_{\mathbf{u}} \quad \lambda_{\bar{\mathbf{v}}} = \lambda_{\mathbf{v}} = \frac{\lambda_{\mathbf{u}}}{\lambda_t} \quad \lambda_{\bar{\mathbf{E}}} = \lambda_{\mathbf{E}} = \frac{\lambda_{\mathbf{u}}}{\lambda_{\mathbf{x}}}, \quad (2.31b)$$

$$\lambda_{\bar{\mathbf{b}}} = \frac{\lambda_{\rho}\lambda_{\mathbf{u}}}{\lambda_t^2} \quad \lambda_{\bar{\boldsymbol{\sigma}}} = \lambda_{\boldsymbol{\sigma}} = \frac{\lambda_{\mathbf{C}}\lambda_{\mathbf{u}}}{\lambda_{\mathbf{x}}} \quad \lambda_{\bar{\mathbf{p}}} = \lambda_{\mathbf{p}} = \frac{\lambda_{\rho}\lambda_{\mathbf{u}}}{\lambda_t}. \quad (2.31c)$$

When working with forms, the same requirements simplify to

$$\lambda_{\mathbf{x}} = \lambda_c \lambda_t, \quad (2.32a)$$

$$\lambda_{\bar{\boldsymbol{\varepsilon}}} = \lambda_{\boldsymbol{\varepsilon}} = \lambda_{\mathbf{u}}, \quad (2.32b)$$

$$\lambda_{\bar{\mathbf{M}}} = \lambda_{\mathbf{M}} = \lambda_{\bar{\mathbf{b}}} := \frac{\lambda_{\rho}\lambda_{\mathbf{u}}\lambda_{\mathbf{x}}^d}{\lambda_t}. \quad (2.32c)$$

All the scaling values in (2.31) and (2.32) are written with respect to $\lambda_{\mathbf{C}}$, λ_{ρ} , λ_t and $\lambda_{\mathbf{u}}$. In fact, we can choose any other set of four scalings from which to derive the rest.

2.3.3 Elastodynamic cohesive processes: scalings, nondimensional groups and intrinsic scales

In this subsection, we discuss the scaling of elastodynamic cohesive processes and investigate their nondimensional groups. We also identify certain di-

mensional parameters as intrinsic scales, and we describe how each of these influences the elastodynamic cohesive response.

Scalings

Let $\{\mathbf{u}, \boldsymbol{\varepsilon}, \mathbf{M}, \mathcal{C}, \tilde{\mathbf{s}}, \bar{\mathbf{b}}, \bar{\mathbf{u}}, \bar{\boldsymbol{\varepsilon}}, \bar{\mathbf{M}}; (\mathbf{x}, t)\}$ be an elastodynamic cohesive process, and let $\{\mathbf{u}', \boldsymbol{\varepsilon}', \mathbf{M}', \mathcal{C}', \tilde{\mathbf{s}}', \bar{\mathbf{b}}', \bar{\mathbf{u}}', \bar{\boldsymbol{\varepsilon}}', \bar{\mathbf{M}}'; (\mathbf{x}', t')\}$ be a scaled system that is defined according to (2.18). We seek the conditions under which the scaled system is also an elastodynamic cohesive process; that is, in addition to the conditions for a general elastodynamic system, it must also satisfy (2.17) and (2.18). Recalling $\boldsymbol{\varepsilon}|_{\bar{\Gamma}} = \mathbf{v}|_{\bar{\Gamma}}$ and $\mathbf{M}|_{\bar{\Gamma}} = -\boldsymbol{\sigma}|_{\bar{\Gamma}}$, and according to (2.9), (2.13) and (2.32), we get

$$\lambda_{\tilde{\mathbf{s}}} = \lambda_{\bar{\mathbf{b}}}, \quad \lambda_{\bar{\boldsymbol{\varepsilon}}} = \lambda_{\bar{\mathbf{u}}}. \quad (2.33)$$

The cohesive scaling factors, $\lambda_{\tilde{\mathbf{s}}}$ and $\lambda_{\bar{\boldsymbol{\varepsilon}}}$, are natural choices for defining the scaling of an elastodynamic cohesive process. We must select two additional scaling factors to determine all the scaling factors in (2.31). Here, we choose two that govern the constitutive relation for the bulk material, λ_c and λ_ρ .

Nondimensional groups

We obtain a nondimensional representation of the solution by setting

$$\tilde{\mathbf{s}}' = \tilde{\boldsymbol{\sigma}} \quad \Leftrightarrow \quad \lambda_{\bar{\mathbf{b}}} = \lambda_{\mathbf{x}}^{d-1} \lambda_t \tilde{\boldsymbol{\sigma}}, \quad \lambda_{\bar{\boldsymbol{\varepsilon}}} = \tilde{\boldsymbol{\delta}}, \quad \lambda_c = c_0, \quad \lambda_\rho = \rho_0, \quad (2.34)$$

in which ρ_0 and c_0 are representative scales for the wave speed and mass density of the bulk material. From here on, we assume that the bulk material is homogeneous, and we set $\rho_0 = \rho$ and $c_0 = c_d$, where c_d is the dilatational wave speed,³

$$c_d = \max_{\mathbf{n}} \sqrt{\frac{C^{ijkl} n_i n_j n_k n_l}{\rho}} \quad \forall \mathbf{n} \quad \ni \quad n_i n_i = 1. \quad (2.35)$$

Equation (2.34) implies that $\tilde{\boldsymbol{\sigma}}' = \tilde{\boldsymbol{\delta}}' = 1$. Moreover, the wave speeds and the density are scaled by c_0 and ρ_0 , respectively. In particular, $c_d' = \rho' = 1$.

All the scales in (2.31) can be expressed in terms of those in (2.34). The

³However, we can extend our results to cover non-homogeneous materials by substituting c_0 and ρ_0 for c_d and ρ .

nondimensional, tensorial representation of the solution is

$$\mathbf{x}' = \frac{\mathbf{x}}{\tilde{\tau}c_d} \quad t' = \frac{t}{\tilde{\tau}}, \quad (2.36a)$$

$$\begin{aligned} \mathbf{u}' &= \frac{\mathbf{u}}{\tilde{\delta}} & \mathbf{v}' &= \frac{\mathbf{v}}{\tilde{v}} & \mathbf{E}' &= \frac{c_d}{\tilde{v}} \mathbf{E} \\ \bar{\mathbf{u}}' &= \frac{\bar{\mathbf{u}}}{\tilde{\delta}} & \bar{\mathbf{v}}' &= \frac{\bar{\mathbf{v}}}{\tilde{v}} & \bar{\mathbf{E}}' &= \frac{c_d}{\tilde{v}} \bar{\mathbf{E}}, \end{aligned} \quad (2.36b)$$

$$\begin{aligned} & & \mathbf{p}' &= \frac{c_d}{\tilde{\sigma}} \mathbf{p} & \boldsymbol{\sigma}' &= \frac{\boldsymbol{\sigma}}{\tilde{\sigma}} \\ \bar{\mathbf{b}}' &= \frac{\tilde{\tau}}{\rho\tilde{v}} \bar{\mathbf{b}} & \bar{\mathbf{p}}' &= \frac{c_d}{\tilde{\sigma}} \bar{\mathbf{p}} & \bar{\boldsymbol{\sigma}}' &= \frac{\bar{\boldsymbol{\sigma}}}{\tilde{\sigma}}, \end{aligned} \quad (2.36c)$$

where $\tilde{\tau}$ and \tilde{v} are intrinsic time and velocity scales associated with the TSR, as explained below. When working with forms, the same relations simplify to

$$\mathbf{x}' = \frac{\mathbf{x}}{\tilde{\tau}c_d} \quad t' = \frac{t}{\tilde{\tau}}, \quad (2.37a)$$

$$\mathbf{u}' = \frac{\mathbf{u}}{\tilde{\delta}} \quad \bar{\mathbf{u}}' = \frac{\bar{\mathbf{u}}}{\tilde{\delta}} \quad \boldsymbol{\varepsilon}' = \frac{\boldsymbol{\varepsilon}}{\tilde{\delta}} \quad \bar{\boldsymbol{\varepsilon}}' = \frac{\bar{\boldsymbol{\varepsilon}}}{\tilde{\delta}}, \quad (2.37b)$$

$$\bar{\mathbf{b}}' = \frac{\bar{\mathbf{b}}}{\tilde{m}} \quad \mathbf{M}' = \frac{\mathbf{M}}{\tilde{m}} \quad \bar{\mathbf{M}}' = \frac{\bar{\mathbf{M}}}{\tilde{m}}, \quad (2.37c)$$

where $\tilde{m} := \tilde{\sigma}\tilde{\tau}\tilde{L}^{d-1}$ is the cohesive model's intrinsic momentum scale, in which $\tilde{L} = c_d\tilde{\tau}$ is an intrinsic length scale for the cohesive process-zone size (see below).

Equation (2.36) demonstrates that the domain dimensions, the loads and the material properties must scale in a particular way to obtain a cohesive elastodynamic process. For example, the non-dimensional Dirichlet and Neumann boundary data, $\bar{\mathbf{v}}'$ and $\bar{\boldsymbol{\sigma}}'$, must always scale, respectively, with \tilde{v} and $\tilde{\sigma}$.

Let \bar{u} , \bar{v} , \bar{E} , \bar{p} , $\bar{\sigma}$ and \bar{b} be measures for the load data, $\bar{\mathbf{u}}$, $\bar{\mathbf{v}}$, $\bar{\mathbf{E}}$, $\bar{\mathbf{p}}$, $\bar{\boldsymbol{\sigma}}$ and $\bar{\mathbf{b}}$. Also, let L and T be length and time scales for the spacetime domain \mathcal{D} , and assume that the ratios, $\bar{u}/\tilde{\delta}$, \bar{v}/\tilde{v} , $c_d\bar{E}/\tilde{v}$, \bar{p}/\tilde{p} , $\bar{\sigma}/\tilde{\sigma}$, $\tilde{\tau}\bar{b}/\tilde{v}$, L/\tilde{L} and $T/\tilde{\tau}$, are fixed for a family of scalings of a given cohesive elastodynamic process. Then, according to our previous discussion, the family of scaled systems are cohesive elastodynamic processes with self-similar solutions. Furthermore, the listed ratios are the nondimensional groups that determine the elastodynamic response of TSR-based cohesive models.

Intrinsic cohesive scales

We showed in 2.2.5 that any two members of $\{\tilde{\sigma}, \tilde{\delta}, \tilde{\phi}\}$, in combination with the bulk material properties, ρ and c_d , are sufficient to describe the scaling properties of a TSR; *cf.* (2.20). Here we choose $\tilde{\sigma}$ and $\tilde{\delta}$ as the independent parameters. In general, $\tilde{\phi} = \gamma\tilde{\sigma}\tilde{\delta}$, in which the dimensionless factor γ depends on the choice of the independent cohesive scales and on the type of the cohesive model (see (2.70), for example). We simplify this relation for purposes of dimensional analysis to $\tilde{\phi} = \tilde{\sigma}\tilde{\delta}$. The dimensional parameters of the TSR are then, $\tilde{\sigma}$, $\tilde{\delta}$ and

$$\tilde{\phi} = \tilde{\sigma}\tilde{\delta}, \quad (2.38a)$$

$$\tilde{\tau} = \frac{\rho c_d \tilde{\delta}}{\tilde{\sigma}}, \quad (2.38b)$$

$$\tilde{v} = \frac{\tilde{\delta}}{\tilde{\tau}} = \frac{\tilde{\sigma}}{\rho c_d}, \quad (2.38c)$$

$$\tilde{E} = \frac{\tilde{v}}{c_d} = \frac{\tilde{\sigma}}{\rho c_d^2}, \quad (2.38d)$$

$$\tilde{p} = \rho \tilde{v} = \frac{\tilde{\sigma}}{c_d}, \quad (2.38e)$$

$$\tilde{L} = c_d \tilde{\tau} = \frac{\rho c_d^2 \tilde{\delta}}{\tilde{\sigma}} \propto \frac{\|\mathbf{C}\| \tilde{\phi}}{\tilde{\sigma}^2}. \quad (2.38f)$$

The second, alternative expression for \tilde{L} in (2.38f) arises from (2.38a) and the definition of c_d in 2.3.2. Next, we discuss the influence of the dimensional parameters on various aspects of the cohesive response.

The cohesive parameters and the bulk material properties determine the cohesive length scale, \tilde{L} . Although \tilde{L} and $\tilde{\delta}$ share a common dimension, length, they have distinct physical interpretations. The cohesive length scale \tilde{L} reflects the cohesive process-zone size, while the cohesive separation scale $\tilde{\delta}$ influences the amplitude of the displacement field. Both cohesive length scales are independent of the spatial length scale L of the analysis domain.

As will be shown in 2.4.2, the quasistatic process-zone size for an isotropic material is estimated by,

$$A^0 = \zeta \pi \frac{\mu}{1 - \nu} \left(\frac{\tilde{\phi}}{\tilde{\sigma}^2} \right) = \check{\zeta} \tilde{L}, \quad (2.39)$$

where μ and ν are the shear modulus and Poisson ratio, $\tilde{\sigma}$ is set equal to the cohesive strength and the constant factors, $\check{\zeta}$ and ζ , depend on the details of the TSR and on the convention that defines the process-zone size. The process-zone size in the dynamic setting is proportional to Λ^0 , and we discuss its dependence on crack speed in section 2.4.2.

We present a rate-dependent interfacial damage model in chapter 4 that is governed by the cohesive strength and time scales, $\tilde{\sigma}$ and $\tilde{\tau}$. A similar dimensional analysis of that model generates a cohesive separation scale $\tilde{\delta}$ through (2.38b), and the relations in (2.36) and (2.38) hold as well. In contrast to the present analysis of TSR-based cohesive models, in which the cohesive separation scale $\tilde{\delta}$ is an independent parameter and the cohesive time scale $\tilde{\tau}$ is a derived quantity that depends on the loading, $\tilde{\delta}$ derives from $\tilde{\tau}$ and other independent parameters in the rate-dependent model. Although the same relation (2.38b) holds in both cases, the differences in the dependency relations between the scales in the two models result in distinct cohesive behaviors and distinct crack-tip dynamics. We will explore this issue in greater detail in subsequent publications.

The above equations and cohesive scales are valid for general mixed-mode conditions. While they remain valid for single-mode problems, different choices for the wave speeds and cohesive parameters that define the cohesive scales might be more appropriate in particular setting. For example, in pure mode-II and mode-III settings, the shear-wave speed c_s is the natural choice for the wave speed, and we substitute c_s for c_d in all equations following (2.35). Moreover, the appropriate normal or tangential components of cohesive traction and separation should be used for $\tilde{\sigma}$ and $\tilde{\delta}$ in each case.

Next, we hold fixed the material parameters, \mathbf{C} and ρ , and hence the wave speeds, to investigate the influence of the cohesive parameters in (2.38) on the system response. Consequently, the pairs $(\tilde{\tau}, \tilde{L})$ and $(\tilde{\sigma}, \tilde{v})$ are interchangeable for this study. Subject to these conditions, we categorize the applied loads in (2.36) into three groups, each with a distinct scaling. First, the initial displacement $\bar{\mathbf{u}}$ scales with $\tilde{\delta}$; second, the body force $\bar{\mathbf{b}}$ is proportional to $\rho\tilde{v}/\tilde{\tau}$; and third, all boundary conditions as well as the initial linear momentum density and the initial strain are proportional to $\tilde{\sigma}$.

We next consider the cohesive scales, $\tilde{\tau}$, $\tilde{\sigma}$, $\tilde{\delta}$ and $\tilde{\phi}$, and discuss the impact on the system scalings when the bulk material parameters and one cohesive scale are held fixed and the others are allowed to vary, for constant bulk

material parameters, ρ and c_d . First, let the cohesive time scale $\tilde{\tau}$ be fixed, and let the separation scale $\tilde{\delta}$ vary. This corresponds to uniform scaling of the TSR on both the separation and stress axes, because fixed $\tilde{\tau}$ implies $\tilde{\sigma} \propto \tilde{\delta}$. We also have $\tilde{v} \propto \tilde{\delta}$ and $\tilde{\phi} \propto \tilde{\delta}^2$. By construction and by (2.31a), the spatial and temporal dimensions of the domain are unchanged. However, all of the load values scale linearly with $\tilde{\delta}$.

Second, we consider the case where $\tilde{\sigma}$ is fixed and $\tilde{\delta}$ is varied. This corresponds to scaling the separation axis in a graph of the TSR. In this case, $\tilde{L}, \tilde{\tau}, \tilde{\phi} \propto \tilde{\delta}$, and the displacement and initial-displacement fields (2.36b) also scale linearly with $\tilde{\delta}$. That is, both the undeformed and deformed spacetime configurations as well as the temporal axis scale proportionally to $\tilde{\delta}$, so that $\boldsymbol{\varepsilon}$ and \boldsymbol{M} do not change. This invariance is also evident in the initial–boundary conditions, which are unchanged. The body force $\bar{\mathbf{b}}$, however, scales as $1/\tilde{\delta}$.

Next, we vary $\tilde{\sigma}$ with $\tilde{\delta}$ held fixed. This yields $\tilde{\phi} \propto \tilde{\sigma}$ and $\tilde{L}, \tilde{\tau} \propto 1/\tilde{\sigma}$. Now the scaling is on the stress axis of the TSR graph, with the separation axis fixed. Clearly, the displacement and the initial displacement do not change. However, all of the other initial–boundary conditions scale linearly with $\tilde{\sigma}$, and we have $\bar{\mathbf{b}} \propto \tilde{\sigma}^2$.

Finally, we consider the case where $\tilde{\phi}$ is fixed. This situation has significant practical importance, since we are often able to measure directly a material’s specific fracture energy, from which we can compute $\tilde{\phi}$. We must then identify the remaining cohesive parameters with the computed value of $\tilde{\phi}$ held fixed (*cf.* section 2.5.1). Let $\tilde{\sigma}$ be the control for the remaining cohesive parameters. Then $\tilde{v} \propto \tilde{\sigma}$, $\tilde{\delta} \propto 1/\tilde{\sigma}$, and $\tilde{\tau}, \tilde{L} \propto \tilde{\sigma}^{-2}$. The displacement solution and the initial displacements are proportional to $1/\tilde{\sigma}$, while the spatial and temporal coordinates scale as $1/\tilde{\sigma}^2$. All initial–boundary conditions scale linearly with $\tilde{\sigma}$, and $\bar{\mathbf{b}} \propto \tilde{\sigma}^3$.

2.4 Comparative analyses of cohesive and linear elastic models of dynamic fracture

The asymptotic, crack-tip-stress and velocity solutions for a dynamically propagating crack obtained from *Linear Elastic Fracture Mechanics* (LEFM) both exhibit $r^{-1/2}$ singular behavior, where r is the radial distance from the crack tip [9]. This implies infinite stress and material velocity, in the

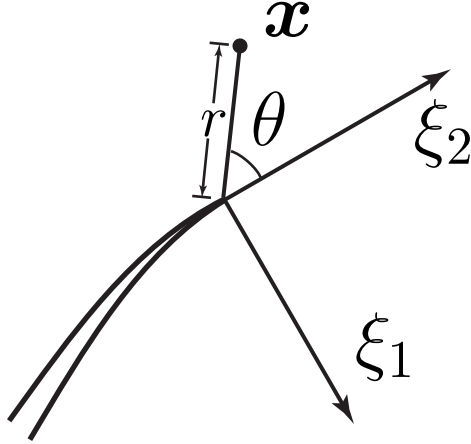


Figure 2.3: Local coordinate system at a crack tip.

limit, as $r \rightarrow 0$, a non-physical finding. *Cohesive Fracture Mechanics* (CFM) remedies this problem by limiting tractions acting across *cohesive interfaces* that model the fracture process. Clearly, the CFM solution differs within a *cohesive process zone* (CPZ) from the LEFM solution in the same region. However, the CFM solution should agree with the asymptotic LEFM fields at locations that are sufficiently remote from the CPZ when the CPZ size is much smaller than the length scale of the singularity-dominant zone in the LEFM solution. Thus, the gross solution features and the crack paths predicted by the two models might be similar. As the size of the CPZ increases relative to the scale of the singular-dominant LEFM zone, we expect larger discrepancies between the two solutions. In this section, we develop and compare the relevant length scales for the two models.

2.4.1 LEFM solution at a moving crack tip

Figure 2.3 depicts an instantaneous, local coordinate system at a crack tip moving with speed \hat{v} in the ξ_2 direction, with the ξ_1 direction normal to the crack surface. The cylindrical coordinates of a point \mathbf{x} are (r, θ) , in which r is the radial distance from the crack tip and the angle θ is measured counter-clockwise relative to the ξ_2 axis. The material is assumed to be isotropic. We restrict our attention to the in-plane fracture modes, $\{I, II\} = \{(1), (2)\}$, *cf.* 2.2.5. Pure mode-*I* behavior is implied whenever the directions and modes are not indicated explicitly.

Asymptotic expansion of the stress field

The leading term in the asymptotic expansion of the crack-tip stress field is summarized as [9],

$$\underline{\sigma}^{ij}(r, \theta, t) = \frac{K_I(t)}{\sqrt{2\pi r}} \Sigma_I^{ij}(\theta, \hat{v}) + \frac{K_{II}(t)}{\sqrt{2\pi r}} \Sigma_{II}^{ij}(\theta, \hat{v}) \quad \text{as } r \rightarrow 0, \quad (2.40)$$

where $K_I(t)$ and $K_{II}(t)$ are the *modal dynamic stress intensity factors* for in-plane opening (mode-*I*) and shearing (mode-*II*), the components are referenced to the local coordinate frame, and \hat{v} is the crack-tip speed. The stress intensity factors are identified by

$$K_I(t) = \lim_{\xi_2 \rightarrow 0} \sqrt{2\pi \xi_2} \underline{\sigma}^{11}(\xi_2, 0, t), \quad K_{II}(t) = \lim_{\xi_2 \rightarrow 0} \sqrt{2\pi \xi_2} \underline{\sigma}^{12}(\xi_2, 0, t). \quad (2.41)$$

The functions, $\Sigma_I^{ij}(\theta, \hat{v})$ and $\Sigma_{II}^{ij}(\theta, \hat{v})$, describe the angular dependence of the stress components for any given crack-tip speed, and are given by

$$\Sigma_I^{11} = -\frac{1}{D} \left\{ (1 + \alpha_2^2)^2 \frac{\cos \frac{1}{2}\theta_1}{\sqrt{\gamma_1}} - 4\alpha_1\alpha_2 \frac{\cos \frac{1}{2}\theta_2}{\sqrt{\gamma_2}} \right\}, \quad (2.42a)$$

$$\Sigma_I^{12} = \frac{2\alpha_1(1 + \alpha_2^2)}{D} \left\{ \frac{\sin \frac{1}{2}\theta_1}{\sqrt{\gamma_1}} - \frac{\sin \frac{1}{2}\theta_2}{\sqrt{\gamma_2}} \right\}, \quad (2.42b)$$

$$\Sigma_I^{22} = \frac{1}{D} \left\{ (1 + \alpha_2^2)(1 + 2\alpha_1^2 - \alpha_2^2) \frac{\cos \frac{1}{2}\theta_1}{\sqrt{\gamma_1}} - 4\alpha_1\alpha_2 \frac{\cos \frac{1}{2}\theta_2}{\sqrt{\gamma_2}} \right\}, \quad (2.42c)$$

and

$$\Sigma_{II}^{11} = \frac{2\alpha_2(1 + \alpha_2^2)}{D} \left\{ \frac{\sin \frac{1}{2}\theta_1}{\sqrt{\gamma_1}} - \frac{\sin \frac{1}{2}\theta_2}{\sqrt{\gamma_2}} \right\}, \quad (2.43a)$$

$$\Sigma_{II}^{12} = \frac{1}{D} \left\{ 4\alpha_1\alpha_2 \frac{\cos \frac{1}{2}\theta_1}{\sqrt{\gamma_1}} - (1 + \alpha_2^2)^2 \frac{\cos \frac{1}{2}\theta_2}{\sqrt{\gamma_2}} \right\}, \quad (2.43b)$$

$$\Sigma_{II}^{22} = -\frac{2\alpha_2}{D} \left\{ (1 + 2\alpha_1^2 - \alpha_2^2) \frac{\sin \frac{1}{2}\theta_1}{\sqrt{\gamma_1}} - (1 + \alpha_2^2) \frac{\sin \frac{1}{2}\theta_2}{\sqrt{\gamma_2}} \right\}, \quad (2.43c)$$

in which

$$\alpha_k = \sqrt{1 - \hat{v}^2/c_k^2} \quad (2.44a)$$

$$\gamma_k = \sqrt{1 - (\hat{v} \sin \theta/c_k)^2} \quad (2.44b)$$

$$\tan \theta_k = \alpha_k \tan \theta, \quad k = 1, 2, \quad (2.44c)$$

$$D = 4\alpha_1\alpha_2 - (1 + \alpha_2^2)^2. \quad (2.44d)$$

The reference velocities, $c_1 := c_d$ and $c_2 := c_s$, are the dilatation and shear wave speeds, which for an isotropic, linearly elastic material with Lamé parameters, λ and μ , are given by

$$c_d = \sqrt{\frac{\lambda + 2\mu}{\rho}}, \quad c_s = \sqrt{\frac{\mu}{\rho}}. \quad (2.45)$$

The *Rayleigh wave speed*, denoted by c_R , is computed as the non-zero speed \hat{v} at which D vanishes, where, in general, \hat{v} need not be associated with a crack-tip speed. However, in the present context, it is clear that D vanishes as the crack-tip speed approaches the Rayleigh wave speed.

Equations (2.41) and (2.40) imply,

$$\Sigma_I^{11}(0, \hat{v}) = 1, \quad \Sigma_{II}^{12}(0, \hat{v}) = 1, \quad (2.46)$$

which is easily verified using (2.42) and (2.43). It is customary to decorate α , θ and γ with d and s , similarly to c_d and c_s . However, we use instead the indices 1 and 2, since the displacements for dilatational and shear waves are purely in the ξ_1 and ξ_2 directions, respectively. Many relations, such as (2.44c), can be written in a more compact form when expressed with this convention.

Radii of singularity

Asymptotic solutions in dynamic LEFM are generally based on the representation of a given problem, defined for specified far-field loads acting on a cracked body, as the superposition of two simpler subproblems [9]. In the first subproblem, the far-field loading acts on an un-cracked body with geometry and material properties that are otherwise identical to the original cracked body. The second subproblem involves the cracked geometry sub-

jected to traction loads that cancel the crack-face tractions that would be generated by the stress solution from the first subproblem if it acted on the cracked geometry. Thus, the superposition of the two subproblems provides, by construction, a solution that satisfies the traction-free condition on the crack faces. If, in addition to far-field loads, the original problem involves tractions that act directly on the evolving crack faces, then these loads are added to the second subproblem.

Since the solution to the first subproblem exhibits no singular response, the second subproblem captures entirely the singular response of the original system. Thus, the second problem alone suffices for asymptotic studies of the crack-tip fields. Equation (2.40) gives the leading singular term in the asymptotic expansion of the crack-tip stress field, which is $\mathcal{O}(r^{-1/2})$. The second term in the expansion is spatially uniform, and therefore zeroth-order in r . For very small values of r , the singular term dominates the stress solution. However, as r increases, the singular term trends toward zero, so that the zeroth-order term, and eventually higher-order terms, become dominant.

We are interested in quantifying the critical radii below which the singular terms dominate the rest of the stress solution, and we refer to these as the *radii of singularity*. In general, the radii of singularity vary with the angle θ . However, it is convenient and sufficient to consider only $\theta = 0$, *i.e.*, the direction directly ahead of the crack tip, to establish an overall scale for the singular zone. In particular, we use $r_{(k)}(t)$ to denote the radius of singularity for mode- (k) response at time t and for $\theta = 0$. Let $\check{\sigma}_k(t); k = 1, 2$ denote the limiting values, as $r \rightarrow 0$, of the normal and tangential components of the prescribed crack-face tractions in the second subproblem. It turns out that these limiting values determine the zeroth-order terms in the asymptotic expansions for the normal components (*i.e.*, $\underline{\sigma}^{11}$ and $\underline{\sigma}^{12}$) of the crack-tip stress field [9]. That is, $\underline{\sigma}_0^{1k}(t) = \check{\sigma}_k(t)$, in which a subscript ‘0’ indicates a zeroth-order term in an asymptotic expansion.

We identify the radii of singularity by equating the leading singular terms, evaluated at $(r, \theta, t) = (r_{(k)}(t), 0, t)$ with the corresponding zeroth-order terms. Then, recalling (2.40) and (2.46), we have

$$\begin{aligned} \frac{|K_{(k)}(t)|}{\sqrt{2\pi r_{(k)}(t)}} |\Sigma_{(k)}^{1k}(0, \hat{v})| &= \frac{|K_{(k)}(t)|}{\sqrt{2\pi r_{(k)}(t)}} = |\check{\sigma}_k(t)| \\ \Rightarrow r_{(k)}(t) &:= \frac{1}{2\pi} \left(\frac{K_{(k)}(t)}{\check{\sigma}_k(t)} \right)^2. \end{aligned} \quad (2.47)$$

From here on, we suppress the temporal arguments of $r_{(k)}$ and $\check{\sigma}_k$ for convenience.

Energy release rate

The *dynamic energy release rate*, G , is defined as the rate of mechanical energy outflow from the body into the crack tip per unit crack advance. It is computed as a function of the instantaneous crack speed and the modal, dynamic stress-intensity factors [9]:

$$G = \frac{1 - \nu}{2\mu} [A_I(\hat{v})K_I^2 + A_{II}(\hat{v})K_{II}^2], \quad (2.48)$$

where

$$A_{(k)}(\hat{v}) = \frac{(1 - \alpha_2^2)\alpha_k}{(1 - \nu)D} = \frac{\hat{v}^2\alpha_k}{(1 - \nu)c_2^2 D}. \quad (2.49)$$

The functions $A_{(k)}$ are universal functions that do not depend on the details of the loading or on the domain geometry. These functions have the properties, $A_{(k)} \rightarrow 1$ as $\hat{v} \rightarrow 0^+$ and $A_{(k)} = O[(c_R - \hat{v})^{-1}]$ as $\hat{v} \rightarrow c_R$, and are monotone between 0^+ and c_R .

We obtain a relation between r_I and r_{II} , for general mixed-mode loading, by combining (2.47) and (2.48). We are, however, more interested in the pure mode-*I* and mode-*II* cases, *cf.* 2.4.2, where the modal radii of singularity are given independently by,

$$r_{(k)} = \frac{1}{\pi(1 - \nu)} \frac{\mu G}{A_{(k)}(\hat{v})\check{\sigma}_k^2}. \quad (2.50)$$

2.4.2 Cohesive fracture mechanics solution

In this section, we discuss the concept of small-scale yielding as it applies to cohesive models within the context of LEFM. Later, we compare the length scales associated with each model and discuss the validity of the small-scale-

yielding assumption.

Small-scale-yielding assumption

The stress solution from LEFM theory predicts unbounded stresses near the crack tip, in the limit, as $r \rightarrow 0$. Clearly, this is a mathematical idealization, since real materials cannot withstand such stresses. Nonetheless, LEFM solutions provide useful information when the size of the region within which the material behavior deviates from linear elasticity is very small compared to the other length scales in the model [9]. That is, when the *small-scale-yielding* (SSY) assumption holds. Under such circumstances, plastic flow or some other inelastic process determines the stress values within the process zone, where the material response is nonlinear [9]. Cohesive models provide one means to describe the nonlinear material behavior within the process zone. The dominant singular terms from LEFM theory accurately describe the response of materials that conform to the SSY assumption outside, but close to, the process zone. These singular fields can be fully characterized using dynamic stress intensity factors.

Geometry of the cohesive process zone

Cohesive models replace a mathematically sharp crack tip with a cohesive process zone (CPZ) that takes the form of a vertical spacetime d -manifold with finite size, but in general, no clear boundary. The crack-tip position is similarly ill-defined. We next introduce conventions to address these ambiguities for cohesive models in two spatial dimensions, where a single point suffices to describe the crack tip and the leading and trailing boundaries of the process zone.

We define the *nominal crack-tip position*, denoted by \mathbf{x}_c , as the location where the critical cohesive separation $\tilde{\delta}$, corresponding to the cohesive strength $\tilde{\sigma}$ in the TSR, is attained. The *trailing edge of the CPZ*, denoted by \mathbf{x}_T , is the position behind the crack tip where the cohesive tractions first vanish. This location is not well defined in TSRs where the tractions only vanish asymptotically for large separations. In such cases, we identify \mathbf{x}_T with the location where $\llbracket \mathbf{u} \rrbracket_{\tilde{r}} = \delta_T > \tilde{\delta}$, such that the cohesive traction falls to 1% of the strength $\tilde{\sigma}$. In general, the leading edge of the CPZ, denoted by \mathbf{x}_L , is identified by the condition, $\llbracket \mathbf{u} \rrbracket_{\tilde{r}} = \delta_L$, where δ_L is the smallest co-

hesive separation at which significant crack-like behavior (*i.e.*, large strains and velocities) is observed. Following common practice, we set $\delta_L = \tilde{\delta}$.

The *nominal CPZ* is the segment of the cohesive interface between \mathbf{x}_T and \mathbf{x}_L . The *nominal CPZ size* is given by $\Lambda = |\mathbf{x}_L - \mathbf{x}_T|$. Although there is a level of arbitrariness in these definitions, we note that reasonable alternative definitions for \mathbf{x}_L and \mathbf{x}_T generally scale Λ by a factor that is only $\mathcal{O}(1)$. We use $\Lambda_{(k)}$ to denote the modal CPZ sizes. The SSY condition, in the context of CFM, is expressed as,

$$\Lambda_{(k)} \ll r_{(k)} \quad k = 1, \dots, d. \quad (2.51)$$

Process-zone size estimates

There are several estimates in the literature for the modal process-zone sizes under quasi-static conditions [19, 20]. For isotropic materials, and recalling (2.39), they can be presented in the combined form,

$$\Lambda_{(k)}^0 = \zeta_{(k)} \pi \frac{\mu}{1 - \nu} \frac{\tilde{\phi}_{(k)}}{(\tilde{\sigma}_{(k)})^2}, \quad (2.52)$$

in which $\tilde{\sigma}_{(k)}$ and $\tilde{\phi}_{(k)}$ denote the cohesive strength and the work of separation for mode (k), and superscript ‘0’ indicates a quasi-static value. The value of the scalar factor $\zeta_{(k)}$ depends on the choice of TSR and on the convention employed in the definition of process-zone size. For instance, Rice [19] estimated $\zeta_{(1)} = 1/4$ for the Dugdale model [7], and proposed $\zeta_{(1)} = 9/16$ for potential-based TSRs [20].

One can show, using the methods advanced in [9], that for any extrinsic cohesive model subject to SSY and steady-state crack growth conditions,

$$\Lambda_{(k)} = \frac{\Lambda_{(k)}^0}{A_{(k)}(\hat{v})}. \quad (2.53)$$

Then, combining (2.52) and (2.53), we obtain

$$\Lambda_{(k)} = \zeta_{(k)} \pi \frac{\mu}{1 - \nu} \frac{\tilde{\phi}_{(k)}}{(\tilde{\sigma}_{(k)})^2 A_{(k)}(\hat{v})}. \quad (2.54)$$

In view of the behavior of $A_{(k)}(\hat{v})$ (*cf.* discussion in 2.4.1), (2.54) implies that the CPZ size approaches zero as $\hat{v} \rightarrow c_R$. Yu and Suo [21], using an

eigenvalue expansion of the solution around the crack tip, obtained results for more general crack velocities and loadings that agree with the results in (2.52) and (2.53).

Although the CPZ-size estimate (2.54) is based on an assumption of steady-state crack propagation, it is expected to remain valid for unsteady conditions when the CPZ size is small compared to the overall crack length and when the normalized crack speed, \hat{v}/c_R , does not change appreciably during crack extensions on the order of the CPZ-size [9]. Our numerical results, presented in 2.5, support this expectation under typical conditions and suggest that these relations also hold for intrinsic cohesive models. However, we find that (2.54) loses accuracy as the SSY assumption loses validity or when the above condition on normalized crack speed is violated. Even in these extreme situations, the relation between CPZ size and crack-tip speed is qualitatively similar to the one predicted by (2.54). We discuss this matter in more detail in 2.5.3.

2.4.3 Interplay between the length scales of cohesive models and LEFM

In this section, we study the dependence of the radii of singularity and the CPZ size on crack speed. This provides a basis for understanding the conditions under which the SSY assumption and, therefore, LEFM models of dynamic fracture are valid.

Energy release rate and the work of separation

Let us assume that the SSY assumption holds, so that the CPZ is entirely embedded within the singularity-dominant region of LEFM. Let us denote the separation by δ_k and the corresponding cohesive stress by $\sigma(\delta_k)$. Under these conditions, we have [9],

$$G = \frac{1}{\hat{v}} \int_{-A(k)}^0 \sigma(\delta_k) \frac{\partial \delta_k}{\partial t} dx + \int_0^{\delta_T} \sigma(\delta_k) d\delta_k = I_t + \tilde{\phi}_{(k)}, \quad (2.55)$$

where δ_T is the nominal separation at which the cohesive tractions vanish. The second integral is the work of separation; *cf.* (2.19). The first integral, denoted by I_t , represents the contributions of transient variations in the

separation observed in a moving coordinate frame attached to the crack-tip position. It vanishes identically for steady-state response, where we find, $G = \tilde{\phi}_{(k)}$. We can also neglect the contribution of I_t under transient conditions as $\hat{v} \rightarrow c_R$, since then $\Lambda_{(k)} \rightarrow 0$ (*cf.* section 2.4.2). In fact, employing the estimate (2.54), we get,

$$\left| \frac{I_t}{\tilde{\phi}_{(k)}} \right| \leq \frac{\tilde{\sigma}_{(k)} \Lambda_{(k)}^0}{\hat{v} \tilde{\phi}_{(k)}} \left| \frac{\partial \delta_k}{\partial t} \right|_{\infty} \approx \frac{\zeta_{(k)} \pi \mu}{(1 - \nu) \hat{v} \Lambda_{(k)}(\hat{v}) \tilde{\sigma}_{(k)}} \left| \frac{\partial \delta_k}{\partial t} \right|_{\infty}. \quad (2.56)$$

This upper bound vanishes, in the limit, as $\hat{v} \rightarrow c_R$, due to the properties of $\Lambda_{(k)}$. Consequently, while I_t can contribute a significant part of G at small crack speeds, it can be ignored at higher crack velocities. That is, approximating G with $\tilde{\phi}_{(k)}$ is well justified, except when $\hat{v}/c_R \ll 1$.

Influence of stress on characteristic lengths

The CPZ is entirely embedded within the region where the singular terms dominate, according to the SSY assumption, (2.51). Although the singular fields are not valid within the CPZ, we expect them to be accurate elsewhere in the domain. Through equations (2.50) and (2.54) we get,

$$\frac{\Lambda_{(k)}}{r_{(k)}} = \zeta_{(k)} \pi^2 \frac{\tilde{\phi}_{(k)}}{G} \left(\frac{\check{\sigma}_k}{\tilde{\sigma}_{(k)}} \right)^2. \quad (2.57)$$

Following the above discussion, $\tilde{\phi}_{(k)}/G \approx 1$ for steady state crack propagation or when $\hat{v}/c_R \rightarrow 1$. Under these conditions, the main factor that determines $\Lambda_{(k)}/r_{(k)}$ is the ratio, $\check{\sigma}_k/\tilde{\sigma}_{(k)}$, which is relatively independent of the crack speed, especially as $\hat{v} \rightarrow c_R$.

Relations similar to (2.57) can be found in the literature. For example, Freund [9] studies the problem of a stress wave with magnitude $\check{\sigma}$ impinging on a crack within an infinite, elastoplastic domain with yield strength $\tilde{\sigma}$. He shows that the plastic-yield region is entirely contained within the crack-tip singular fields when the ratio of $\check{\sigma}/\tilde{\sigma} \leq 0.2$, and obtains a similar relation between Λ/r and $(\check{\sigma}/\tilde{\sigma})^2$.

The ratio $\Lambda_{(k)}/r_{(k)}$ can serve as an indicator for the validity of the SSY assumption. As $\check{\sigma}_k/\tilde{\sigma}_{(k)}$ increases, the CPZ covers larger parts of the singularity dominant zone, and the LEFM theory gradually loses accuracy. This finding is similar to the small-scale yielding result for plastic-zone size based

on the strip-yield model [9, 19].

There is a close connection between $\check{\sigma}_k/\check{\sigma}_{(k)}$ and $\bar{\sigma}/\check{\sigma}$, which appears as a nondimensional parameter in section 2.3.3. Both reflect the ratio of the loading to the cohesive strength. In the context of TSR models, either one can serve as an indicator that reflects the discrepancy between the LEFM and CFM solutions.

2.5 Numerical parametric study of the CFM model

This section presents a numerical, parametric study of the behavior of a TSR-based cohesive model for mode- I , dynamic fracture. From here on, we drop for simplicity the subscript (1) that indicates a mode- I quantity. A full study would require independent investigations of all the relevant dimensionless groups in the cohesive model, including ratios of the loads to the cohesive strength and critical cohesive separation (*e.g.*, $\bar{\sigma}/\check{\sigma}$ and $\bar{u}/\check{\delta}$) and ratios of the spatial and temporal scales for the macroscopic domain and the cohesive model (*e.g.*, L/\check{L} and $T/\check{\tau}$) (*cf.* section 2.3.3). We focus our study on the influence of the load parameter, $\bar{\sigma}/\check{\sigma}$.

We use semi-analytical results for the LEFM model as reference solutions and highly-resolved numerical solutions to represent the behavior of the CFM model. In the latter case, we choose the extent of the spatial domain to be large enough, for a given analysis duration, to prevent reflected waves from affecting the cohesive response.

As described in 2.4.3, the parameter $\bar{\sigma}/\check{\sigma}$ controls the normalized CPZ-size, $\Lambda_{(k)}/r_{(k)}$, and, therefore, provides a suitable indicator for the validity of the SSY-assumption in the LEFM theory. As $\bar{\sigma}/\check{\sigma}$ increases, LEFM models lose accuracy in their rendering of the cohesive crack-tip fields and of various derived solution features, such as crack speed and trajectory. We report in detail how changes in $\bar{\sigma}/\check{\sigma}$ cause the LEFM and CFM solutions to diverge.

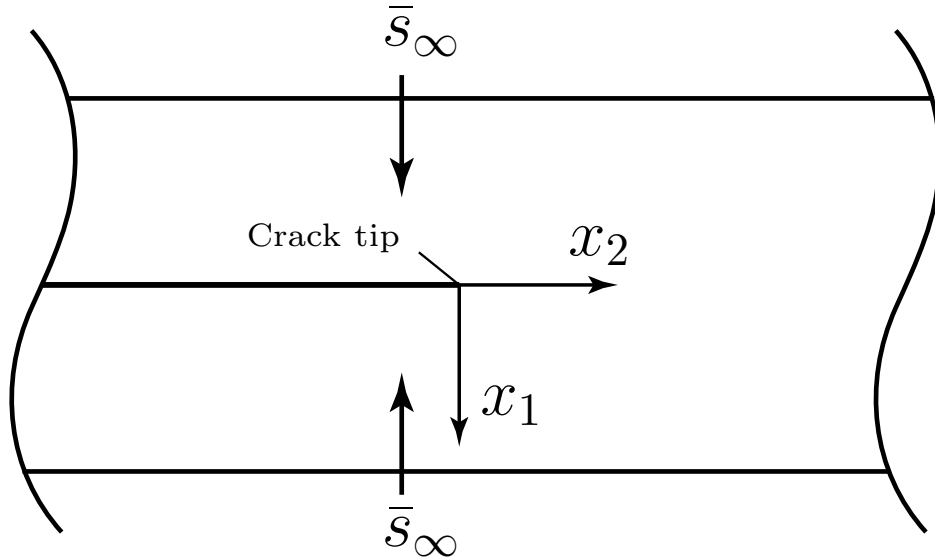


Figure 2.4: Infinite domain containing a half-plane crack.

2.5.1 Reference LEFM solution for an infinite plate

Domain and loading description

Figure 2.4 shows a plate that contains a half-plane crack, but that is otherwise unbounded, subjected to plane stress loading. We introduce the spatial coordinates, (x_1, x_2) , so that the x_1 -direction is normal to the crack plane, $x_1 = 0$, in \mathbb{E}^2 and the negative part of the x_2 -axis coincides with the crack surface at the initial time when the crack tip is coincident with the origin of the spatial coordinate system. We prescribe traction-free conditions on the crack faces at all times and a spatially uniform, mode- I traction, \bar{s}_∞ , as the far-field loading. The far-field tractions act suddenly and generate sharp wavefronts that approach the crack plane from both sides to arrive at time $t = 0$.

Stress intensity factor

The stress intensity factors for this problem are computed from the superposition of two subproblems; *cf.* [9] and 2.4.1. In the first subproblem, the far-field loading acts on an un-cracked body which is otherwise identical to the original cracked body. Additive interference between the two incident waves generates a spatially uniform tensile stress, $2H(t)\bar{s}_\infty$, on the entire

$x_1 = 0$ plane. Given the uncracked geometry and the spatially uniform loading, the stress intensity factor for the first subproblem is zero. In the second subproblem, which has the same cracked geometry as the original problem, compressive tractions with intensity

$$\bar{s}(t) = 2H(t)\bar{s}_\infty \quad (2.58)$$

act uniformly on the crack faces, so that \bar{s}_∞ determines the stress intensity factor in the second subproblem for $t > 0$; cf. 2.4.1. Furthermore, the limiting magnitude of the compressive traction acting on the trailing faces of the crack, as $r \rightarrow 0$, is simply, $\check{\sigma}(t) = \bar{s}(t)$. The superposition of the two subproblems yields the desired traction-free condition on the crack faces. Consequently, the dynamic stress intensity factor for the original problem is equal to that of the second subproblem.

The scale of the traction loading for the second subproblem is $\bar{\sigma} = 2\bar{s}_\infty$ (cf. section 2.3.3). We define the *normalized load intensity* as,

$$\sigma' := \frac{\bar{\sigma}}{\check{\sigma}} = 2\frac{\bar{s}_\infty}{\check{\sigma}} \quad \Rightarrow \quad \frac{\check{\sigma}(t)}{\check{\sigma}} = \frac{\bar{s}(t)}{\check{\sigma}} = 2H(t)\frac{\bar{s}_\infty}{\check{\sigma}} = \sigma'H(t). \quad (2.59)$$

Together, equations (2.57) and (2.59) imply that the normalized load intensity σ' governs the size ratio Λ/r .

The following identity holds for general loading conditions [9],

$$K_I(t, a, \hat{v}) = k(\hat{v})K_I(t, a, 0), \quad (2.60)$$

where $K_I(t, a, 0)$, is the stress intensity factor that would result from the same applied loading if the crack tip were stationary at the instantaneous position corresponding to the crack length a . The function $k(\hat{v})$, a universal function of crack-tip speed for mode-I crack growth, is independent of the loading and the geometry of the body. A useful approximation to $k(\hat{v})$ for most practical purposes is $k(\hat{v}) \approx (1 - \hat{v}/c_R)\sqrt{1 - \hat{v}/c_d}$. For the spatially uniform crack-face loading $\bar{s}(t)$, we have [9, 22],

$$K_I(t, a, 0) = C_I\sqrt{2\pi c_d} \int_{-\infty}^t \bar{s}'(z)\sqrt{t-z} dz, \quad (2.61)$$

where $C_I = \sqrt{2(1-2\nu)}/\pi(1-\nu) = 2c_s/(\pi c_d\sqrt{1-\nu})$ and \bar{s}' is to be inter-

preted as a distributional derivative.

Crack-growth criterion and crack-tip equation of motion for the LEFM model

In order to predict the trajectory of a moving crack with LEFM theory, we must augment the governing equations with an extrinsic *crack-growth criterion*, stated as a physical postulate for the material behavior that is distinct from the governing postulates for momentum balance, kinematic compatibility and the bulk constitutive relations [9]. The most common criterion is the *generalized Griffith's critical energy-release-rate criterion*, which states that the crack grows in a manner such that the dynamic energy release rate always equals the material's fracture energy. A crack will remain stationary or arrest if this requirement cannot be satisfied. The former quantity is a function of the crack-tip solution fields and the crack-tip velocity, as is evident in (2.48). The latter quantity is a property of the material, and it characterizes the material's resistance to crack growth.

In the simplest case, the amount of energy required to advance the crack per unit area of new crack surface is a constant, denoted by Γ_0 and called the *specific fracture energy*. Consequently, the kinetics of crack growth are governed by the *crack-tip equation of motion*,

$$G = \Gamma_0, \tag{2.62}$$

cf. (2.48). Combining (2.55) and (2.62), we obtain a relation between the specific fracture energy Γ_0 and the modal works of separation $\tilde{\phi}$, subject to pure-mode-loading and SSY assumptions. In particular, $\Gamma_0 = \tilde{\phi}$ for steady-state crack growth, and $\Gamma_0 \rightarrow \tilde{\phi}$, in the limit, as $\hat{v} \rightarrow c_R$, as explained in 2.4.3. Consequently, we construct the reference LEFM solution by setting $\Gamma_0 = \tilde{\phi}$. In the CFM framework, the identification, $\Gamma_0 = \tilde{\phi}$, follows directly from considerations of energy-balance, and does not require the application of an extrinsic, Griffith-type criterion.

We expect the solution from the CFM model to match the LEFM reference solution, in the limit, as $\sigma' \rightarrow 0$, since this condition implies that $\Lambda/r \rightarrow 0$. We also expect the CFM solution to deviate from the reference when the underlying assumptions that justify LEFM theory are invalid; that is, when the SSY assumption does not hold, when the crack motion is highly

unsteady, or when the unsteady crack speed is small relative to c_R .

Equations (2.60) and (2.62) yield,

$$\frac{1-\nu}{2\mu} A_I(\hat{v}) k(\hat{v})^2 [K_I(t, a, 0)]^2 = \Gamma_0 \quad (2.63a)$$

$$\Leftrightarrow g(\hat{v}) = \frac{2\mu\Gamma_0}{(1-\nu) [K_I(t, a, 0)]^2}, \quad (2.63b)$$

where $g(\hat{v}) := A_I(\hat{v})k(\hat{v})^2$ is a universal function of the crack-tip speed that is very accurately approximated by $g(\hat{v}) \approx 1 - \hat{v}/c_R$ for $0 \leq \hat{v} \leq c_R$. Equation (2.61) implies that $K_I(t, a, 0) = 0$ at $t = 0$. As $K_I(t, a, 0)$ increases for $t > 0$, the right-hand side of (2.63b) approaches unity from its initial, unbounded value. The crack remains stationary when the left-hand side of (2.63a) is less than Γ_0 , and crack growth initiates at a critical time, denoted by τ' , when

$$\frac{1-\nu}{2\mu} [K_I(\tau', a, 0)]^2 = \Gamma_0, \quad (2.64)$$

since $g(\hat{v}) = 1$ for a stationary crack.

Crack-tip dynamics for step-function loading

Combining $\bar{s}(t) = H(t)\bar{\sigma}$ and (2.61) and recalling that $H'(t) = \delta_0(t)$ we obtain

$$K_I(t, a, 0) = C_I \sqrt{2\pi c_d t} \bar{\sigma}, \quad (2.65)$$

and the equation of crack-tip motion reduces to

$$g(\hat{v}) = \frac{\mu\Gamma_0}{(1-\nu)\pi c_d (C_I \bar{\sigma})^2 t}. \quad (2.66)$$

The right-hand side equals unity when

$$\tau' = \frac{\pi\mu\tilde{\phi}c_d}{4(c_s\bar{\sigma})^2}, \quad (2.67)$$

in which we have substituted $\tilde{\phi}$ for Γ_0 , as justified by the discussion below (2.62). Noting that $g(\hat{v}) \approx 1 - \dot{a}/c_R$, we obtain

$$\dot{a}' = \begin{cases} 0 & : 0 < t' \leq 1 \\ 1 - \frac{1}{t'} & : 1 < t' \end{cases} \quad (2.68a)$$

$$a' = \begin{cases} 0 & : 0 < t' \leq 1 \\ t' - 1 - \ln t' & : 1 < t' \end{cases} \quad (2.68b)$$

in which $\dot{a}' := \dot{a}/c_R$, $a' := a/\tau'c_R$ and $t' := t/\tau'$ are normalized, non-dimensional values for the crack-tip speed, crack-tip position and time. We observe that \dot{a}' approaches c_R asymptotically as $t' \rightarrow \infty$ and that $\tau' \propto 1/(\bar{\sigma})^2$. Thus, the time scale associated with the delay between the arrival of the longitudinal waves at the crack surface and the initiation of crack propagation shrinks as $\bar{\sigma}$ increases.

2.5.2 Numerical model for CFM theory

We use the spacetime discontinuous Galerkin (SDG) method described in [12, 23, 13] to implement the CFM model. Although the details of the SDG finite element method are not our primary concern in this work, we note that the method's element-wise balance properties, linear scaling properties, unique spacetime adaptive meshing capabilities, and use of two adaptive error indicators, one for the governing equations in the bulk material and one for the TSR on the cohesive interface, combine to provide exceptionally high precision in the numerical results reported here.

Domain description and material model

We consider a crack that propagates along the x_2 -axis, as shown in figure 2.5. The entire crack path, $\{(x_1, x_2) : x_1 = 0, x_2 > 0\}$, is modeled with the Xu and Needleman TSR described in 2.5.2. The nominal crack-tip position, defined according to the conventions introduced in 2.4.2, moves in the positive x_2 direction. Our goal is to investigate the influence of the nondimensional parameter σ' on the crack-tip motion.

We use a material model that approximates the elastic properties of polymethyl methacrylate (PMMA): Young's modulus, $E = 3.24$ GPa; Poisson's

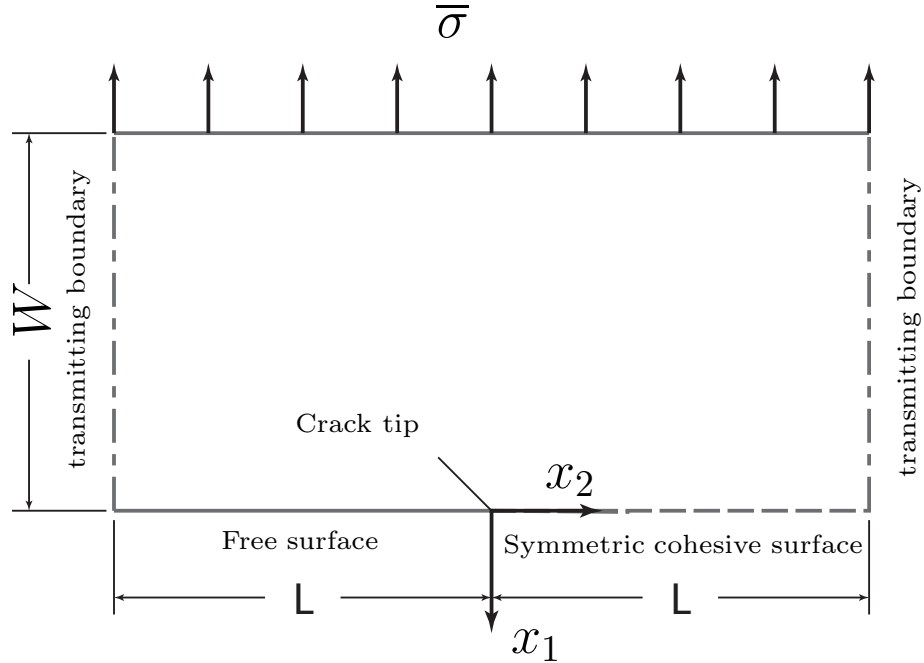


Figure 2.5: Cohesive model for middle-crack tension specimen.

ratio, $\nu = 0.35$; and mass density, $\rho = 1190 \text{ kg/m}^3$. For these values of the material parameters, the dilatational, shear and Rayleigh wave speeds are $c_d = 2090 \text{ m/s}$, $c_s = 1004 \text{ m/s}$, and $c_R = 938 \text{ m/s}$.

The cohesive properties for the traction–separation relation are based on those used in [14]; we use $\tilde{\sigma} = 0.1E = 324 \text{ MPa}$ and $\tilde{\delta} = 4.0 \times 10^{-4} \text{ mm}$ for the TSR relations described in (2.18) and in 2.5.2. We present our results in terms of nondimensional variables, so alternative choices for the cohesive and material parameters, other than the Poisson’s ratio, would not change the results.

Traction–separation relation

We restrict our attention to two spatial dimensions ($d = 2$) and to the history-independent, exponential TSR developed by Xu and Needleman [14]. As in [13, 14], we consider the simplified case where the critical separations and the works of separation are equal for the normal and tangential directions. That is, $\tilde{\delta}_{(1)} = \tilde{\delta}_{(2)} := \tilde{\delta}$ and $\tilde{\phi}_{(1)} = \tilde{\phi}_{(2)} := \tilde{\phi}$. The function \mathbf{f} in (2.18) then

takes the form, *cf.* [13],

$$\mathbf{f} \begin{pmatrix} \llbracket u_1 \rrbracket \\ \llbracket u_2 \rrbracket \end{pmatrix} = \begin{pmatrix} \Delta_1 \exp(1 - \Delta_1 - \Delta_2^2) \\ 2\Delta_2(1 + \Delta_1) \exp(1 - \Delta_1 - \Delta_2^2) \end{pmatrix}, \quad (2.69)$$

in which $\Delta_1 := \llbracket u_1 \rrbracket / \tilde{\delta}$ and $\Delta_2 := \llbracket u_2 \rrbracket / \tilde{\delta}$ are, respectively, normalized separations in the normal and tangential directions. In this particular case, the normal cohesive strength, $\tilde{\sigma}$, is achieved for $\llbracket u_1 \rrbracket = \tilde{\delta}$. That is $\tilde{\sigma}$ and $\tilde{\delta}$ in (2.18) are the cohesive strength and the critical separation for the normal direction. Finally, the work of separation is

$$\tilde{\phi} = e\tilde{\sigma}\tilde{\delta}, \quad (2.70)$$

in which $e \approx 2.718$ is the natural log base.

Regularized loading model

We apply a regularized tensile stress history along the top edge of the plate to approximate the step-function loading described in 2.5.1. The regularization is introduced only to reduce computational expense, and is given by

$$\check{H}(t) = \begin{cases} -2(t')^3 + 3(t')^2 & : t \leq \tau', \\ 1 & : \text{otherwise.} \end{cases} \quad (2.71)$$

The compressive traction loading for the second subproblem is then given by $\bar{s}(t) = 2\check{H}(t)\bar{s}_\infty = \check{H}(t)\bar{\sigma}$. Likewise, the ratio is $\check{\sigma}(t)/\tilde{\sigma} = \check{H}(t)\sigma'$ compared to $H(t)\sigma'$ in (2.59) for step function loading. The response to the regularized loading is very similar to (2.68). However, because of the regularization, the trajectory of the crack tip for the regularized LEFM solution is computed numerically, based on (2.61) and (2.63).

We use (2.68) to estimate, based on LEFM theory, the minimum space-time domain required to ensure that there is sufficient space and time for the crack tip to approach the Rayleigh wave speed without encountering reflected waves or edge effects from the domain boundary. The time required to reach $\dot{a}' = 1 - 10^{-\alpha}$, $\alpha > 0$ is $T(\alpha) = 10^\alpha \tau'$, at which time the length of crack extension must be less than $L(\alpha) := 10^\alpha \tau' c_R$. Given the ratio σ' , we compute τ' using (2.64) and choose $1 \leq \alpha \leq 2$. We set the duration of our

simulation and the spatial dimensions L, W in figure 2.5 to roughly double $T(\alpha)$ and $L(\alpha)$ to ensure that no reflected waves or edge effects influence the cohesive response.

2.5.3 Influence of load amplitude on cohesive response

Next, we study the influence of the normalized load intensity σ' on the cohesive response. The entire cohesive surface debonds simultaneously when σ' exceeds unity, so that the apparent ‘crack speed’ is infinite. This is the lifting-off mode of separation discussed in [14], not a mode of dynamic fracture, so we focus on problems where $\sigma' < 1$. We study a low-amplitude load range, where $\sigma' \ll 1$, as well as a high-amplitude range, in which $\sigma' \rightarrow 1^-$. For the low-amplitude case, we use load data in the range $-3/2 \leq \log \sigma' \leq -1/2$, with equal logarithmic increments, and for the high-amplitude case, we use $\log \sigma' = -1/4, -1/8, -1/16, \dots, -1/128$ so that the largest value of σ' is $10^{-1/128} \approx 0.98$. In all cases, we plot solution histories as functions of the normalized time, t' , to facilitate comparison with the LEFM reference solution; *cf.* (2.37a).

The validity of the SSY assumption is an effective predictor of the accuracy of the LEFM theory. As a first approximation, we evaluate (2.57) with $\tilde{\phi} = G$ and $\zeta = 9/16$ (*cf.* 2.5.3). Since $\check{\sigma}/\check{\sigma} = \sigma' \check{H}(t)$, we obtain a maximum estimate for the normalized CPZ size, $\Lambda/r \approx 0.55$, which indicates that the SSY assumption is valid for most, but not all, of the low-amplitude-load range. In the high-amplitude range, the LEFM estimate yields $1.76 \leq \Lambda/r \leq 5.36$. Since the numerical results for the CFM model predict even larger CPZ sizes, the SSY assumption is clearly invalid in the high-amplitude-load range.

Crack-tip trajectory and velocity

Figure 2.6 shows histories of the crack-tip velocity and position for the low-amplitude loads plotted against non-dimensional time. The velocity histories for different values of σ' in the cohesive model are nearly identical, except at the onset of propagation. The reference LEFM solution exhibits visible differences with respect to the cohesive solutions at velocities larger than

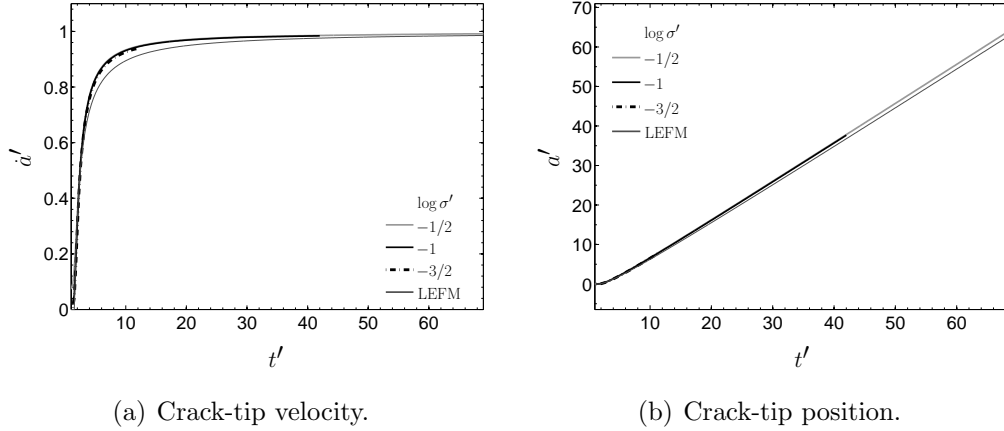


Figure 2.6: Crack-tip velocity histories and trajectories for low-amplitude loads, $\bar{s}_\infty \ll \tilde{\sigma}$.

$0.6c_R$. However, these differences decrease as the crack-tip velocities approach their limiting value, c_R . Corresponding differences are observed in the crack-tip trajectories depicted in figure 2.6(b). The trajectories are nearly identical across the cohesive model simulations. The relatively large difference in the cohesive and LEFM crack velocities for $\dot{a} \approx 0.9c_R$ manifests itself in larger crack extensions in the CFM results.

Let t_0 and v_0 denote, respectively, the time and velocity at the onset of crack propagation. Figure 2.7 shows the crack speed and position during the early stages of crack growth. The initiation time for the LEFM solution is $t_0 \approx 1.5\tau'$. The load regularization described in (2.71) causes a delay of about $\tau'/2$ delay relative to the solution in (2.68). Although the initial crack velocity in the LEFM solution vanishes, we observe that v_0 increases and τ' decreases as we raise σ' in the CFM simulations. In fact, $t_0 \approx \tau'$ for $\sigma' = 10^{-1/2}$, which corresponds to the time at which the sustained value of the applied load is attained in (2.71). The sensitivity to the load-amplitude parameter increases nonlinearly, in part, because $\Lambda/r \propto (\sigma')^2$.

The crack-tip trajectories from the CFM simulations are very close to those from the LEFM solution at early times in figure 2.7(b). However, they start to deviate at later times due to the cumulative effect of the larger velocities in the CFM solutions. The difference grows as we increase σ' .

Figure 2.8 displays the response to high-amplitude loads. Crack propagation initiates almost immediately when the applied loading reaches its

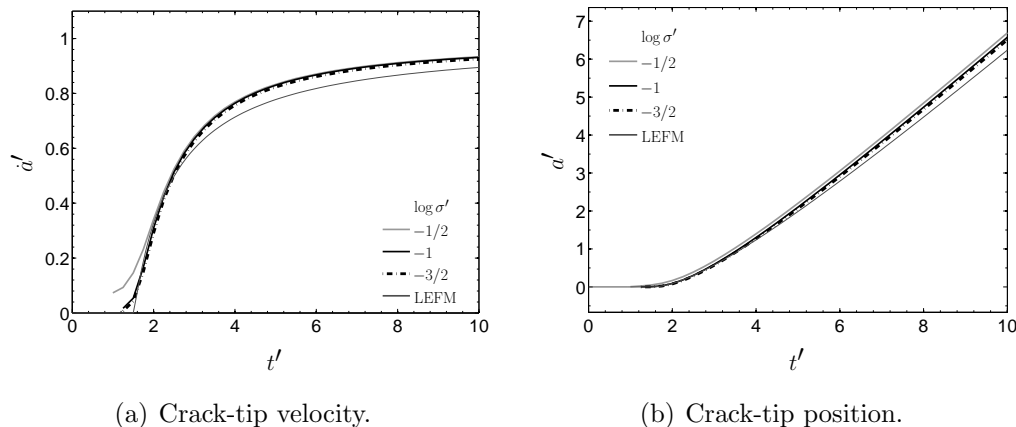


Figure 2.7: Early stages of crack-tip velocity histories and trajectories for low-amplitude loads, $\bar{s}_\infty \ll \tilde{\sigma}$.

sustained value at time τ' in all of the CFM solutions. This contrasts with the LEFM theory, which, in general, predicts a delay of crack initiation by about $0.5\tau'$. For low-amplitude loads, the delay time is the time required for to develop the crack-tip singular fields. However, for the high-amplitude loading considered here, where $\sigma' \approx 1$, the crack propagates almost immediately when the crack-surface loads reach their sustained value, even though the singular LEFM fields are not yet fully developed.

The initial velocity v_0 increases rapidly as $\sigma' \rightarrow 1^-$, and there are irregular ‘humps’ in the CFM results at early times. Eventually, the CFM results for varying load amplitudes converge as the crack speeds approach c_R . Numerical studies using variable ramp times in the load regularization (2.71), indicate that the hump feature is a numerical artifact that becomes sharper and more prominent as the ramp time increases. Recalling that the regularization is simply a means to reduce computational expense, *cf.* 2.5.2, we expect the hump feature to become less pronounced and v_0 to increase as the regularization ramp time approaches zero. Apart from this numerical artifact, we observe a general increase in v_0 and a greater discrepancy relative to the LEFM solution as $\sigma' \rightarrow 1^-$ in the CFM model.

Figure 2.8(b) shows the crack-tip trajectories for high-amplitude loading. Evidently, increasing σ' increases crack extension, as is expected for the larger crack-tip speeds. The LEFM crack extensions are smaller at any given time, due to the delayed initiation of crack growth and to the more gradual tip

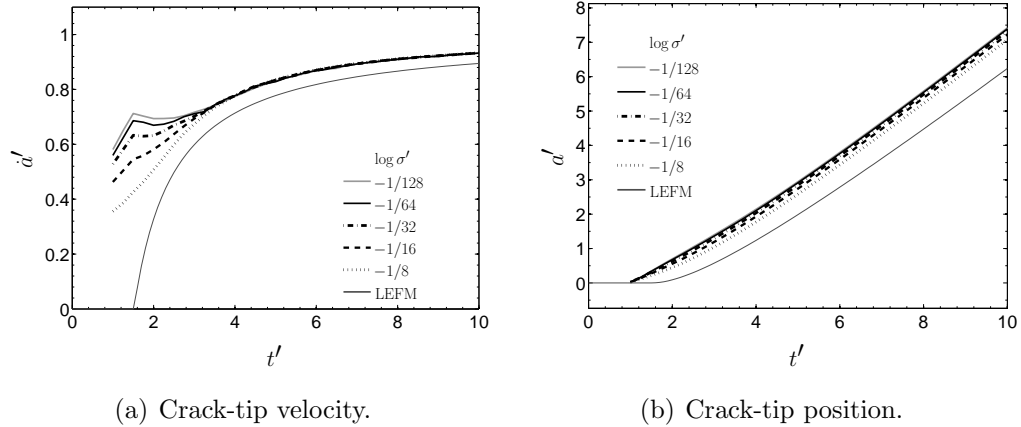


Figure 2.8: Crack-tip velocity histories and trajectories for high-amplitude loads, $\sigma' \rightarrow 1^-$.

acceleration in the LEFM solution.

Energy release rate

Here we investigate the influence of load amplitude on the the evolution of the energy release rate, G . As noted in section 2.5.1, $G = \tilde{\phi}$ under steady-state conditions. Based on the discussion in section 2.4.3 and on (2.55) and (2.56), we concluded that transient effects become less important as the crack speed approaches c_R . However, this conclusion depends on the validity of the small-scale-yielding assumption, a caveat in the derivation of (2.55), which, in turn, depends on the amplitude of the loading.

Figure 2.9 shows the evolution of the energy release rate G as a function of load amplitude, for both the low- and high-amplitude ranges. In all cases, highly transient behavior is observed at the early stages of the evolution. At very early times, there is a brief stage where G exceeds the work of separation by a significant margin. This effect, which is more pronounced in the high-amplitude load range, can be attributed to diffuse separation due to the uniform tensile stress acting over the entire cohesive surface. This is followed by a brief excursion of G into the negative range. This is due to a rebound effect associated with the sudden load application, and numerical studies, not presented here, show that his effect reduces and eventually vanishes with increased ramp time in the load regularization. For loads in the low-amplitude range, G quickly returns to and undergoes small oscillations

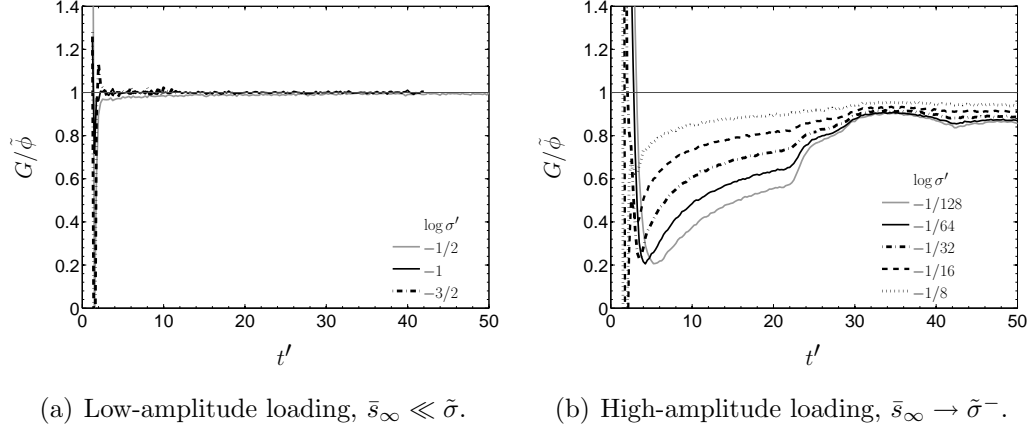
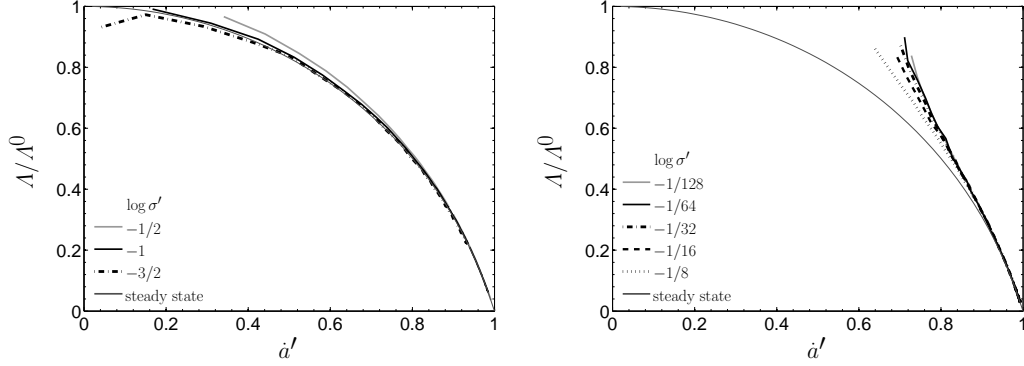


Figure 2.9: Evolution of energy release rate as a function of load amplitude.

about the work of separation, $\tilde{\phi}$. For high-amplitude loads, the behavior is similar, but G oscillates about a value below $\tilde{\phi}$. This lower value is due to the fact that the initial energy release from diffuse separation is much larger for loads in the high-amplitude range. The much longer recovery time in Figure 2.9(b) can be attributed to violations of the SSY assumption in the high-amplitude load range.

Figure 2.9(a) depicts the changes of G normalized by $\tilde{\phi}$ versus normalized time. We observe that $G \approx \tilde{\phi}$ for $t \geq 2\tau' - 4\tau'$. This corresponds to crack speeds $\dot{a} > 0.4 - 0.8c_R$ in figure 2.7(a). The highly unsteady crack growth and specially small crack velocity are the causes of discrepancy for smaller times. The impinging shock front at early time releases energy on the entire cohesive surface which results in large value for G . The short temporary decrease of G to negative values is a consequence of sharp regularization which causes a short interval of crack closing at early stages.

Figure 2.9(b) demonstrates the changes in G when $\sigma' \approx 1_-$. The impinging planar wave causes a uniform separation along the entire cohesive surface. As $\sigma' \rightarrow 1_-$ the uniform separation increases to $\tilde{\delta}$ which corresponds to $\tilde{\sigma}$ in Xu and Needleman TSR. This initial separation “consumes” a part of the work of separation and only the remaining fraction can be released under the actual crack propagation. The fact that the steady values for G at $t \geq 40\tau'$ decrease by an increase in σ' is a consequence of this uniform release of energy for intrinsic cohesive models. The same concept applies in figure 2.10(a), however, the fraction of the energy released due to uniform loading



(a) Low-amplitude loading, $\bar{s}_\infty \ll \tilde{\sigma}$.

(b) High-amplitude loading, $\bar{s}_\infty \rightarrow \tilde{\sigma}^-$.

Figure 2.10: Evolution of cohesive process zone size for unsteady crack growth.

is negligible.

Similar to figure 2.7(a), we observe that G decreases from values considerably larger than $\tilde{\phi}$ and after a short interval of negative value it raises to reach its steady state value. However, we have a rather prolonged interval before reaching the steady value. The main reason for this substantial difference between figures 2.7(a) and 2.8(a) is the validity of small-scale yielding condition assumed in (2.55).

Cohesive process zone size

In this section we want to examine equation (2.53). Figure 2.10 compares the actual Λ/Λ^0 where $\zeta = 9/16$ is used in the estimate (2.52). As mentioned in section 2.4.2 this value is suggested for potential-based cohesive models. The choice of this factor would only scale Λ/Λ^0 for all crack speeds. Coincidentally with the definition of cohesive process zone in section 2.4.2, the value $\zeta = 9/16$ provides a very good estimate as it is evident in this figure.

There is a very good agreement between numerical results and the estimate (2.53) in figure 2.10(a), specially after the initial rapid crack acceleration. As explained in section 2.4.2, the change in \hat{v}/c_R for a crack advance equal to Λ can be an indicator on steadiness of the propagation. At early stages of crack propagation, crack velocity is small, hence the process zone size must be large based on (2.54). At the same time, the crack acceleration is relatively high as shown in 2.7(a). The small discrepancy at early crack

speeds on each of the data sets is a result of these effects combined. We, however, observe a very small error over the whole range of velocities.

Figure 2.10(b) shows the results when $\sigma' \approx 1_-$. The initiation crack speed, v_0 , is noticeably higher than zero as illustrated in figure 2.8(a). For the same reasons in previous case, the error from steady state estimate is larger at early stages of crack propagation. However, herein, the difference is considerably higher; the relative process zone size increases as $\sigma' \rightarrow 1_-$. Although the initiation crack speeds are higher in this case, the violation of SSY contribute to larger discrepancies compared to figure 2.10(a). As mentioned before, equation (2.57) yields the range of 1.76-5.36 for Λ/r under the assumption of $\zeta = 9/16$ and $\tilde{\phi} = G$. We obtain even higher values for Λ/r since Λ takes larger values than the estimate (2.53) which was assumed in the derivation of (2.57). Finally, we notice that as $\dot{a} \rightarrow c_R$ all CFM results merge to the steady state estimate. This is expected since $\Lambda \rightarrow 0$ as $\dot{a} \rightarrow c_R$ and the crack motion can be accurately approximated as steady state.

2.6 Conclusions

We carry out a dimensional analysis for a general initial and boundary value elastodynamic problem using differential forms notation. We consider scalings of both the forms overall and of just the form coefficients, as would be done in analyses using conventional tensor notation. We show that to obtain a scaled elastodynamic process, the velocity scalings implied by the spatial and temporal coordinate scalings and by the scalings of the material properties must be identical. Our analysis within the differential forms notation reveals certain intrinsic relations between the spacetime mechanics fields, which otherwise are obscured by tensorial notation. For example we find that only four distinct scalings are required to define an elastodynamic process when we work directly with forms, while eight are required when tensor notation is used. This simplification provides new evidence of the elegance and insight afforded by spacetime mechanics formulations that use differential forms and the exterior calculus.

Furthermore, we extend the dimensional analysis to TSR-based cohesive fracture mechanics problem. We demonstrate that the stress and displacement fields are related to cohesive strength and separation. The solution

fields are represented in terms of nondimensional groups which in turn are expressed in terms of cohesive scales. The cohesive length scale, \tilde{L} , determines the scaling of domain dimensions. We also show that cohesive process zone size is proportional to \tilde{L} . The intrinsic cohesive velocity value, \tilde{v} scales all velocity related fields. In addition we obtain an intrinsic time scale, $\tilde{\tau}$, which is of fundamental importance in dynamic fracture. For example, Pandolfi *et al.* [11] discussed the influence of the characteristic time on crack initiation and propagation. It also influences minimum time step required for a convergent time stepping algorithm.

We can identify a TSR cohesive model by characteristic strength, $\tilde{\sigma}$, separation, $\tilde{\delta}$, and work of separation, $\tilde{\phi}$. We discussed the relation between self-similar solutions by modifying these characteristic values. This study is of importance, for example, to study the changes in the response of the system when one of the characteristic values is changed. Furthermore, we derive all the nondimensional parameters associated with cohesive fracture mechanics. The first group relate the magnitude of applied loads, *e.g.*, initial and boundary conditions as well as body force, to cohesive strength. The second group compare the spatial and temporal scales of the domain with their corresponding cohesive values, namely \tilde{L} and $\tilde{\tau}$.

The stress and velocity fields from LEFM theory are singular around the crack tip. Obviously, real materials could not withstand such values and stresses are reduced through plastic or some other material yielding processes in a zone around the singular core. The LEFM solutions can, however, accurately describe the response outside the process zone if SSY assumption holds. That is, the relative size of this process zone to radii of singularity from LEFM theory is considerably smaller than unity. We show that this ratio, A/r , is proportional to $(\check{\sigma}/\tilde{\sigma})^2$ where $\check{\sigma}$ in turn is proportional to the scale of loading. This relation is of utmost importance. On one hand, it quantifies small-scale yielding assumption and determines how LEFM solution loses its accuracy. On the other hand, $\check{\sigma}/\tilde{\sigma}$ is one of the nondimensional parameters associated with TSR models; as mentioned above, changes to these parameters can not be described by self-similar solutions.

We studied the effect of σ' on cohesive fracture for a mode *I* crack in an infinite domain and compared the solution with an LEFM reference solution. We showed that crack initiation time decreased while its corresponding velocity increased relative to LEFM solution by increasing σ' . The difference in

crack speeds for different ratios σ' becomes negligible as they approach the Rayleigh wave speed. We also examined the evolution of CPZ and compared that with steady state estimates. There were discrepancies between CFM results and the estimate at initial propagation stages or when SSY assumption failed. However, the transient results very closely matched the estimate when crack velocity approached the Rayleigh wave speed.

The numerical results were obtained by the Spacetime Discontinuous Galerkin Finite Element method [12, 13]. The element-level balance of momentum, dual adaptive control of dissipation and fracture energy error, and linear complexity of the numerical scheme enabled us to very accurately solve the trajectory and velocity of moving cracks. For example, Xu and Needleman [14] reported numerical crack velocities that exceeded the Rayleigh speed for high ratios of σ' . We did not encounter this problem and even for σ' as high as $10^{-1/128}$ the crack speeds were bounded by the Rayleigh wave speed.

In this work, we only investigated the nondimensional parameters relating the ratio of the loads to cohesive strength. In finite domains the interplay between the domain and cohesive length and time scales changes the dynamic of moving cracks. For example, waves reflected from the domain boundaries and crack tips can appreciably change the crack speed. The study of such nondimensional parameters can be an extension to the current work. Moreover, similar studies can be carried out for other types of fracture models such as the interfacial damage evolution models described in the following chapters. Finally, it is desirable to extend the results on pure modes *I* and *II* to a general mixed mode condition. Our numerical results were obtained using Xu and Needleman (*cf.* section 2.5.2) TSR. We do not advocate any specific form of the cohesive model in this work and the theoretical development is independent of such choice. Under the mixed mode conditions many of the existing cohesive models exhibit non-physical behavior. For further discussion of such features and a new cohesive model addressing these issues the reader is referred to [24].

Chapter 3

Riemann conditions for elastodynamic contact with SDG implementation

3.1 Introduction

Contact and friction play a central role in the modern life. Contact is the principal method of applying loads to a deformable body [25] and about a third of the world’s energy resources appear as friction in one form or another [26,27]. The strong nonlinear and non-smooth transitions associated with contact/separation and stick/slip modes pose numerous difficulties in the study of contact mechanics.

A variety of numerical methods for modeling contact and friction have been proposed. The *penalty* methods [28,29,30,31,32] enforce contact conditions through the application of large “penalties” when contact inequalities are violated. For example the kinematic compatibility condition is modeled by employing high stiffness values for negative separations. The solution to these problems is approximate and approaches the exact solution as the penalty variables become increasingly large. However, the use of excessively high values may result in stiff global stiffness matrices, which in turn leads to numerical errors and divergence. Moreover, the stiff system requires smaller time increments, which may introduce undesirable large numerical oscillations [33]. The *adaptive penalty* methods in [34,35,36] alleviate these problems, to some extent, by adjusting the penalty values in concert with the numerical stability and accuracy, bisecting the load or time step size when the increment is excessive, and updating the stiffness at appropriate times.

Variational Inequalities(VIs) and *Lagrange multiplier* methods [37,38,39,40,41,42,43], on the other hand, exactly enforce the contact/friction constraints. The major drawback of these methods is the increase of problem size due to the introduction of Lagrange multiplier variables. Moreover, they typically require an implicit solution scheme for the augmented system, which can become computationally very expensive for large problems [33].

The variational based contact mechanics formulations are discussed in more detail in [44].

A variety of other numerical methods for modeling contact mechanics have been proposed. For example, the penalty and Lagrange multiplier methods are combined in [45, 46]. The transition between separation and contact modes is realized through the introduction and elimination of independent normal degrees of freedom on the opposite sides of contact interface in the *United element method* [47]. In *Decomposition contact response* (DCR) method [33], a predictor corrector-type algorithm is employed to independently enforce the impenetrability constraints and the exchange of momenta between the impacting bodies. The monographs [48, 49, 50] specifically investigate the contact problem in the realm of computational mechanics.

The study of contact mechanics at fine scales and the derivation of macroscale properties has gained a considerable attention recently. Oden [51] derives several macroscale contact properties such as static coefficient of friction on the assumption that elastoplastic asperities are randomly distributed over the contact surface. Gerde and Marder [52] demonstrate that the existence of self-healing cracks at atomic scales result in solids that slip in accord with Coulomb's laws of friction. *Molecular dynamics*(MD) simulations have also been employed to derive the macroscale contact properties [53, 54] and investigate the static and kinetic frictions [55, 56]. However, the high cost of MD simulations limits their application to very small length and time scales, so they are not useful for many scientific and engineering studies. A more complete survey of contact mechanics can be found in [57, 58, 25, 59].

This chapter presents the Riemann conditions for the elastodynamic contact problem within an adaptive spacetime discontinuous Galerkin (SDG) finite element method [60, 12, 13]. We use the differential form notation on spacetime manifold. The expression of mechanical fields in differential forms reveals several intrinsic relations between space and time fields that are otherwise obscure in classical mechanics. Upon the application of the Stokes theorem on the balance of momentum and taking the jump part of the kinematic compatibilities, we derive the appropriate jump conditions across manifolds with arbitrary orientations in space and time. The expression of Stokes theorem and the resulting jump conditions are, however, problematic in tensorial notation due to the absence of an objective metric in spacetime settings.

We employ the derived jump conditions to enforce the appropriate target

values across the element boundaries. The physically and mathematically correct target fluxes are obtained from the solution to a Riemann problem. A detailed description of Riemann solutions can be found in [61,62]. Herein, we present a novel method to solve the Riemann problem for linear elastodynamics. We directly derive the admissible jump manifolds and their jump conditions by the application of the jump parts of the balance of momentum and the kinematic compatibility conditions. Our method is more direct and physically-motivated than the conventional Riemann solutions [61], where the eigensolutions to the entire spatial flux matrix is required.

The aforementioned solution process provides the allowable set of Riemann target fluxes on an arbitrary material interface. These solutions can subsequently be employed in specific matching conditions which arise for different classes of interface conditions. Specifically, we derive the Riemann solutions for bonded, contact–stick, contact–slip, and separation modes, which to our knowledge have not been reported before.

We demonstrate that the solution for bonded and contact–stick modes are identical. That is, the interface should be modeled as bonded when it is in stick mode. This identification is not realized in many numerical methods. For example, large stiffness values replace the interelement continuity condition for the bonded mode in penalty methods. Furthermore, the enforcement of kinematic compatibilities ensures the satisfaction of impenetration condition. In contrary to Lagrange multiplier methods, no additional degrees of freedom are augmented to the problem.

The interface undergoes the contact–slip mode when the contact–stick Riemann solution violates the Coulomb’s stick condition. The tangential target traction is derived from the Coulomb’s friction law; the magnitude of the tractions is k times the compressive traction and its direction is the same as the sliding velocity of the two sides of the interface, $[[\mathbf{v}]]$ when $[[\mathbf{v}]] \neq 0$, otherwise it is aligned with the tangential traction that would have acted under the stick mode¹. Different types of numerical regularization have been reported in response to the abrupt stick/slip mode changes in Coulomb’s friction law. Peillix *et al.* [63] introduced a relaxation time which delays the friction response to the changes in the compressive traction and the regularization of the contact surface is addressed in [64].

¹Refer to (2.2) for the definition of the jump operator and section 3.2.1 for detailed explanation of the Coulomb’s friction law.

This Coulomb relation is discontinuous at $[[\mathbf{v}]] = 0$ as shown in section 3.2.1 and [65]; the frictional traction exhibits potentially large oscillations, since the orientation of $[[\mathbf{v}]]$ can change when $[[\mathbf{v}]] \rightarrow 0$. The computational difficulties posed by the direct determination of the orientation of frictional traction from that of $[[\mathbf{v}]]$ are well documented and necessitate special treatments as $[[\mathbf{v}]] \rightarrow 0$; Karnopp [66] proposes the elimination of slip mode kinematic degrees of freedom, if the contact velocity magnitude falls below a specified threshold. The regularization of the Coulomb friction law is sought as an alternative remedy in [67, 65]. Herein, we demonstrate that $[[\mathbf{v}]]$ and contact–stick tangential traction are aligned for linear homogeneous material. That is, we can directly compute the direction of slip mode traction from that of stick mode. As will be explained in section 3.2.1, this eliminates numerical difficulties encountered when $[[\mathbf{v}]] \rightarrow 0$.

Mathematically speaking, any given point on a contact surface can only take one of the stick, slip, or separation modes; the interface is in contact mode if the separation is zero and the normal traction is compressive, otherwise it is in separation mode. The satisfaction of the Coulomb inequality will distinguish between the stick and slip modes. The sharp transition between contact and separation modes may produce stress and velocity discontinuities on the contact interface as well as in the bulk material [40]. Such discontinuities may pose convergence problems if they pass through the boundaries of finite elements. We will present a regularization of the transition between the contact modes in order to eliminate such nonconvergence problems as well as a means to reduce the computational cost.

Our SDG method is implemented on fully unstructured spacetime meshes with basis functions that are discontinuous across all spacetime element boundaries. When implemented on suitable spacetime grids that satisfy a special *causality constraint* [68], the SDG formulation supports an efficient patch-by-patch², advancing-front solution scheme with $O(N)$ computational complexity, where N is the number of elements in the spacetime mesh. The patch-wise solution method also facilitates adaptive spacetime meshing algorithms wherein mesh refinement and coarsening operations are implemented locally on individual elements or patches [69]. The employment of Riemann solutions, per-element balance of momentum [60, 12], and local adaptivity

²A patch is a small collection of contiguous finite elements, *cf.* section 3.3.2.

operations, makes our SDG method a very accurate and efficient method for solving the contact problems.

3.2 Formulation

In this section, we derive the Riemann solutions for separation and contact modes. Following the development in [12, 13], we use the differential form notation on spacetime manifolds. This approach provides a direct, coordinate-free notation that can be used to express fluxes across spacetime interfaces with arbitrary orientation. This leads to concise representations of the governing equations that emphasize the notion of conservation on spacetime control volumes.

Differential forms are not widely used in solid mechanics; however, their use is well justified in the spacetime setting. For example, the spacetime Stokes Theorem has a simple and elegant structure when written for differential forms, but its expression for spacetime tensor fields is problematic due to the ambiguity in the definition of spacetime normal vectors; the absence of an objective metric in classical mechanics prevents to define magnitude and the orthogonality property for spacetime vectors.

The exterior derivative operator generally includes a diffusive and a jump part. In contrast to the jump part, the diffusive part acts where the differential form is smooth. In fact, the *Rankine-Hugoniot* conditions are systematically derived from the aforementioned jump parts. Similar to Stokes theorem, we need the notion of unit normal vectors on spacetime manifolds to express such jump conditions in tensorial notation. This, however, does not pose a problem in differential form context where such unit normal vectors are not referenced.

We present a novel method to solve the Riemann problem for linear elastodynamics. We directly derive the admissible jump manifolds and their jump conditions by the application of the jump parts of the balance of momentum and compatibility conditions. These conditions are otherwise obtained through the solution to the eigenvalues and eigenvectors of matrices which correspond to spatial flux vectors. Our method, not only is more direct and eliminates the eigensolution to these matrices, but also provides more physical insight to the jump condition and the whole solution process. We

employ this method to compute the physically and mathematically correct target values for separation and contact modes. Furthermore, we incorporate these solutions in our discrete *spacetime discontinuous Galerkin (SDG)* finite element method.

The expression of the mechanical fields and governing equation in differential form notation follows the development in 2.2. We start the section with the strong form of the problem which is required for the formulation of the weak form in 3.3.1. In addition, the determination of the target fluxes in 3.2 is slightly different from the previous chapter.

Continuum problem statement

Our SDG finite element method derives from a continuum problem in which the displacement field \mathbf{u} is the only independent unknown solution field. That is, compatibility relations (2.8a) and (2.5a) are strongly enforced. Miller *et al.* [18] demonstrate that under such conditions (2.6) reduces to,

$$[(\mathbf{u}_0^* - \mathbf{u}_0) \star dt]|_{\partial Q} = \mathbf{0}, \quad \forall Q \subset \mathcal{D} \quad (3.1)$$

a subscript “0” indicates a local projection to a zero-energy subspace characterized by vanishing velocity and strain [12, 18]. Furthermore, we strongly enforce the constitutive relation (2.10). Then we seek $\mathbf{u} \in \mathcal{V}$ such that (2.12a) as well as the jump conditions for kinematic compatibility (2.9), (3.1) and the equation of motion (2.13) are satisfied. The computation of target values is given in the following section.

Target values

Consider a subdomain $Q \subset D$. The target values \mathbf{u}_0^* , $\boldsymbol{\varepsilon}^*$, and \mathbf{M}^* in (2.9), (3.1), and (2.13) provide a unified mechanism for enforcing boundary conditions consistent with prescribed boundary and initial data on $\partial Q \cap \partial \mathcal{D}$ or with causality on $\partial Q \setminus \partial \mathcal{D}$. We introduce two partitions that determine how the target value is computed on different parts of ∂Q .

The *temporal partition of ∂Q* helps determine the target value \mathbf{u}_0^* on ∂Q (see Figure 3.1(a)). The characteristic associated with this partition is in the \mathbf{e}_t direction. The *temporal inflow boundary of Q* , is defined as ∂Q^{ti} where \mathbf{e}_t is inflow relative to ∂Q . The *temporal outflow boundary* is $\partial Q^{\text{to}} =$

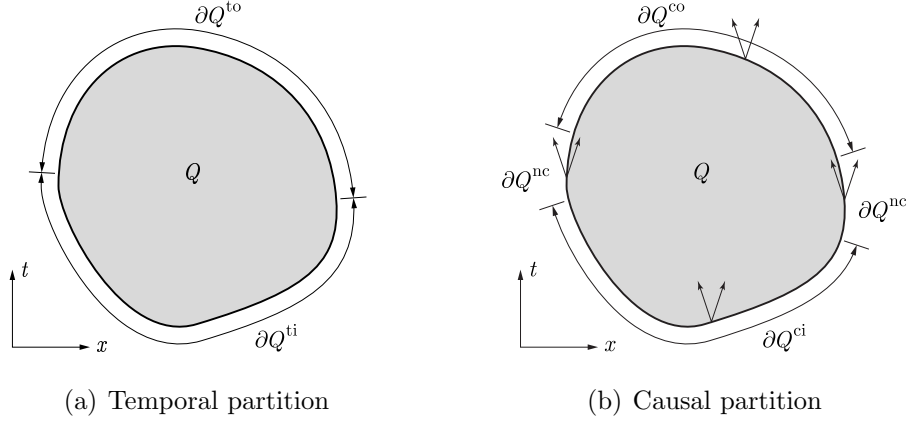


Figure 3.1: Alternative partitions of ∂Q .

$\partial Q \setminus \partial Q^{ti}$. The upstream value determines the target value. That is, the initial conditions or the trace from adjacent spacetime domains, determine \mathbf{u}_0^* on ∂Q^{ti} , while \mathbf{u}_0^* is equal to the interior trace of \mathbf{u}_0 on ∂Q^{to} , so that (3.1) is trivially satisfied).

We use a separate *causal partition* of ∂Q to determine the target values for $\boldsymbol{\varepsilon}^*$ and \mathbf{M}^* . A d -manifold is *causal* if its intersection with the union of the dynamic domains of influence of all its points is empty. As a result, all characteristic directions at all points on a causal subdomain of ∂Q are either all outward or all inward relative to Q . We partition ∂Q into its causal and noncausal parts, ∂Q^c and ∂Q^{nc} . Furthermore, ∂Q^c is partitioned into a *causal inflow* part ∂Q^{ci} and a *causal outflow* part ∂Q^{co} as depicted in figure 3.1(b). The characteristic directions are all inward relative to Q on ∂Q^{ci} , where the target values are obtained either from initial conditions or inflow traces from adjacent subdomains [12, 13]. The characteristics are all outflow on ∂Q^{co} , where the interior trace determines the target values so that the corresponding jump conditions are trivially satisfied.

The application of either Dirichlet or Neumann boundary conditions and initial conditions through \mathbf{M}^* and $\boldsymbol{\varepsilon}^*$ is described in [12, 13]. Here we direct our attention to $\partial Q \setminus \partial \mathcal{D}$, where the target values are determined by causality, as reflected in the characteristic structure of the governing hyperbolic system. Due to the crossing of characteristics on noncausal boundary segments, the target fluxes on ∂Q^{nc} depend on both the interior and exterior traces of \mathbf{M} and $\boldsymbol{\varepsilon}$ on ∂Q as well as on the local orientation of ∂Q .

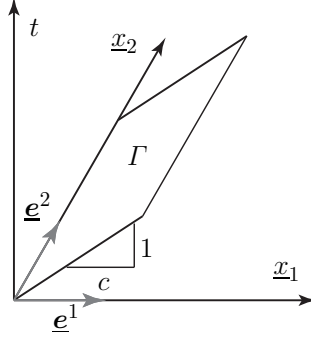


Figure 3.2: The local coordinate system at a jump manifold.

We define the *contact set* of \mathcal{D} , denoted by $\tilde{\Gamma}$, as the union of all vertical d -manifolds in $\partial\mathcal{D}$ that are either in active contact or are possibly in imminent contact. In general, the identification of $\tilde{\Gamma}$ is an important aspect of a contact solution algorithm. However, for simplicity, we assume in this work that $\tilde{\Gamma}$ is known *a priori*. By including in $\tilde{\Gamma}$ boundary segments that are only in imminent contact, we must include *separation* as one of the possible contact modes, in addition to *contact-stick* and *contact-slip*. We describe below a method that determines the contact mode at any given point on $\tilde{\Gamma}$

3.2.1 Riemann solutions with specialization to the contact conditions

In this subsection, we develop Riemann solutions on material interfaces and specialize them to the contact interface conditions, separation, contact-stick and contact-slip. First, we show that the longitudinal and shear wave speeds identify the admissible orientations for d -manifolds that can sustain non-trivial jumps in the mechanical fields. Next, we develop a general solution and identify the associated characteristic values for a Riemann problem in which the field values on only one side of a vertical material interface control the solution. We use the general solution to solve a standard Riemann problem controlled by distinct states on opposing sides of the interface, and then specialize this result to the various contact conditions.

Admissible orientations of jump manifolds

Let Γ be a non-horizontal d -manifold embedded in $\mathbb{E}^d \times \mathbb{R}$, as illustrated in figure 3.2 for the case $d = 2$. To facilitate a description of the restricted cotangent space $T^*\Gamma$, we define on Γ a local frame, $\{\underline{\mathbf{e}}^i, \mathbf{e}^t\}_{i=1}^d : \underline{\mathbf{e}}^1 \perp T^*\Gamma|_{\mathbb{E}^d}$, with local coordinates $\{\underline{x}_i, t\}_{i=1}^d$, in which underlined symbols denote items referred to the local frame. The standard basis for 1-forms in the local coordinate system is $\{d\underline{x}^1, \dots, d\underline{x}^d, dt\}$. The standard basis for d -forms, $\{\star d\underline{x}^1, \dots, \star d\underline{x}^d, \star dt\}$, and the combined forms, $\mathbf{d}\underline{\mathbf{x}} := \underline{\mathbf{e}}_i d\underline{x}^i$ and $\star \mathbf{d}\underline{\mathbf{x}} := \underline{\mathbf{e}}^i \star d\underline{x}^i$, are defined in the local coordinate system in the same fashion as their counterparts are defined in the global (\mathbf{x}, t) coordinate system; cf. section 2.2.1.

The velocity of the manifold in the \underline{x}_1 -direction, denoted by c , determines the orientation of Γ , as shown in the figure. Thus,

$$d\underline{x}^1|_{\Gamma} = c dt|_{\Gamma} \quad (3.2)$$

Since, $d\underline{x}^i \wedge \star d\underline{x}^j = \delta_j^i \boldsymbol{\Omega}$, $dt \wedge \star d\underline{x}^j = \mathbf{0}$, $dt \wedge \star dt = \boldsymbol{\Omega}$ and $d\underline{x}^i \wedge \star dt = \mathbf{0}$ (cf. section 2.2.1) we have,

$$\star d\underline{x}^j = (-1)^{j-1} d\underline{x}^1 \wedge \dots \wedge \widehat{d\underline{x}^j} \wedge \dots \wedge d\underline{x}^d \wedge dt, \quad (3.3a)$$

$$\star dt = (-1)^d d\underline{x}^1 \wedge \dots \wedge d\underline{x}^d. \quad (3.3b)$$

in which the decoration $\widehat{}$ indicates a term that is omitted in the exterior product. We combine (3.2), (3.3) and the identity, $(\boldsymbol{\alpha} \wedge \boldsymbol{\beta})|_{\Gamma} = \boldsymbol{\alpha}|_{\Gamma} \wedge \boldsymbol{\beta}|_{\Gamma}$, to obtain,

$$\star dt|_{\Gamma} = -c \star d\underline{x}^1|_{\Gamma} \quad (3.4a)$$

$$\star d\underline{x}^i|_{\Gamma} = 0 \text{ when } i \neq 1 \Rightarrow \star \mathbf{d}\underline{\mathbf{x}}|_{\Gamma} = \underline{\mathbf{e}}^1 \star d\underline{x}^1|_{\Gamma}, \quad (3.4b)$$

To investigate the jump condition for the momentum flux on Γ , we first note that (3.4b) yields,

$$\boldsymbol{\sigma}|_{\Gamma} = \boldsymbol{\sigma} \wedge \star \mathbf{d}\underline{\mathbf{x}}|_{\Gamma} = \boldsymbol{\sigma} \wedge (\underline{\mathbf{e}}^1 \star d\underline{x}^1|_{\Gamma}) = \boldsymbol{\sigma}(\underline{\mathbf{e}}^1) \star d\underline{x}^1|_{\Gamma} = \mathbf{s} \star d\underline{x}^1|_{\Gamma} \quad (3.5)$$

where $\mathbf{s} := \boldsymbol{\sigma}(\underline{\mathbf{e}}^1) = (\underline{\sigma}^{ij} \underline{\mathbf{e}}_i \otimes \underline{\mathbf{e}}_j)(\underline{\mathbf{e}}^1) = \underline{\sigma}^{ij} \underline{\mathbf{e}}_i \delta_j^1 = \underline{\sigma}^{i1} \underline{\mathbf{e}}_i$ is the traction field acting on Γ . Equations (2.4), (3.4), and (3.5) yield $\mathbf{M}|_{\Gamma} = -(\underline{\mathbf{s}} + \underline{\mathbf{c}}\mathbf{p}) \star d\underline{x}^1|_{\Gamma}$.

Hence the jump condition for momentum flux (2.12b) reduces to

$$\llbracket \mathbf{s} + c\mathbf{p} \rrbracket|_I = \mathbf{0}. \quad (3.6)$$

From here on, for the sake of brevity, we drop I from the jump operator.

Next, we consider the jump condition for compatibility of strain and velocity on I . The expanded form of (2.8b) on I is $-\mathbf{T} : \llbracket \mathbf{E} \rrbracket \star dt + \mathbf{T}(\llbracket \mathbf{v} \rrbracket) \wedge \star d\mathbf{x} = \mathbf{0}$ in which ‘ \cdot ’ denotes the dyadic tensor product. According to (3.4), this reduces on I to

$$\begin{aligned} (c\mathbf{T} : \llbracket \mathbf{E} \rrbracket + \mathbf{T}(\llbracket \mathbf{v} \rrbracket) \otimes \underline{\mathbf{e}}^1) \star d\mathbf{x}^1|_I &= \mathbf{0} \\ \Leftrightarrow c\underline{T}_{ij} \llbracket E_{ij} \rrbracket + \underline{T}_{1j} \llbracket v_j \rrbracket &= \mathbf{0}. \end{aligned} \quad (3.7)$$

Since \mathbf{T} is an arbitrary symmetric tensor, equation (3.7) implies,

$$c \llbracket E_{11} \rrbracket + \llbracket v_1 \rrbracket = 0, \quad (3.8a)$$

$$2c \llbracket E_{1j} \rrbracket + \llbracket v_j \rrbracket = 0, \quad j \neq 1 \quad (3.8b)$$

$$\llbracket E_{ij} \rrbracket = 0, \quad i, j \neq 1 \quad \text{and} \quad c \neq 0 \quad (3.8c)$$

Next, we develop necessary conditions for simultaneous satisfaction of (3.6), (3.8) and the constitutive relation (2.10). We first treat the case $d = 3$ and consider later specializations to lower spatial dimensions. We assume isotropic material, so the components of the elasticity tensor are expressed as,

$$C^{ijkl} = \lambda \delta^{ij} \delta^{kl} + \mu (\delta^{ik} \delta^{jl} + \delta^{il} \delta^{jk}), \quad (3.9)$$

where λ and μ are the Lamé parameters. Thus, we get $\sigma^{ij} = 2\mu \delta^{ik} \delta^{jl} E_{kl} + \lambda \delta^{ij} E_{kk}$. Substituting this result into (3.8), and considering (2.10), we obtain

$$\llbracket \underline{\sigma}^{11} \rrbracket = \llbracket \underline{s}^1 \rrbracket = (\lambda + 2\mu) \llbracket E_{11} \rrbracket \quad c \neq 0, \quad (3.10a)$$

$$\llbracket \underline{\sigma}^{1j} \rrbracket = \llbracket \underline{s}^j \rrbracket = 2\mu \llbracket E_{1j} \rrbracket \quad j \neq 1, \quad (3.10b)$$

$$\llbracket \underline{\sigma}^{j(j)} \rrbracket = \lambda \llbracket E_{11} \rrbracket = \frac{\lambda}{\lambda + 2\mu} \llbracket \underline{s}^1 \rrbracket \quad j \neq 1 \quad \text{and} \quad c \neq 0, \quad (3.10c)$$

$$\llbracket \underline{\sigma}^{23} \rrbracket = 0 \quad c \neq 0 \quad (3.10d)$$

$$\llbracket \underline{p}^i \rrbracket = \delta^{ij} \llbracket \rho v_j \rrbracket. \quad (3.10e)$$

We assume $c \neq 0$ to obtain the necessary conditions for admissible, nontrivial jumps. Equations (3.6), (3.8a), (3.10a) and (3.10e) generate the following system for the normal direction,

$$\begin{aligned} \llbracket \underline{s}^1 \rrbracket + c \llbracket \underline{p}^1 \rrbracket &= (\lambda + 2\mu) \llbracket \underline{E}_{11} \rrbracket + c\rho \llbracket \underline{v}_1 \rrbracket = 0, \\ c \llbracket \underline{E}_{11} \rrbracket + \llbracket \underline{v}_1 \rrbracket &= 0. \end{aligned} \quad (3.11)$$

A nontrivial solution can only be realized when $\lambda + 2\mu = c^2\rho$. That is, when $c = \pm c_d$, where

$$c_d = \sqrt{\frac{\lambda + 2\mu}{\rho}}, \quad (3.12)$$

is the dilatational (longitudinal) wave speed. Similarly, equations (3.6), (3.8b), (3.10b) and (3.10e) generate the necessary condition for the tangential directions $\underline{x}_j, j \neq 1$:

$$\begin{aligned} \llbracket \underline{s}^j \rrbracket + c \llbracket \underline{p}^j \rrbracket &= 2\mu \llbracket \underline{E}_{1j} \rrbracket + c\rho \llbracket \underline{v}_j \rrbracket = 0, \\ 2c \llbracket \underline{E}_{1j} \rrbracket + \llbracket \underline{v}_j \rrbracket &= 0. \end{aligned} \quad (3.13)$$

Thus, we must have $\mu = c^2\rho$ for nonzero jump values. That is, $c = \pm c_s$, where

$$c_s = \sqrt{\frac{\mu}{\rho}}, \quad (3.14)$$

is the shear wave speed. In other words, jumps in the normal and tangential fields can only occur on fronts moving normal to Γ at the longitudinal and shear wave speeds, respectively.

One-sided Riemann solution

Figure 3.3(a) shows a material interface and the local coordinate frame for $d = 2$. The setup for $d = 3$ is similar, with both the \underline{x}_2 and \underline{x}_3 -axes in the tangent plane of the manifold. We prescribe uniform initial data, $(\check{\mathbf{M}}, \check{\boldsymbol{\varepsilon}})$, as the set-up for a general, one-sided Riemann problem in which we seek the solution on the interior of the region whose outward surface normal is in the \underline{x}_1 -direction (*i.e.*, in the region to the left of the interface in the figure). We have shown that, in general, nontrivial jumps in the mechanical fields can only occur across d -manifolds with speeds $\pm c_d$ and $\pm c_s$. In the present one-sided configuration, the admissible speeds reduce to $-c_d$ and $-c_s$, as

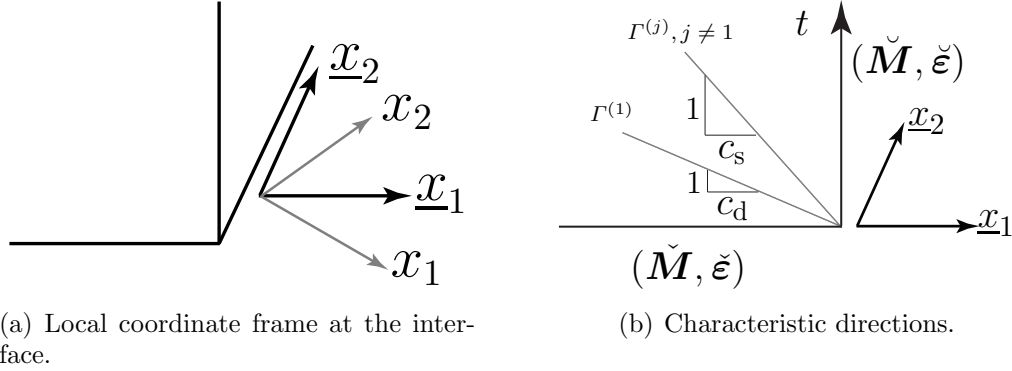


Figure 3.3: Riemann problem with data prescribed on only one side of a vertical material interface.

demonstrated in the figure. We seek the entire admissible set of fluxes on the material interface, denoted by $\check{\mathbf{M}}$ and $\check{\boldsymbol{\varepsilon}}$, that are consistent with the initial data. We use this admissible solution set to solve the full Riemann problem below. Moreover, this one-sided Riemann solution can be used to determine target values on material interfaces in multiphysics problems, such as solid-fluid interaction problems.

Let $\Gamma^{(1)}$ denote the d -manifold identified by $c = -c_d$. Equations (3.11) and (3.13) imply that only \underline{s}^1 and \underline{p}^1 can suffer jumps across $\Gamma^{(1)}$, in which case they must satisfy $\llbracket \underline{s}^1 - c_d \underline{p}^1 \rrbracket = 0$. Similarly, let $\Gamma^{(j)}$, $j \neq 1$, denote the manifolds identified with $c = -c_s$. For the tangential directions $\underline{x}_j, j \neq 1$, jumps in \underline{s}^j and \underline{p}^j can only occur across $\Gamma^{(j)}$ under the conditions $\llbracket \underline{s}^j - c_s \underline{p}^j \rrbracket = 0$. Thus, we define the *jump manifold speeds*, $\underline{\mathbf{c}}^{(j)} := \underline{c}^{(j)} \mathbf{e}_1$, in which

$$\underline{\mathbf{c}}^{(j)} = \begin{cases} -c_d & j = 1 \\ -c_s & j \neq 1. \end{cases} \quad (3.15)$$

Superscripts (j) denote the spatial direction, in the local frame, associated with each vector. The summation convention does not apply between j and (j) , since their meanings are distinct.

We define the *characteristic values*, $\underline{w}^{(j)} := \underline{s}^j|_{\Gamma^{(j)}} + \underline{\mathbf{c}}^{(j)} \underline{p}^j|_{\Gamma^{(j)}}$, as the j^{th} component of the vector coefficient of $\mathbf{M}|_{\Gamma^{(j)}}$; cf. (3.6). We can summarize all of the jump conditions as follows. The components \underline{s}^j and \underline{p}^j can only suffer jumps on $\Gamma^{(j)}$, subject to the constraint, $\llbracket \underline{s}^j + \underline{\mathbf{c}}^{(j)} \underline{p}^j \rrbracket = 0$. That is, for

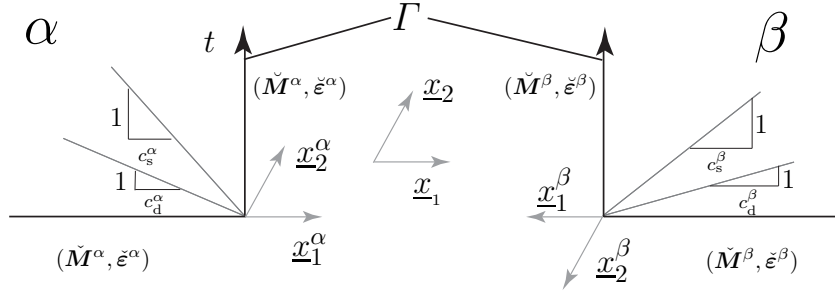


Figure 3.4: Riemann problem with distinct initial data on opposing sides, α and β , of a material interface Γ . Local coordinate directions $\underline{x}_j^{\alpha,\beta}$ correspond to the local frames used in the one-sided Riemann problems. The \underline{x}_j -directions indicate the local frame on Γ , which agrees (arbitrarily) with the local α frame in this illustration.

an arbitrary manifold Γ , with $c < 0$, we have, $\underline{s}^j|_\Gamma + \underline{c}^{(j)}\underline{p}^j|_\Gamma = \underline{w}^{(j)}$. Note that $\underline{w}^{(j)} = \underline{s}^j|_\Gamma + \underline{c}^{(j)}(\rho\delta^{ij}\underline{v}_i)|_\Gamma = \underline{s}^j|_\Gamma + \rho\underline{c}^{(j)}\underline{v}_j|_\Gamma$. In particular, when Γ is horizontal or vertical, we have

$$\check{s}^j + \rho\underline{c}^{(j)}\check{v}_j = \check{s}^j + \rho\underline{c}^{(j)}\check{v}_j = \underline{w}^{(j)}. \quad (3.16)$$

This equation determines the admissible set of fluxes on the vertical manifolds as a function of the initial data.

Two-sided Riemann problem

Figure 3.4 shows a general Riemann problem for a two-sided material interface Γ . Sides α and β have distinct initial data, $\check{M}^{\alpha,\beta}$ and $\check{\epsilon}^{\alpha,\beta}$, and material properties, $\rho^{\alpha,\beta}$, $\lambda^{\alpha,\beta}$ and $\mu^{\alpha,\beta}$; cf. (3.9). Equation (3.16) provides a general solution for $\check{M}^{\alpha,\beta}$ and $\check{\epsilon}^{\alpha,\beta}$ on Γ . Since Γ is vertical, these simplify to

$$\check{M}^{\alpha,\beta} = \check{\sigma}^{\alpha,\beta} \quad \check{\epsilon}^{\alpha,\beta} = \check{\nu}^{\alpha,\beta}. \quad (3.17)$$

The material boundaries on the opposing sides of Γ possess opposite orientations, as is evident in the local coordinate frames depicted in figure (3.4). Either of these orientations can be assigned to Γ without affecting the expressions in the following development, in which all vector and tensorial components are assumed to be defined with respect to the local \underline{x}_j coordinate frame on Γ . Thus, depending on the relation between $\underline{x}_j^{\alpha,\beta}$ and \underline{x}_j , it is

necessary to adjust the sign of some components defined with respect to the local coordinate frames used in the one-sided Riemann problems to obtain the corresponding components in the local frame on Γ . For example, in the case $d = 2$ with $\underline{x}_j = \underline{x}_j^\alpha$ illustrated in Figure 3.4, the components of the vector fields, \mathbf{p}^β , \mathbf{v}^β and \mathbf{c}^β , change sign when moving from the \underline{x}_j^β frame to the \underline{x}_j frame on Γ , while there is no sign change for the components of \mathbf{p}^α , \mathbf{v}^α , and \mathbf{c}^α . On the other hand, no net sign changes are required for the components of $\check{\mathbf{s}}^{\alpha,\beta}$, because these derive from the components of the second-order tensors, $\check{\boldsymbol{\sigma}}^{\alpha,\beta}$. It is evident from (3.16), then, that no net sign change is required for $\underline{w}^{(j)\alpha,\beta}$. Again, we emphasize that, provided that all components are expressed consistently with respect to the local coordinate frame on Γ , the expressions in the following development are valid and independent of which orientation is selected for Γ .

Balance of linear momentum must hold for all subdomains $\mathcal{Q} \subset \mathcal{D}$. Since $c = 0$ on Γ , equation (3.6) yields,

$$\llbracket \check{\mathbf{s}} \rrbracket = 0 \Leftrightarrow \check{\mathbf{s}}^\alpha = \check{\mathbf{s}}^\beta = \check{\mathbf{s}}. \quad (3.18)$$

The specific form of the jump condition for kinematic compatibility on Γ depends on whether the material interface is perfectly bonded, or in the case of stick, on the contact mode. It also may differ, depending on whether the normal or tangential local directions are considered. Equations (3.8a) and (3.8b) yield the appropriate jump conditions for the local direction j ,

$$\llbracket \check{\underline{v}}_j \rrbracket = 0 \Leftrightarrow \check{\underline{v}}_j^\alpha = \check{\underline{v}}_j^\beta = \check{\underline{v}}_j, \quad (3.19)$$

when kinematic compatibility is enforced for local direction j on Γ .

Riemann solution for bonded and contact–stick conditions

The jump conditions and Riemann solutions are identical for the cases where the material interface Γ is perfectly bonded or in the contact–stick mode, so we treat these cases together. Clearly, (3.19) holds for $j \in \{1, \dots, d\}$ in both cases. Thus, equations (3.16), (3.18) and (3.19) yield

$$\begin{aligned} \check{\underline{s}}^j + \rho^\alpha \underline{c}^{(j)\alpha} \check{\underline{v}}_j &= \underline{w}^{(j)\alpha} \\ \check{\underline{s}}^j + \rho^\beta \underline{c}^{(j)\beta} \check{\underline{v}}_j &= \underline{w}^{(j)\beta} \end{aligned} \quad (3.20)$$

for $j \in \{1, \dots, d\}$. The Riemann fluxes derived from (3.20) are called the *Riemann solution of the first kind*, and we denote them with symbols decorated by I . They are given by

$$\begin{aligned}\underline{s}_I^j &= \check{\underline{s}}_I^j = \llbracket \underline{w}^{(j)} / \rho \underline{c}^{(j)} \rrbracket / \llbracket (\rho \underline{c}^{(j)})^{-1} \rrbracket \\ &= \{ \llbracket \check{\underline{s}}^j / \rho \underline{c}^{(j)} \rrbracket + \llbracket \check{\underline{v}}_j \rrbracket \} / \llbracket (\rho \underline{c}^{(j)})^{-1} \rrbracket\end{aligned}\quad (3.21a)$$

$$\begin{aligned}\underline{v}_j^I &= \check{\underline{v}}_j^I = \llbracket \underline{w}^{(j)} \rrbracket / \llbracket (\rho \underline{c}^{(j)})^{-1} \rrbracket \\ &= \{ \llbracket \check{\underline{s}}^j \rrbracket + \llbracket \rho \underline{c}^{(j)} \check{\underline{v}}_j \rrbracket \} / \llbracket (\rho \underline{c}^{(j)})^{-1} \rrbracket\end{aligned}\quad (3.21b)$$

for $j \in \{1, \dots, d\}$. The expanded forms of (3.21) for the normal components of $\check{\underline{s}}_I$ and $\check{\underline{v}}^I$ are

$$\underline{s}_I^1 = \frac{\underline{w}^{(1)\alpha} \rho^\beta c_d^\beta + \underline{w}^{(1)\beta} \rho^\alpha c_d^\alpha}{\rho^\alpha c_d^\alpha + \rho^\beta c_d^\beta} = \frac{\check{\underline{s}}^{1\alpha} \rho^\beta c_d^\beta + \check{\underline{s}}^{1\beta} \rho^\alpha c_d^\alpha}{\rho^\alpha c_d^\alpha + \rho^\beta c_d^\beta} + \frac{\rho^\alpha \rho^\beta c_d^\alpha c_d^\beta}{\rho^\alpha c_d^\alpha + \rho^\beta c_d^\beta} \llbracket \check{\underline{v}}_1 \rrbracket\quad (3.22a)$$

$$\underline{v}_1^I = \frac{\llbracket \underline{w}^{(1)} \rrbracket}{\rho^\alpha c_d^\alpha + \rho^\beta c_d^\beta} = \frac{\llbracket \check{\underline{s}}^1 \rrbracket}{\rho^\alpha c_d^\alpha + \rho^\beta c_d^\beta} + \frac{c_d^\beta \rho^\beta \check{\underline{v}}_1^\beta + c_d^\alpha \rho^\alpha \check{\underline{v}}_1^\alpha}{\rho^\alpha c_d^\alpha + \rho^\beta c_d^\beta}.\quad (3.22b)$$

The same relations hold for tangential directions, if we replace c_d with c_s in (3.22). That is,

$$\underline{s}_I^j = \frac{\underline{w}^{(j)\alpha} \rho^\beta c_s^\beta + \underline{w}^{(j)\beta} \rho^\alpha c_s^\alpha}{\rho^\alpha c_s^\alpha + \rho^\beta c_s^\beta} = \frac{\check{\underline{s}}^{j\alpha} \rho^\beta c_s^\beta + \check{\underline{s}}^{j\beta} \rho^\alpha c_s^\alpha}{\rho^\alpha c_s^\alpha + \rho^\beta c_s^\beta} + \frac{\rho^\alpha \rho^\beta c_s^\alpha c_s^\beta}{\rho^\alpha c_s^\alpha + \rho^\beta c_s^\beta} \llbracket \check{\underline{v}}_j \rrbracket,\quad (3.23a)$$

$$\underline{v}_j^I = \frac{\llbracket \underline{w}^{(j)} \rrbracket}{\rho^\alpha c_s^\alpha + \rho^\beta c_s^\beta} = \frac{\llbracket \check{\underline{s}}^j \rrbracket}{\rho^\alpha c_s^\alpha + \rho^\beta c_s^\beta} + \frac{c_s^\beta \rho^\beta \check{\underline{v}}_j^\beta + c_s^\alpha \rho^\alpha \check{\underline{v}}_j^\alpha}{\rho^\alpha c_s^\alpha + \rho^\beta c_s^\beta},\quad (3.23b)$$

for $j = 2, 3$.

Equation (3.21b) defines a unique Riemann velocity vector for the fully bonded and contact–stick cases. The tangential traction is given by,

$$\boldsymbol{\tau}_I = \underline{s}_I^2 \mathbf{e}_2 + \underline{s}_I^3 \mathbf{e}_3.\quad (3.24)$$

In the case of contact–stick for a Coulomb friction model, the following inequality must hold,

$$|\boldsymbol{\tau}_I| \leq k \langle -\underline{s}_I^1 \rangle_+, \quad (3.25)$$

in which $|\boldsymbol{\tau}_I|$, k and $\langle \cdot \rangle_+$ are, respectively, the magnitude of the tangential

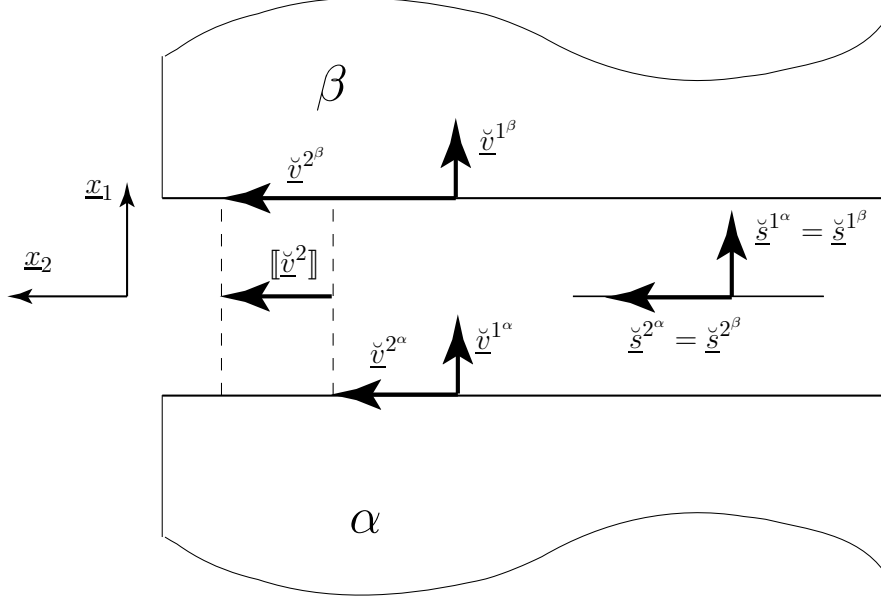


Figure 3.5: Traction and velocity vectors on opposite sides of an interface in the contact–slip mode.

traction, the Coulomb friction factor, and the positive part (*i.e.*, Heaviside) function. When the inequality (3.25) is not satisfied, we must investigate the Riemann solution for the contact–slip case, as developed below. For the fully-bonded case, (3.21) holds, independent of whether the solution satisfies inequality (3.25).

Riemann solution for contact–slip conditions

Contact–slip conditions hold when, *cf.* (3.25),

$$|\boldsymbol{\tau}_I| > k \langle -\underline{s}_I^1 \rangle_+. \quad (3.26)$$

Figure 3.5 depicts the tractions and velocities on a material interface in contact–slip mode for $d = 2$. Again, we define vector and covector components on both sides of the interface with respect to the local coordinate frame \underline{x}_j on Γ . In contact–slip mode, the tangential velocity may be discontinuous across the contact interface, so kinematic compatibility is only enforced in the normal direction. Thus, (3.19) holds only for $j = 1$, while the tangential components of the velocity may suffer jumps.

The entire traction vectors, on the other hand, must satisfy the jump

condition (3.18), subject to a suitable constitutive relation for friction. For simplicity, we adopt Coulomb's law of friction from here on in this work. Thus, the magnitudes of the tangential parts of the traction vectors are k times the compressive normal traction, and their direction coincides with $\llbracket \check{\mathbf{v}} \rrbracket$ when $\llbracket \check{\mathbf{v}} \rrbracket \neq \mathbf{0}$. Otherwise, we align the tangential tractions with those that would develop if contact–stick conditions were imposed [65].

Next, we develop the Riemann solution for contact–slip conditions. We call the resulting fluxes the *Riemann solution of the second kind*, and we decorate these quantities with ‘II’ to denote contact–slip mode. Since both (3.18) and (3.19) hold for the normal components of the solution, the normal components of the Riemann fluxes are identical to those in the contact–stick solution, as given in (3.22) for $j = 1$. The tangential components of the Riemann tractions conform to the modified Coulomb law described above. Thus, the Riemann solution for the tractions in contact–slip mode is given by

$$\underline{s}_{II}^j = \begin{cases} \underline{s}_I^1 & j = 1 \\ k \langle -\underline{s}_I^1 \rangle_+ (\mathbf{e}_{\check{\mathbf{v}}})^j & j \neq 1, \llbracket \check{\mathbf{v}} \rrbracket \neq \mathbf{0} \\ k \langle -\underline{s}_I^1 \rangle_+ (\mathbf{e}_{\boldsymbol{\tau}_I})^j & j \neq 1, \llbracket \check{\mathbf{v}} \rrbracket = \mathbf{0} \end{cases} \quad (3.27)$$

in which $\mathbf{e}_{\check{\mathbf{v}}} := \mathbf{R}(\llbracket \check{\mathbf{v}} \rrbracket) / |\mathbf{R}(\llbracket \check{\mathbf{v}} \rrbracket)|$ is the unit vector in the same direction as the tangential part of the covector $\llbracket \check{\mathbf{v}} \rrbracket$, *cf.* (2.10), and $\mathbf{e}_{\boldsymbol{\tau}_I}$ is, similarly, the unit vector in the direction of the tangential part of the traction $\boldsymbol{\tau}_I$. The definition of the characteristic value $\underline{w}^{(j)}$, (3.16) and (3.18) yield

$$\check{v}_j = \begin{cases} \underline{v}_1^I & j = 1 \\ \underline{w}^{(j)} / \rho \underline{c}^{(j)} - \underline{s}_{II}^j / \rho \underline{c}^{(j)} & j \neq 1. \end{cases} \quad (3.28)$$

We derive now an alternative form for (3.27) that does not depend on $\llbracket \check{\mathbf{v}} \rrbracket$, a problematic quantity in numerical implementations. Equations (3.28) and (3.21), for the case $j \neq 1$, yield

$$\llbracket \check{v}_j \rrbracket = \llbracket \underline{w}^{(j)} / \rho \underline{c}^{(j)} \rrbracket - \llbracket \underline{s}_{II}^j / \rho \underline{c}^{(j)} \rrbracket = (\underline{s}_I^j - \underline{s}_{II}^j) \llbracket (\rho \underline{c}^{(j)})^{-1} \rrbracket. \quad (3.29)$$

We substitute \underline{s}_I^j from (3.27) into (3.29) for the case $j \neq 1$, $[\check{\mathbf{v}}] \neq \mathbf{0}$ to obtain

$$\begin{aligned} [[\check{v}_j]] &= \left(\underline{s}_I^j - k \frac{[[\check{v}_j]]}{[[\check{\mathbf{v}}]]} \langle -\underline{s}_I^1 \rangle_+ \right) [(\rho \underline{c}^{(j)})^{-1}] \\ \Leftrightarrow |[\check{\mathbf{v}}]| \underline{s}_I^j &= \left(|[\check{\mathbf{v}}]| \frac{c_s^\alpha \rho^\alpha c_s^\beta \rho^\beta}{c_s^\alpha \rho^\alpha + c_s^\beta \rho^\beta} + k \langle -\underline{s}_I^1 \rangle_+ \right) [[\check{v}_j]], \end{aligned} \quad (3.30)$$

in which we have used the identity, $[(\rho \underline{c}^{(j)})^{-1}] = (c_s^\alpha \rho^\alpha + c_s^\beta \rho^\beta) / (c_s^\alpha \rho^\alpha c_s^\beta \rho^\beta)$ for $j \neq 1$. Equation (3.30) implies that the tangential components of $[\check{\mathbf{v}}]$ agree with $\boldsymbol{\tau}_I$ to within a positive constant when $[\check{\mathbf{v}}] \neq \mathbf{0}$. Thus,

$$(e_{\check{\mathbf{v}}})^j = (e_{\boldsymbol{\tau}_I})^j, \quad (3.31)$$

for $j \neq 1$, $[\check{\mathbf{v}}] \neq \mathbf{0}$. Combining (3.17), (3.21), (3.27), (3.28), (3.30), and (3.31), we obtain

$$\underline{s}_I^j = \begin{cases} \underline{s}_I^1 & j = 1 \\ k \langle -\underline{s}_I^1 \rangle_+ (e_{\boldsymbol{\tau}_I})^j & j \neq 1 \end{cases} \quad (3.32a)$$

$$\underline{v}_I^j = \begin{cases} \underline{v}_I^1 & j = 1, \\ \underline{w}^{(j)} / \rho \underline{c}^{(j)} - \underline{s}_I^j / \rho \underline{c}^{(j)} = \check{v}_j + (\check{s}^j - \underline{s}_I^j) / \rho \underline{c}^{(j)} & j \neq 1 \end{cases} \quad (3.32b)$$

Equation (3.32a) is valid, even if $[\check{\mathbf{v}}] = \mathbf{0}$; *cf.* (3.27). We emphasize that the tangential components of the Riemann velocities on opposing sides of the interface may be distinct; *cf.* (3.32b), in which superscripts α, β are suppressed.

Next, we investigate the behaviors of $[\check{\mathbf{v}}]$ and the alternative representations of $\boldsymbol{\tau}_I$ in (3.27) and (3.32a) at transitions between contact–stick and contact–slip modes. Equations (3.29), (3.32a), and $[[\check{v}^1]] = 0$ yield,

$$\begin{aligned} [[\check{v}_j]] &= (|\boldsymbol{\tau}_I| - |\boldsymbol{\tau}_I|) (e_{\boldsymbol{\tau}_I})^j [(\rho \underline{c}^{(j)})^{-1}], \quad j \neq 1 \\ \Leftrightarrow [\check{\mathbf{v}}] &= \frac{c_s^\alpha \rho^\alpha + c_s^\beta \rho^\beta}{c_s^\alpha \rho^\alpha c_s^\beta \rho^\beta} (|\boldsymbol{\tau}_I| - |\boldsymbol{\tau}_I|) \mathbf{e}_{\boldsymbol{\tau}_I} \end{aligned} \quad (3.33)$$

Since $|\boldsymbol{\tau}_I| - |\boldsymbol{\tau}_I| = |\boldsymbol{\tau}_I| - k \langle -\underline{s}_I^1 \rangle_+$, equations (3.26) and (3.33) imply that $[[\check{\mathbf{v}}]] > 0$ in slip mode, and $[[\check{\mathbf{v}}]] = 0$ at transitions between stick and slip modes.

Now, consider the continuity of the representation of $\boldsymbol{\tau}_I$ in terms of $[\check{\mathbf{v}}]$ in

(3.27). The function $k\langle -\underline{s}_I^1 \rangle_+$ is continuous, although not smooth, in \underline{s}_I^1 . The unit vector function, $\mathbf{e}_{\check{\mathbf{v}}}(\llbracket \check{\mathbf{v}} \rrbracket)$, on the other hand, is discontinuous at $\llbracket \check{\mathbf{v}} \rrbracket = \mathbf{0}$. Thus, for $\langle -\underline{s}_I^1 \rangle_+$ an arbitrary, strictly-positive number, $\boldsymbol{\tau}_H$ is discontinuous at $\llbracket \check{\mathbf{v}} \rrbracket = 0$ for the representation used in (3.27). This discontinuous behavior, which occurs at transitions between stick and slip modes, is well documented and necessitates special numerical treatment as $\llbracket \check{\mathbf{v}} \rrbracket \rightarrow 0$. For example, Karnopp [66] proposes the elimination of slip-mode kinematic degrees of freedom when the magnitude of the relative velocity across a contact interface falls below a specified threshold. Regularization of the Coulomb friction law, an alternative numerical remedy for the same problem, is proposed in [67, 65].

The alternative description of $\boldsymbol{\tau}_H$ in (3.32a) can be shown to circumvent the problem of discontinuity, as follows. Similar to $\mathbf{e}_{\llbracket \check{\mathbf{v}} \rrbracket}$, the unit vector function $\mathbf{e}_{\boldsymbol{\tau}_I}$ may be discontinuous at $\boldsymbol{\tau}_I = \mathbf{0}$. However, (3.26) and (3.33) imply that $|\boldsymbol{\tau}_H| = k\langle -\underline{s}_I^1 \rangle_+ < |\boldsymbol{\tau}_I|$. Thus, $\lim_{\boldsymbol{\tau}_I \rightarrow \mathbf{0}} \boldsymbol{\tau}_H = \mathbf{0}$, so that, in contrast to (3.27), (3.32a) provides a continuous representation for $\boldsymbol{\tau}_H$. In fact, equation (3.33) implies that $\llbracket \check{\mathbf{v}} \rrbracket$ can only approach zero along the direction $\mathbf{e}_{\boldsymbol{\tau}_I}$; and under this constraint, $\boldsymbol{\tau}_H$ is also a continuous function of $\llbracket \check{\mathbf{v}} \rrbracket$. However, since $|\boldsymbol{\tau}_I| \rightarrow |\boldsymbol{\tau}_H|$ as $\llbracket \check{\mathbf{v}} \rrbracket \rightarrow 0$, the unit vector function, $\mathbf{e}_{\check{\mathbf{v}}}(\llbracket \check{\mathbf{v}} \rrbracket)$, is ill-conditioned and highly sensitive to small perturbations of the velocity solution. This explains the numerical chatter in the tangential velocity and traction solutions at stick–slip transitions for models based on (3.27), as reported in [65]. The alternative model in (3.32a) circumvents these problems, and requires no special numerical treatments at stick–slip transitions.

Riemann solution for separation conditions

The conditions that identify parts of the contact set as being in separation mode are described in 3.2.2. These parts of the contact interface are treated the same as prescribed-traction boundaries, so the kinematic compatibility conditions (3.19) are completely relaxed to allow independent velocities on opposing sides of the interface. Typically, the prescribed-tractions are homogeneous. We decorate the Riemann values for this case with ‘*III*’ to indicate

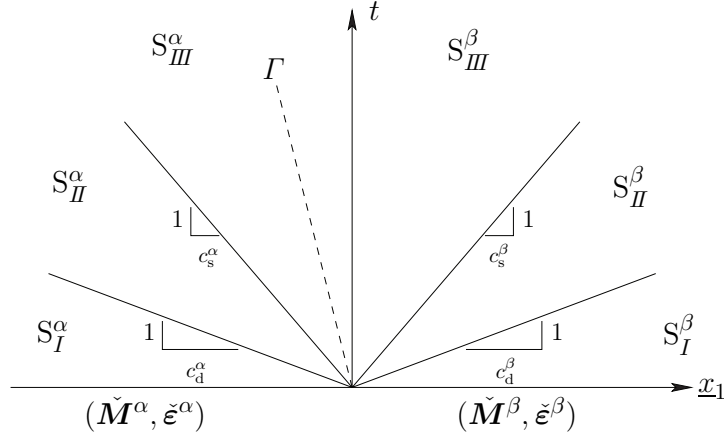


Figure 3.6: Sectors with distinct Riemann solutions used to classify the inclination of a d -manifold Γ with arbitrary orientation.

separation mode. Then (3.16) yields,

$$\underline{s}_{III} = \mathbf{0}, \quad (3.34a)$$

$$\underline{v}_j^{III} = \check{\underline{v}}_j^{III} = \frac{\underline{w}^{(j)}}{\rho \underline{c}^{(j)}} = \check{\underline{v}}_j + \frac{\check{\underline{s}}^j}{\rho \underline{c}^{(j)}} \quad j \in \{1, \dots, d\}, \quad (3.34b)$$

in which $\bar{\mathbf{s}}$ is the prescribed traction and the velocities in (3.34b) are distinct and independent on opposing sides α and β of the interface.

Riemann solution for arbitrary manifold orientation

Figure 3.6 displays all the sectors having distinct Riemann solutions in the local coordinate frame. We seek the Riemann solutions on a d -manifold Γ based on the initial data on both sides of the interface and the orientation of Γ . The spacetime domain on each side of the vertical interface is divided into three sectors, $S_I^{\alpha,\beta}$, $S_{II}^{\alpha,\beta}$ and $S_{III}^{\alpha,\beta}$, based on the longitudinal and shear wave speeds, $c_d^{\alpha,\beta}$ and $c_s^{\alpha,\beta}$, in which α and β identify the two sides of the interface. The d -manifold Γ can lie in any of these sectors. We will demonstrate that the Riemann solution in any sector can be expressed in terms of only the initial data, $(\check{\underline{\sigma}}^{\alpha,\beta}, \check{\underline{v}}^{\alpha,\beta})$, and the Riemann solutions on the vertical interface, denoted by $(\check{\underline{\sigma}}^{\alpha,\beta}, \check{\underline{v}}^{\alpha,\beta})$, which can be for any mode — bonded, contact–stick, contact–slip or separation; *cf.* (3.21), (3.32), and (3.34).

We use the fact that \underline{s}^j and \underline{v}_j can only suffer jumps across d -manifolds

with normal speeds $\pm \underline{c}^{(j)}$ subject to the constraint that $[[\underline{w}^{(j)}]] = 0$ to compute all components of the Riemann traction and velocity vectors. Equation (3.10c) and the fact that the shear component $\underline{\sigma}^{23}$ cannot suffer jumps on nonvertical interfaces determine the Riemann values of the off-normal components of the stress tensor. Finally, equation (3.7) implies that \underline{E}_{ij} , $i, j \neq 1$ can suffer arbitrary jumps across the vertical interface ($c = 0$), and this implies the same for $\underline{\sigma}^{ij}$. Combining these results, the complete Riemann solutions for sectors $S_{II}^{\alpha, \beta}$ and $S_{III}^{\alpha, \beta}$ are as follows,

$$\underline{s}^{1*} = \underline{\sigma}^{11*} = \underline{\check{s}}^1 \quad \text{Regions } S_{II}^{\alpha, \beta} \text{ and } S_{III}^{\alpha, \beta} \quad (3.35a)$$

$$\underline{v}_1^* = \begin{cases} \underline{\check{v}}_1^\alpha \\ \underline{\check{v}}_1^\beta \end{cases} \quad \begin{array}{l} \text{Regions } S_{II}^\alpha \text{ and } S_{III}^\alpha \\ \text{Regions } S_{II}^\beta \text{ and } S_{III}^\beta \end{array} \quad (3.35b)$$

$$\underline{s}^{j*} = \underline{\sigma}^{1j*} = \begin{cases} \underline{\check{s}}^{j\alpha} \\ \underline{\check{s}}^j \\ \underline{\check{s}}^{j\beta} \end{cases} \quad \begin{array}{l} \text{Region } S_{II}^\alpha \\ \text{Regions } S_{III}^{\alpha, \beta} \\ \text{Region } S_{II}^\beta \end{array} \quad j \neq 1 \quad (3.35c)$$

$$\underline{v}_j^* = \begin{cases} \underline{\check{v}}_j^\alpha \\ \underline{\check{v}}_j^\alpha \\ \underline{\check{v}}_j^\beta \\ \underline{\check{v}}_j^\beta \end{cases} \quad \begin{array}{l} \text{Region } S_{II}^\alpha \\ \text{Region } S_{III}^\alpha \\ \text{Region } S_{III}^\beta \\ \text{Region } S_{II}^\beta \end{array} \quad j \neq 1 \quad (3.35d)$$

$$\underline{\sigma}^{j(j)*} = \begin{cases} \underline{\check{\sigma}}^{j(j)\alpha} + \frac{\lambda^\alpha}{\lambda^\alpha + 2\mu^\alpha} (\underline{\check{s}}^1 - \underline{\check{s}}^{1\alpha}) \\ \underline{\check{\sigma}}^{j(j)\beta} + \frac{\lambda^\beta}{\lambda^\beta + 2\mu^\beta} (\underline{\check{s}}^1 - \underline{\check{s}}^{1\beta}) \end{cases} \quad \begin{array}{l} \text{Regions } S_{II}^\alpha \text{ and } S_{III}^\alpha \\ \text{Regions } S_{II}^\beta \text{ and } S_{III}^\beta \end{array} \quad j \neq 1 \quad (3.35e)$$

$$\underline{\sigma}^{23*} = \begin{cases} \underline{\check{\sigma}}^{23\alpha} \\ \underline{\check{\sigma}}^{23\beta} \end{cases} \quad \begin{array}{l} \text{Regions } S_{II}^\alpha \text{ and } S_{III}^\alpha \\ \text{Regions } S_{II}^\beta \text{ and } S_{III}^\beta \end{array} \quad (3.35f)$$

Furthermore, the Riemann fluxes on the causal sectors $S_I^{\alpha, \beta}$ are entirely determined by the initial data. That is, $\underline{\sigma}^* = \underline{\check{\sigma}}^{\alpha, \beta}$ and $\underline{v}^* = \underline{\check{v}}^{\alpha, \beta}$ in S_I^α and S_I^β , respectively. Since the Riemann velocities are distinct in the separation mode (III), and because the tangential components of the Riemann velocities are distinct in contact–slip mode (II), we assume distinct values for these values

on the vertical interface in (3.35b) and (3.35d). Obviously, these values must match for the bonded and contact–stick modes (I).

Equation (3.35) can easily be specialized for spatial dimensions $d = 1, 2$. Equation (3.35f) only applies to $d = 3$. For $d = 2$ under plane-stress conditions, equations (3.35c-e) are restricted to $j = 2$. Consequently, there is only one jump direction associated with each of the shear wave speeds $c_s^{\alpha,\beta}$ in figure 3.6. We can adapt these results to plane-strain conditions by replacing λ with $\hat{\lambda} = 2\mu\lambda/(\lambda + 2\mu)$. This substitution alters the longitudinal wave speeds $c_d^{\alpha,\beta}$ in (3.12), while the shear wave speed does not change. Thus, only the normal Riemann values are affected in (3.22) for the I and II cases in plane strain.

For $d = 1$, only (3.35a) and (3.35b) apply. There is no jump manifold associated with the shear wave speed $c_s^{\alpha,\beta}$ and there are only the four sectors, $S_I^{\alpha,\beta}$ and $S_{II}^{\alpha,\beta}$. There is no contact–slip solution and the Riemann solutions are limited to bonded and contact I and separation III modes. The longitudinal wave speed in (3.22) is computed according to $c_d = \sqrt{E/\rho}$, where E is the elastic modulus.

Equation (3.5) demonstrates that the restriction of \mathbf{M} to Γ only involves the normal (traction) components of the stress tensor. Although the equations (3.35e) and (3.35f) complete the Riemann stress solution, these off-normal components do not participate in the jump conditions.

3.2.2 Identification and regularization of the contact modes

This section describes methods for identifying the mesoscale contact modes (separation, contact–stick or contact–slip) in the neighborhood of any macroscopic point \mathbf{x} in the contact set $\tilde{\Gamma}$. These modes determine which of the Riemann solutions advanced in 3.2.1 hold at the mesoscale level, and these determine the macroscopic Riemann fluxes through a simple homogenization procedure described in 3.3. The transition between separation and contact is discontinuous, so we regularize that transition to facilitate numerical implementations. We use (3.32) to evaluate the Riemann fluxes in the contact–stick mode, and this makes the transition between contact–stick and contact–slip continuous and well-conditioned. Thus, no regularization is required for the stick–slip transition.

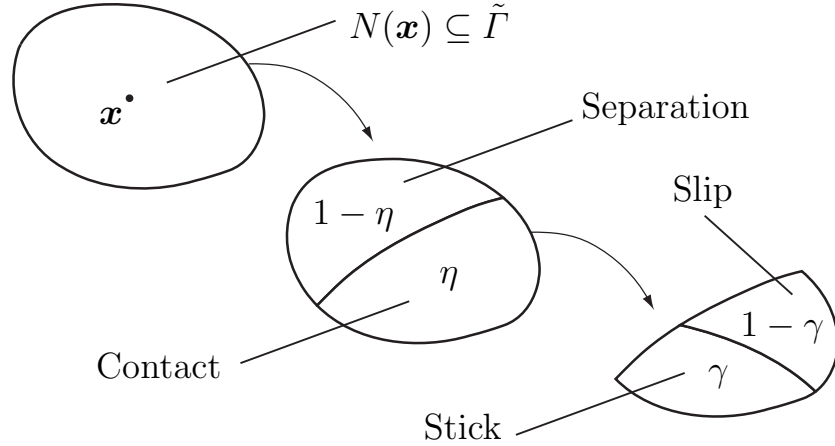
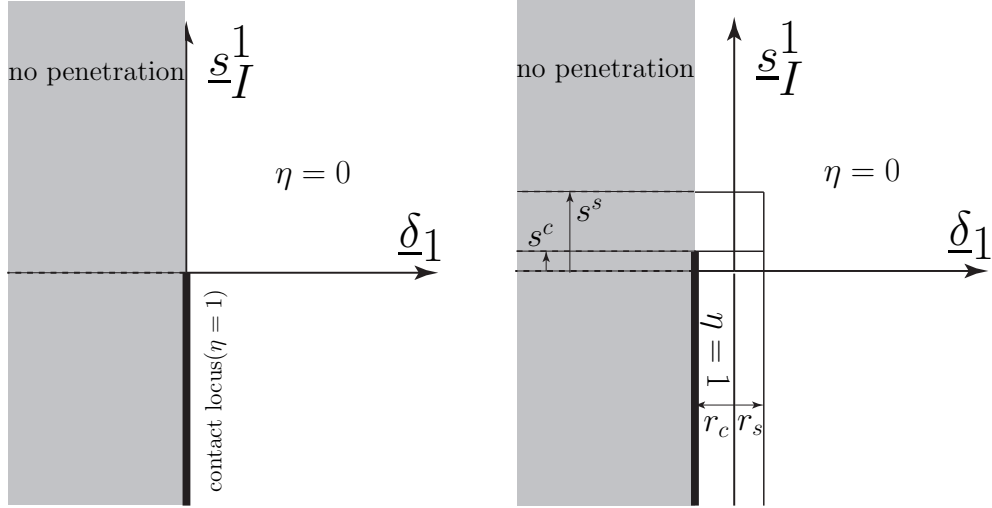


Figure 3.7: Mesoscale contact-mode hierarchy and area fractions in the neighborhood $N(\mathbf{x})$ of a macroscopic location $\mathbf{x} \in \tilde{\Gamma}$.

Figure 3.7 shows the hierarchy of mesoscale contact modes in the neighborhood $N(\mathbf{x})$ of a macroscopic location \mathbf{x} in the contact set $\tilde{\Gamma}$. At the first level of subdivision, $N(\mathbf{x})$ is partitioned into regions that are either in contact mode or in separation mode, with respective area fractions $\eta \in [0, 1]$ and $1 - \eta$, relative to the area of $N(\mathbf{x})$. The connectivities of these regions may be arbitrarily complex. However, the connectivities do not influence the macroscopic Riemann values generated by our simple homogenization scheme, so we are not concerned with them here. However, we do treat η as a continuous variable to support regularization of the separation–contact transition. The second level of subdivision partitions the contact region into contact–stick and contact–slip regions, with respective area fractions $\gamma \in \{0, 1\}$ and $1 - \gamma$ relative to the area of the contact region. We treat γ as a binary variable because we have no need to regularize the stick–slip transition. We next describe methods for identifying the mesoscale parameters, η and γ .

Contact area fraction

Figure 3.8 illustrates a scheme for distinguishing contact and separation modes based on the normal separation, $\underline{\delta}_1$ and the normal component of the contact Riemann traction \underline{s}_1^1 measured in any of the local coordinates described in section 3.2.1. Both of these quantities are sign insensitive to the choice of the local coordinate system. In view of the no-penetration condition, the physically admissible space is limited to $\underline{\delta}_1 \geq 0$ for a perfectly



(a) Contact scheme prior to regularization.

(b) Regularized contact scheme.

Figure 3.8: Identification and regularization of the contact and separation modes.

smooth interface. Consider, first, the basic scheme without regularization in Figure 3.8(a). The contact condition holds at points on the negative \underline{s}_I^1 axis, *i.e.*, $\underline{\delta}_1 = 0$ and $\underline{s}_I^1 < 0$. That is, contact ($\eta = 1$) occurs only when the separation vanishes and the normal traction is compressive. Otherwise, the separation mode ($\eta = 0$) prevails for the entire region $\underline{\delta}_1 \geq 0$.

Sharp transitions between separation and contact modes produce discontinuities in the mechanics solution fields in the form of weak shocks. For example, the velocity of a traction-free boundary in separation mode closing at velocity $v_0 > 0$ toward an opposing surface jumps from v_0 to 0 at the instant of contact. This extreme behavior causes a loss of convergence in many solution algorithms. We introduce the regularization scheme depicted in Figure 3.8(b), which is designed to smooth the abrupt transition between separation and contact modes, to remedy this problem. We regularize the contact area fraction η along both the normal contact–Riemann traction and the normal separation directions by writing,

$$\eta = \eta^\delta \eta^s, \quad (3.36)$$

in which the factors η^δ and η^s regularize the sharp transitions from positive to

zero separation and from traction-free to compressive tractions, as explained below.

Let $r_c \leq 0$ and r_s be the limiting separation values corresponding to full contact and full separation, as shown in Figure 3.8(b). Then we write

$$\eta^\delta = \begin{cases} 1 & : \quad \underline{\delta}_1 \leq r_c \\ \acute{r}(\acute{\delta}) & : \quad r_c < \underline{\delta}_1 < r_s \\ 0 & : \quad r_s \leq \underline{\delta}_1 \end{cases} \quad (3.37)$$

in which $\acute{\delta} := (r_s - \underline{\delta}_1)/(r_s - r_c)$ and \acute{r} is a function that smoothly interpolates between 0 and 1 over the interval $[0, 1]$. Possible choices for \acute{r} are

$$\acute{r}(\xi) = \begin{cases} \xi & : \quad \text{linear} \\ -2\xi^3 + 3\xi^2 & : \quad \text{cubic} \end{cases} \quad \text{for } 0 \leq \xi \leq 1. \quad (3.38)$$

We use the cubic form in this work, because it generates \mathcal{C}^1 transitions that facilitate the convergence of iterative solvers in our numerical implementation. Although r_c and r_s are here intended to describe a regularization of contact between perfectly smooth surfaces, surface roughness in real materials generates a similar gradual transition between separation and contact. Inclusion of a rigorous model for surface roughness effects would likely eliminate the need for regularization, but a formulation of this sort is beyond the scope of this study.

Let $s^c \geq 0$ and s^s denote limiting values of the normal surface stress corresponding to full contact and full separation modes in (3.39). Then we write

$$\eta^s = \begin{cases} 1 & : \quad \underline{s}_I^1 \leq s^c \\ \acute{r}(\acute{s}) & : \quad s^c < \underline{s}_I^1 < s^s \\ 0 & : \quad s^s \leq \underline{s}_I^1 \end{cases} \quad (3.39)$$

in which $\acute{s} = (s^s - \underline{s}_I^1)/(s^s - s^c)$.

The regularization (3.36), graphed in Figure 3.8(b), modifies the original contact range, $\underline{\delta}_1 = 0$ and $\underline{s}_I^1 \leq 0$, so that $\eta = 1$ when $\underline{\delta}_1 \leq r_c$ and $\underline{s}_I^1 \leq s^c$. It expands the original separation range so that $\eta = 0$ when $\underline{\delta}_1 \geq r_s$ or $\underline{s}_I^1 \geq s^s$. Elsewhere, η varies smoothly between 0 and 1. The Riemann values are determined by (3.34) when $\eta = 0$ (separation), and by (3.21) (contact–stick)

or (3.32) (contact–slip) when $\eta = 1$. We show in 3.3.1 that, elsewhere, η interpolates linearly between the Riemann values for separation and contact.

We demonstrate that the separation, δ cannot take values smaller than r_c . According to (3.34b) and (3.21a) we get $\llbracket v_1^{\text{III}} \rrbracket = \llbracket w^1 / \rho c^1 \rrbracket = \underline{s}_I^1 \llbracket (\rho c^1)^{-1} \rrbracket = \underline{s}_I^1 (c_d^\alpha \rho^\alpha + c_d^\beta \rho^\beta) / c_d^\alpha \rho^\alpha c_d^\beta \rho^\beta$. Furthermore, for contact modes, *I* and *II* compatibility condition for normal direction yields $\llbracket v_1^I \rrbracket = \llbracket v_1^{\text{II}} \rrbracket = 0$. The homogenized fluxes on the material interface are the area weighted averages of the mesoscopic divisions. That is,

$$\dot{\delta} = \llbracket \dot{v}^1 \rrbracket = (1 - \eta) \llbracket v_1^{\text{III}} \rrbracket = \frac{c_d^\alpha \rho^\alpha + c_d^\beta \rho^\beta}{c_d^\alpha \rho^\alpha c_d^\beta \rho^\beta} (1 - \eta) \underline{s}_I^1, \quad (3.40)$$

where $\dot{\delta}$ is the rate of separation. We assume that $\delta \geq r_c$ at initial time and demonstrate that this condition hold for subsequent times. The separation cannot cross the contact line $\eta = 1$, identified with $\delta = r_c$ and $\underline{s}_I^1 < s^c$ in figure 3.8(b) as $\dot{\delta} = 0$ for $\eta = 1$ according to (3.40). In addition $\dot{\delta} \geq 0$ for all $\underline{s}_I^1 \geq s^c$ following (3.40) and $s^c \geq 0$. That is, δ cannot decrease and take values smaller than r_c if initially $\delta \geq r_c$ for $\underline{s}_I^1 \geq s^c$. Consequently, δ cannot cross the line $\delta = r_c$ whether $\underline{s}_I^1 < s^c$ or not and this yields a minimum separation of r_c for the regularized model.

It is worth mentioning one alternative to regularization that might address the convergence problems associated with the separation–contact transition. Since the SDG model described in the next section can accommodate discontinuities across element boundaries, but not within elements, ensuring that spacetime element boundaries cover all contact–separation transitions would, presumably, alleviate the convergence problems. Less mesh refinement would be required than with the regularized model, where accuracy still requires strong mesh refinement at transitions that, although smoothed, still occur over very small scales. Although it seems feasible to modify our adaptive spacetime meshing procedure to satisfy this requirement, we do not consider this option further in this work.

Stick area fraction

Equation (3.25) determines whether the stick condition prevails in the contact mode. If the inequality is violated the contact–slip condition will hold. Unlike the transition between the separation and contact modes, we have shown

that there are no jumps in the Riemann fluxes associated with the transition between stick and slip modes when we use (3.32a) to compute the tangential tractions. This approach ensures good conditioning and circumvents the numerical problems encountered in some other methods. As a result, there are no convergence problems that would require regularization of the stick–slip transition, and we do not pursue this option in this work. That is, we restrict the value of γ to 0 and unity.

3.3 Spacetime discontinuous Galerkin formulation and implementation

3.3.1 Discretization

We obtain a spacetime discontinuous Galerkin (SDG) finite element method from the continuum problem formulated in 2.2 by associating the partition $\mathcal{P}(\mathcal{D})$ with a *spacetime finite element mesh* and the subdomains \mathcal{Q}_α with *spacetime elements* in the mesh. SDG solutions are continuous within each element, but allow jumps across element boundaries and on the domain boundaries relative to initial and boundary conditions. Consequently, the common jump set of all fields is identified by $\bigcup_\alpha \partial\mathcal{Q}_\alpha$. That is, the jump conditions (2.9), (2.13), and (3.1) are restricted to $\partial\mathcal{Q}_\alpha$ in the discrete formulation. We define the finite dimensional subspace,

$$\mathcal{V}_h = \left\{ \mathbf{u} \in \mathcal{V} : \mathbf{u}|_Q \in \mathcal{V}_h^Q \quad \forall Q \in \mathcal{P} \right\},$$

in which $\mathcal{V}_h^Q = \mathbf{P}^{k_Q}(Q)$, where $\mathbf{P}^{k_Q}(Q)$ is the space of covector fields on element Q whose components are complete polynomials of order k_Q . The polynomial order k_Q can be adjusted on a per-element basis in an *hp*-adaptive scheme.

We obtain a Bubnov-Galerkin weighted residual statement by weakly enforcing (2.12a) and the jump conditions (2.9), (2.13) and (3.1), in which the weighting functions, denoted by a superposed ‘ \wedge ’, occupy the same space \mathcal{V}_h defined for the displacement field in (3.3.1). The weighted residual problem is then stated as,

Problem 1 (Weighted Residuals Statement) Find $\mathbf{u} \in \mathcal{V}_h$ such that, for all $\mathcal{Q} \in \mathcal{P}(\mathcal{D})$,

$$\begin{aligned} & \int_{\partial\mathcal{Q}} \left[\mathbf{i}\hat{\boldsymbol{\varepsilon}} \wedge (\mathbf{M}^* - \mathbf{M}) + (\boldsymbol{\varepsilon}^* - \boldsymbol{\varepsilon}) \wedge \mathbf{i}\hat{\mathbf{M}} + \kappa\hat{\mathbf{u}} \wedge (\mathbf{u}_0^* - \mathbf{u}_0) \star dt \right] \\ & + \int_{\mathcal{Q}} \mathbf{i}\hat{\boldsymbol{\varepsilon}} \wedge (\mathbf{d}\mathbf{M} - \rho\mathbf{b}) = 0 \quad \forall \hat{\mathbf{u}} \in \mathcal{V}_h \end{aligned} \quad (3.41)$$

in which the constant κ is introduced to ensure dimensional consistency [12].

The Stokes theorem applied to (3.41) and an interchange of the projection operator from \mathbf{u} to $\hat{\mathbf{u}}$, generates the discrete weak form that defines our finite element method:

Problem 2 (Weak Form)

$$\begin{aligned} & \int_{\partial\mathcal{Q}} \left[\mathbf{i}\hat{\boldsymbol{\varepsilon}} \wedge \mathbf{M}^* + (\boldsymbol{\varepsilon}^* - \boldsymbol{\varepsilon}) \wedge \mathbf{i}\hat{\mathbf{M}} + \kappa\hat{\mathbf{u}}_0 \wedge (\mathbf{u}^* - \mathbf{u}) \star dt \right] \\ & - \int_{\mathcal{Q}} (\mathbf{d}\mathbf{i}\hat{\boldsymbol{\varepsilon}} \wedge \mathbf{M} + \mathbf{i}\hat{\boldsymbol{\varepsilon}} \wedge \rho\mathbf{b}) = 0 \quad \forall \hat{\mathbf{u}} \in \mathcal{V}_h \end{aligned} \quad (3.42)$$

The solution to (3.42) exactly satisfies the integral forms of balance of linear momentum and balance of angular momentum over every spacetime element $\mathcal{Q} \in \mathcal{P}(\mathcal{D})$ [12].

Next, we determine the target fluxes on $\partial\mathcal{Q} \cap \tilde{\Gamma}$. The jump integrands on \mathbf{u} vanish in (3.41) and (3.42) since $\tilde{\Gamma}$ is vertical and $\star dt|_{\tilde{\Gamma}} = 0$. Let a_κ denote the absolute area fraction for contact mode κ , where κ can stand for S (separation), ST (contact–stick) or SL (contact–slip). The definitions of the relative area fractions, η and γ , yield

$$a_S = 1 - \eta \quad (3.43a)$$

$$a_{ST} = \eta\gamma \quad (3.43b)$$

$$a_{SL} = \eta(1 - \gamma). \quad (3.43c)$$

The macroscopic target fluxes are area-weighted averages of their constituent mesoscale Riemann values. Since the restrictions of \mathbf{M}^* and $\boldsymbol{\varepsilon}^*$ on $\tilde{\Gamma}$ reduce

to $\boldsymbol{\sigma}^*$ and \boldsymbol{v}^* , we obtain,

$$\boldsymbol{M}^* = \boldsymbol{\sigma}^* = a_\kappa \boldsymbol{\sigma}_\kappa^*, \quad (3.44a)$$

$$\boldsymbol{\varepsilon}^* = \boldsymbol{v}^* = a_\kappa \boldsymbol{v}_\kappa^*. \quad (3.44b)$$

The area-weighted average fluxes in (3.44) can also be obtained by using the subdivisions depicted in figure 3.7 to evaluate the integrals in (3.42). In the absence of regularization, the target values in (3.44) can only take the values given in (3.21), (3.32), or (3.34). However, with regularization, the target values can also be weighted averages of (3.34) and either (3.21) or (3.32).

3.3.2 Implementation

We use unstructured grids to discretize the spacetime analysis domain directly. This contrasts with *semi-discrete* numerical methods where space is discretized independently of time to generate a system of ODEs to be solved by an explicit or implicit time-marching scheme. This artificially imposes severe concurrency constraints on hyperbolic models that are not intrinsic to the underlying physics. In the SDG solution scheme, we obtain computational complexity that scales linearly with the number of spacetime elements by working with the system’s characteristic structure and by treating meshing and solution in a more unified fashion. The SDG approach eliminates the restrictive notion of a global time step to produce scalable, asynchronous, adaptive algorithms with local conservation properties on individual elements. Preserving characteristic structure also provides intrinsic stability to SDG models that, in the present application, eliminates the need for stabilization. However, we do require meshes one dimension higher than the spatial domain.

We use an algorithmic framework, called *Tent Pitcher* [68, 70], for computing unstructured tetrahedral meshes in 2D×time. Our method advances a two-dimensional front through time, starting with a triangular mesh of the underlying two-dimensional domain at the initial time. Elements are added to the evolving spacetime mesh in small *patches* by moving a single vertex of the front forward in time. The time-advance for a given vertex is limited by a *causality constraint*, determined by the characteristic structure of the underlying PDE, and by a *progress constraint* that guarantees that we can

construct meshes to any desired terminal time.

The patch tetrahedra are formed by connecting the advanced vertex to its previous spacetime location and to its neighbor vertices in the front. We compute the solution within each new patch as soon as it is created, since our discontinuous basis functions and causality-based meshing procedure preclude coupling with subsequent patches. The duration of each spacetime element depends only on the local feature size and on the quality of the underlying space mesh (not on a global time step). Patches with no causal relationship can be generated and solved independently and in parallel, reflecting the finite wave speeds in real physical systems. Thus, we interleave the spacetime meshing and finite-element solution procedures at relatively fine granularity to obtain a scalable algorithm that is, by nature, asynchronous and easy to parallelize. Assuming linear response in the bulk material, the nonlinearity of the cohesive model only affects elements adjacent to the the contact set $\tilde{\Gamma}$. Thus, nonlinear iterations are only required in the patch-level solutions for the relatively few patches with faces on $\tilde{\Gamma}$. This represents a significant savings relative to methods that must iterate globally to resolve nonlinearities.

Our algorithm employs dynamic, adaptive refinement and coarsening of the advancing front in response to local *a posteriori* error estimates returned by the SDG solver [13, 69, 23, 71]. We use two adaptive error indicators to drive the adaptive meshing; one measures numerical dissipation in the bulk solution and the other measures the difference between the target Riemann fluxes on the contact set $\tilde{\Gamma}$. If the solver reports an error estimate above some preset threshold for either measure, the patch is rejected, and our algorithm refines the front without advancing it. If both error estimates are below some lower threshold, the patch is accepted, and our algorithm attempts to coarsen that portion of the front before its next advance. A change in the front induces a corresponding refinement or coarsening of future elements in the spacetime mesh. The adaptive algorithm produces strongly graded spacetime meshes that effectively capture shocks and the sharp transitions between contact modes. With refinement ratios as small as 10^{-6} , our models can bridge length scales from millimeters down to nanometers.

Common two-dimensional remeshing operations, such as mesh smoothing, edge flips and vertex deletion, are implemented in spacetime as special patches whose facets perfectly match the old front. Thus, in contrast to

spatial remeshing procedures, in which remeshing necessitates projection operations that accumulate $\mathcal{O}(h)$ error, no projection operations are required in our SDG implementation. This preserves the element-wise conservation properties and the high-order convergence properties of the underlying SDG method and makes our h -adaptive implementation particularly effective in resolving the sharp wavefronts that typically arise in elastodynamic contact.

3.4 Numerical results

This section presents numerical results for contact/separation solutions within our SDG finite element framework. First, we investigate a problem where, on contact set, condition switches between contact and separation mode. We aim to study the effectiveness and accuracy of the method to resolve the correct solution, in particular in capturing the loci which correspond to switches between the two modes. We also investigate the influence of regularization parameters (*cf.* section 3.2.2) on the accuracy as well as cost of our results. In the second example, we study the transfer between contact stick and slip modes.

All of the studies in this section are based on tetrahedral spacetime elements with complete cubic polynomial bases under plain strain condition. The material properties are Young’s modulus, $E = 3.24$ GPa; Poisson’s ratio, $\nu = 0.35$; and mass density, $\rho = 1190$ kg/m³ for all the results in this section. For these values of the material parameters, the dilatational and shear wave speeds are $c_d = 2090$ m/s and $c_s = 1004$ m/s.

3.4.1 Contact/separation Example

The domain and load description of the first problem is illustrated in figure 3.9. Figure 3.9(a) depicts the square region of edge size $L = 4$ mm which is completely debonded on the mid-plane. Since the solution fields are uniform along x_1 , from here on, we suppress the direction arguments from all mechanical fields; the normal stress, and vector components are all in x_2 direction. We model an infinite domain where the spatially uniform wave carrying stress load $\check{\sigma}(t)$ arrives on the top and bottom boundaries of the computational region at time $t = 0$. The periodic boundaries are employed to model the infinite domain condition. To satisfy this requirement along the

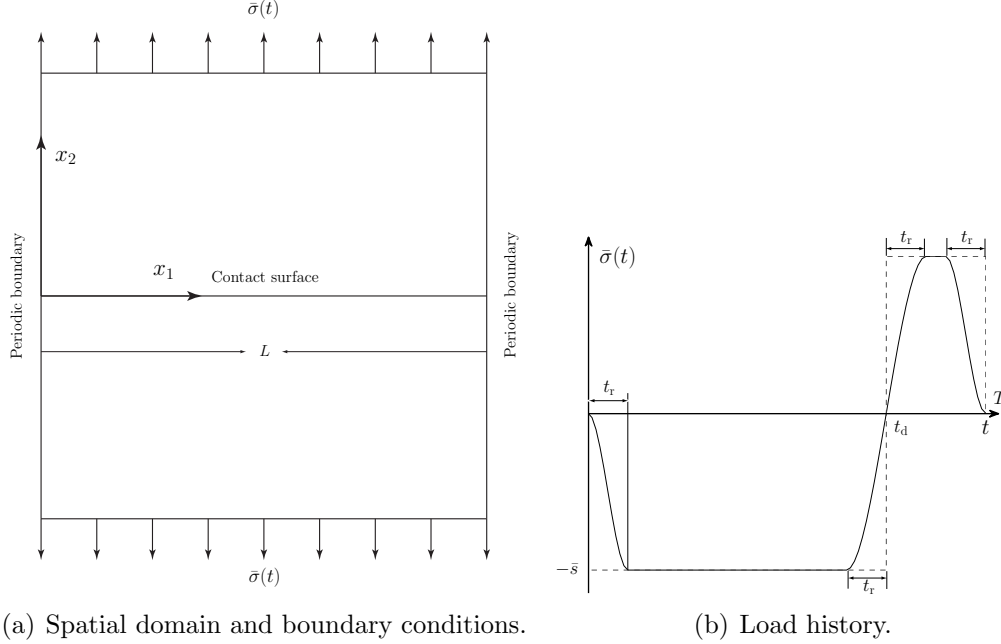


Figure 3.9: Geometry and load description for contact/separation example.

vertical axis we treat the stress wave $\check{\sigma}(t)$ as a load carrying certain characteristic value. The velocity carried by stress wave is equal to $-\check{\sigma}(t)/c_d\rho$ which makes the characteristic value $2\check{\sigma}(t)$ according to (3.16). In order to model infinite domain condition we employ (3.21) to compute the target values where w traces are taken to be $2\check{\sigma}(t)$ and that computed from the interior trace on the two sides of the computational domain at $x_2 = \pm L/2$.

The history of loading $\check{\sigma}(t)$ is demonstrated in figure 3.9(b). The incoming wave is a periodic wave of period $T = 2 \mu\text{s}$ which initially takes the value $-\bar{s} = -100 \text{ MPa}$ from time $t = 0$ to $t_d = 0.75T$, then it jumps to \bar{s} from t_d to T as depicted by dash line in the figure. In order to reduce the computational cost we regularize the loading in the intervals of $t_r = 0.1T$ through cubic polynomials which result in \mathcal{C}^1 continuous loading. Since there is no reflection off the domain boundaries at $x_2 = \pm L/2$ the characteristic load, $w = \check{\sigma}(t)$, is directly translated to contact surface with delay time equal to $t_0 = L/2c_d \approx 0.96 \mu\text{s}$.

Figure (3.10) illustrates the solution on contact surface for regularization parameters $r_c = -10^{-3} \text{ mm}$, $r_s = 0$, $s^c = 0$, and $s^s = 600 \text{ kPa}$ (*cf.* section 3.2.2). For this specific parameter set, the regularization is entirely on neg-

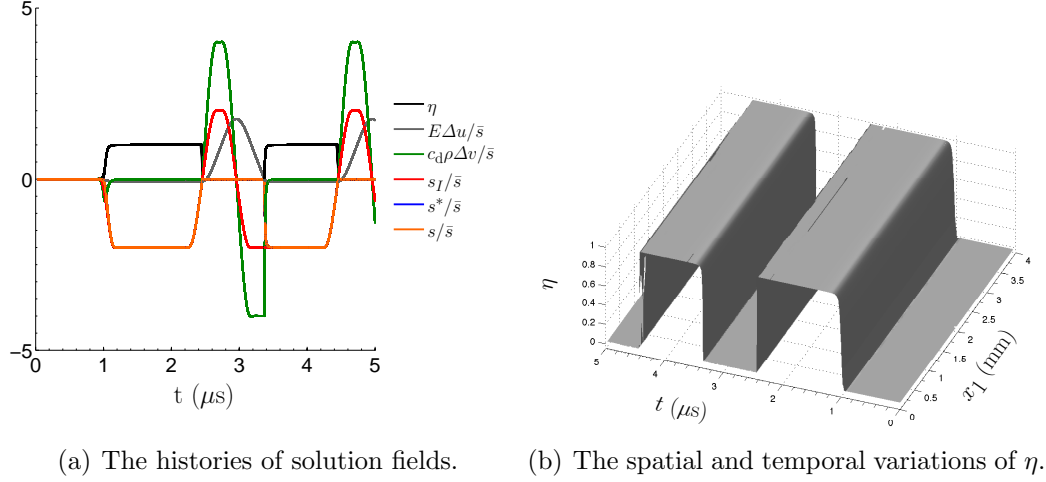


Figure 3.10: The solution on contact interface for $r_c = -10^{-3}$ mm, $r_s = 0$, $s^c = 0$, and $s^s = 600$ kPa.

active parts of the axes in figure 3.8. Since the fields are uniform along this axis the solution should be identical for all x_1 values. However, our numerical SDG solutions may exhibit small perturbations along this axis. In order to capture such variations, we show the solution for all constant x_1 values as a function of time in figure 3.10(a).

The incoming wave carrying characteristic load $w(t) = 2\check{\sigma}(t)$ reaches the contact surface with the delay time t_0 from both sides of the interface. Since the characteristics are equal on the two sides of the interface, (3.21) yields $s_I(t+t_0) = w(t) = 2\check{\sigma}(t)$ and $v^I(t+t_0) = 0$ for $t \geq 0$. The numerical solution for s_I confirms this relation.

At time $t = t_0$ we have $\Delta u = 0$ and $s_I = 0$ and equations (3.37), (3.39), and (3.36) yield $\eta^\delta = 0$, $\eta^s = 0 \Rightarrow \eta = 0$. Thus, the interface will be in separation mode at this instance. Equation (3.34) yields $s_{III} = 0$ and $v^{III} = -w/c_d\rho$ for separation mode. Since w ramps up from zero to negative value $-2\bar{s}$ we get $v^{III} > 0$ which corresponds to penetration at the interface. That is, $\Delta u \rightarrow r_c$ which in turn implies $\eta^\delta \rightarrow 1$. Moreover, since $s_I = w$ quickly exceeds s^c we get $\eta^s \rightarrow 1$. This process is demonstrated in figure 3.10(a) as η approaches unity in the interval of about $0.1 \mu\text{s}$ after t_0 . In this interval, the target values shift from purely separation to purely contact mode according to (3.44). We notice closing $\Delta v = -2v$ in this range as $\Delta u \rightarrow r_c^+$. Afterward, the interface is entirely in contact; equation (3.21)

yields the target values $s^* = s_I = w$ and $v^* = 0$ which implies zero Δv and sustained value of $\Delta u = r_c$. The slight negative separation of r_c is evident in the figure. As mentioned in section 3.2.2 and shown in the figure, r_c corresponds to the minimum separation at the interface.

The interface is completely in contact as we approach $t = t_0 + t_d \approx 2.46 \mu\text{s}$. At about $0.01 \mu\text{s}$ before this time, s_I attains the value s^c . Consequently, in this short interval η^s approaches zero from unity according to (3.39). Thus, equation (3.36) implies $\eta = 0$ at $t_0 + t_d$. The separation Δu does not change appreciably in this interval and $\eta^\delta \approx 1$. However, the form of (3.39) guarantees the separation mode as $\Delta u \rightarrow r_s$ or $s_I \rightarrow s^s$. Note that, the transition from contact to separation mode is mostly done through the regularization of η^s .

We have pure separation mode in the interval from $t = t_0 + t_d$ to approximately $t_0 + 5T/4 \approx 3.46 \mu\text{s}$. Equation (3.34) yields $s^* = 0$ and $v^* = -w/c_d\rho = -s_I/c_d\rho \Rightarrow \Delta v = 2s_I/c_d\rho$. That is, the characteristic load is completely transferred to velocity. Our numerical results capture these features as shown in figure 3.10(a). Since $\Delta u \geq r_s = 0$ in this interval, we have $\eta^\delta = 0$ which in turn yields $\eta = 0$. The contact Riemann traction s_I takes negative values for $t > t_0 + T$ which is transferred to closing velocity. As $\Delta u \rightarrow r_s$, the impinging characteristic load $w = s_I$ takes the constant value of $-2\bar{s} \ll s^c$. Equations (3.39) and (3.36) yield $\eta^s = 1 \Rightarrow \eta = \eta^\delta$; in contrary to previous transition, herein, the shift between contact and separation modes is through the regularization of η^δ . The relative velocity Δv , which takes the value of $-4\bar{s}/c_d\rho$ for $\Delta u = r_s$, causes the closing of the interface until $\Delta u = r_c$. That is the interface shifts from pure separation to pure contact mode in a very short interval. The regularization of η^δ is responsible for the smooth transition of fields in this interval. As shown in the figure, the characteristic wave is completely transferred to traction in the contact mode. That is, $s = s^* = -2\bar{s}$ and $\Delta v = 0$.

Note that as opposed to the two previous instances of shift between contact and separation modes, the characteristic load w does not change sign and in fact it takes the constant value of $-2\bar{s}$ here. This is an example of shock features which are inherent to the contact/separation problem. That is, the solution fields may suffer jumps even if the applied loads are smooth as in this example. In fact, if we did not regularize η^δ (*i.e.*, $r_c = r_s$), the jumps in s and v would happen immediately. This explains the need for

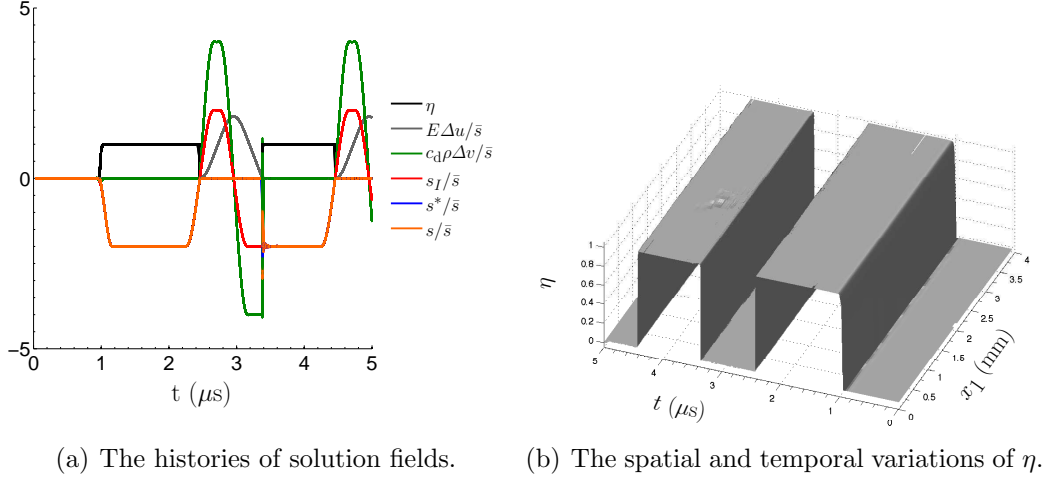


Figure 3.11: The solution on contact interface for $r_c = -10^{-4}$ mm, $r_s = 0$, $s^c = 0$, and $s^s = 60$ kPa.

regularization of η if we do not explicitly track the shock fronts. Otherwise, there may be convergence problems for patches which include these features.

The interface remains in pure contact mode from $t \approx t_0 + 5T/4$ to $t = t_0 + t_d + T \approx 4.46 \mu s$. The transition from pure contact to pure separation mode, just before the end of the interval, is similar to that at $t = t_0 + t_d$. In fact, the solution of the problem is periodic for $t \geq t_0 + t_d$ with the same period of applied load, T . The curves in figure (3.10(a)) imply that the numerical solution is in fact uniform along the x_1 axis. Figure 3.10(b) illustrates the spatial as well as temporal variations of η on the contact surface. It is evident that η is fairly uniform along the x_1 axis.

In order to study the effects of regularization, we solve the same problem with the new parameter set $r_c = -10^{-4}$ mm, $r_s = 0$, $s^c = 0$, and $s^s = 60$ kPa. That is, the regularization is 10 times tighter for both η^s and η^δ . We present the results for this problem in figure 3.11. In comparison to figure (3.10), there are much sharper transitions between contact and separation modes. Moreover, the penetration at contact mode appears to be zero in figure 3.11 due to 10 times smaller value for r_c .

We direct our attention to the transition from separation to contact mode around $t = t_0 + 5T/4 \approx 3.46 \mu s$. As mentioned before, the regularization of η^δ is the only mechanism for a smooth transition between the two modes and the solution to the problem without regularization exhibits a true shock

at this time. We observe undershoot and overshoot in the fields s and v in figure 3.11(b). Furthermore, there is slight discrepancy between s and s^* . None of these features are observed in figure 3.10(b). The spacetime mesh for the first set of parameters contains about 1.4 million tetrahedra with a minimum element size of approximately 2.6×10^{-3} mm. The corresponding values for the second problem are 4.4 million tetrahedra and 2.8×10^{-4} mm, respectively. That is, as expected, the solution becomes more expensive as the regularization approaches zero while the contact/separation problem is solved more accurately.

The solution scheme presented in this chapter captures the shocks in the transition between contact and separation modes. That is, the shock (or regularized shock) fronts cross within the element and element boundaries. We can track the shocks if we do not regularize the transition and align the sharp shock fronts with element boundaries. Since our SDG finite element method readily admits jumps between element boundaries the shock tracking method can exactly represent the solution. This approach is, however, beyond the scope of this work.

3.4.2 Stick–Slip Example

Figure 3.12 shows the geometry and applied loads on the square region with edge size $L = 4$ mm. The domain is debonded on the mid-plane as depicted in the figure. The compressive load $\check{\sigma}(t)$ ramps over an interval of $t_r = 0.2 \mu\text{s}$ from zero to a sustained value, $\bar{s} = 100$ MPa. Similar to section 3.4.1, the load is applied as a wave with the characteristic value $w(t) = 2\check{\sigma}(t)$ which reaches the computational domain boundary at $t = 0$. That is, the domain is of infinite size along the vertical direction and the same characteristic load impinges on the contact surface with the delay time of $t_0 = L/2c_d \approx 0.96 \mu\text{s}$. The lateral loads are given by $\bar{\pi}(t) = 100t/12$ MPa. The regularization parameters are chosen as $r_c = 0$, $r_s = 10^{-5}$ mm, $s^c = 0$, and $s^s = 125$ kPa. The Coulomb’s friction coefficients are set to $k_l = k_u = 0.25$ which implies that there is no regularization for γ . The terminal time of the simulation is $t_f = 12 \mu\text{s}$.

Figure 3.13 presents a series of still images from the animation of the SDG solution generated by the per-pixel-accurate rendering procedure of Zhou *et al.* [72]. The color field depicts the log of the strain-energy density, where

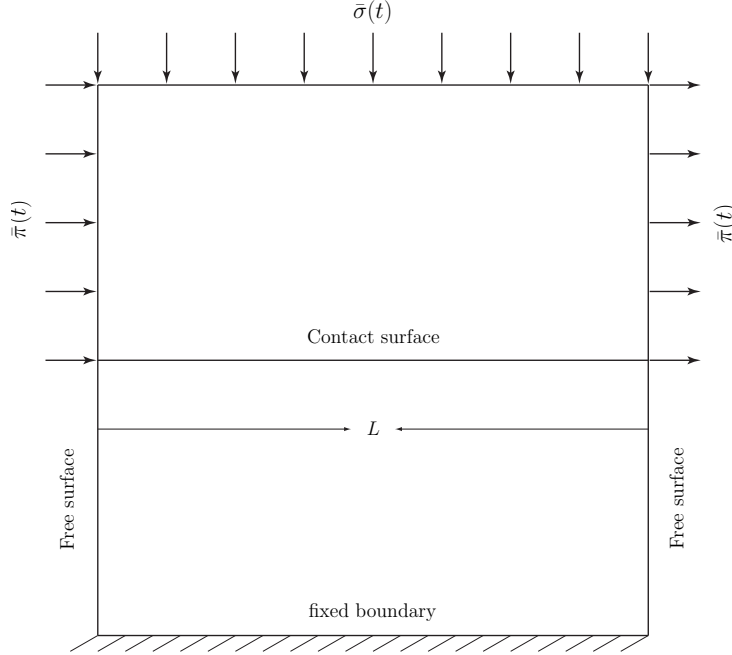


Figure 3.12: Geometry and load description for contact stick and slip example.

blue indicates zero energy density and violet indicates peak values. The color field is rendered on the deformed geometry.

Figure 3.13(a) shows the domain slightly after the reflection of the normal wave front off the bottom edge passes the contact surface at $t = 3.0 \mu\text{s}$. The interface has gone through very small slips due to the application of lateral loads for $t < t_0$ when normal traction is zero. The slip takes its maximum near the edges of the interface where larger tangential tractions are induced for longer periods of time (due to the linear nature of $\bar{\pi}(t)$ and progress of its normal shock fronts from the edges toward the center of the domain). Overall the slips for $t < t_0$ are negligible and are hardly visible in figure 3.13(a). However, the passage of the shock front generated by $\check{\sigma}(t)$ from contact interface at $t \approx t_0$ generates diagonal waves on the edges of the interface where very small slip has occurred. For example, the diagonal wave initiated at the left edge of the interface at $t \approx t_0$ can be clearly observed in this figure.

As the lateral load increases it induces larger values for $|\boldsymbol{\tau}_I|$ which eventually violates (3.25) and causes local slip events on the interface. Figure 3.13(b) demonstrates an instance where small slip is evident on the edges of

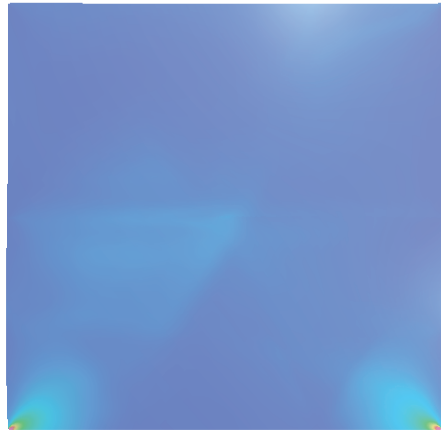
the interface at $t = 7.0 \mu\text{s}$. The slip magnitudes become much larger in figures 3.13(c) and 3.13(d) which correspond to times $t = 9.0 \mu\text{s}$ and $t = 12.0 \mu\text{s}$, respectively. The spacetime mesh for this problem contains about 0.9 tetrahedra with the smallest element size equal to 3.7×10^{-4} mm. The physical dissipation associated with friction is equal to 2.04×10^{-2} J which is about %30.6 of the total inflow energy to the spacetime domain. The numerical dissipation [12, 13] is only %0.02 of the inflow energy.

3.5 Conclusions

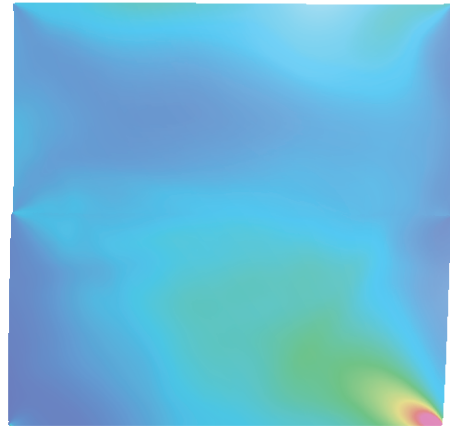
We have presented the Riemann solutions and an adaptive spacetime discontinuous Galerkin (SDG) finite element implementation for elastodynamic contact problem. We express our mechanical fields and the governing equations using the differential form approach. The coefficients of the differential forms might suffer jumps, so the exterior derivative of a form generally contains a diffuse part and a jump part. The jump parts of kinematic compatibility conditions and those obtained from the application of the Stokes theorem on the balance of momentum provide a unified framework to specify fluxes across arbitrary domain boundaries. The target fluxes are determined either from initial/boundary conditions on the domain boundary or from the solution to a local Riemann problem.

The Riemann solutions provide the mathematically and physically correct target fluxes on manifolds with arbitrary orientation in space and time. Herein, we have presented a novel solution scheme for the Riemann fluxes where the admissible jump manifolds and their jump conditions are directly derived from the application of jump parts associated with the balance of linear momentum and the kinematic compatibility conditions. This is followed by the determination of the allowable set of Riemann target fluxes on an arbitrary material interface. The target fluxes for a specific interface condition, are derived by matching these solutions from the opposite sides of the interface.

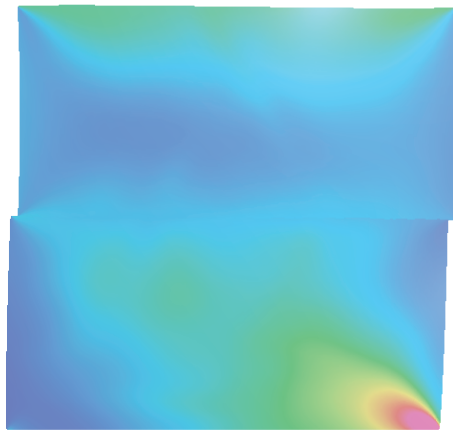
Specifically, we obtained the Riemann fluxes for bonded, contact–stick, contact–slip, and separation modes, which to our knowledge have not been reported before. We should emphasize that the Riemann solutions exactly preserve the characteristic structure of the incoming elastodynamic waves from



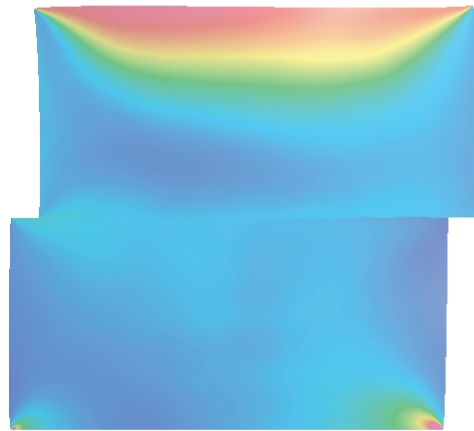
(a) $t = 3.0 \mu\text{s}$.



(b) $t = 7.0 \mu\text{s}$.



(c) $t = 9.0 \mu\text{s}$.



(d) $t = 12.0 \mu\text{s}$.

Figure 3.13: Visualization of slip along the contact surface on the deformed geometry. Color depicts log of strain-energy density.

opposite sides of the interface. The treatment of contact conditions in many numerical methods violates this structure. For example, we demonstrate that the Riemann fluxes are identical for contact–stick and bonded modes. This identification does not hold in penalty methods, where the application of large stiffness values for penetrating displacements replaces the displacement continuity conditions required otherwise. Unlike the Lagrange multiplier method the treatment of contact conditions is localized to the patches that have nonempty intersection with the contact surface. Furthermore, no additional degrees of freedom such as Lagrange multipliers are required in our method.

We employ the Coulomb’s law of friction to determine the transition between stick and slip modes. The direction of slip traction is determined from the sliding velocity of the two sides of the interface $[[\mathbf{v}]]$, when $[[\mathbf{v}]] \neq 0$, otherwise it is aligned with the tangential traction that would have acted under the stick mode. The direction of slip velocity is discontinuous at $[[\mathbf{v}]] = 0$ which in turn makes the slip traction discontinuous [67,65]. The condition of zero slip velocity is actually realized under the transitions between the stick and slip modes. Thus, numerical methods that employ $[[\mathbf{v}]]$ for the determination of the direction of slip traction, typically experience large oscillations in slip traction under the stick/slip mode changes. The regularization of Coulomb’s friction law [67,65] and the elimination of slip degrees of freedom for small contact velocity magnitudes [66] are a few of remedies reported in the literature. Herein, we have demonstrated that for linearly homogeneous solids, the slip velocity is aligned with the tangential traction that would have acted under the stick mode. Thus, instead of $[[\mathbf{v}]]$, we can determine the direction of slip traction from the stick mode traction. This approach eliminates the problems posed by the discontinuous behavior of the Coulomb’s law at $[[\mathbf{v}]] = 0$ (*cf.* section 3.2.1).

We have presented the conditions associated with contact mode transitions; the interface undergoes the contact mode only if the separation is zero and the normal traction is compressive. The transition between the stick and slip modes is determined from the Coulomb’s friction law. The contact/separation mode changes may introduce shocks in velocity and stress fields as shown in section 3.4.1 and described in [40]. We have presented a regularization scheme for the contact mode transitions.

The regularization of contact and separation transition is done in nar-

row bands of normal separation and traction. The examples in section 3.4.1 have demonstrated the influence of the regularization parameters on the accuracy and cost of the solution; as the transition bands shrink, the solution approaches the nonregularized solution and the cost of simulation increases. The regularization eliminates the possible nonconvergent problems associated with the shocks generated by contact/separation shocks. It also provides a means to control the cost and accuracy of the simulation. Finally, the stick/slip transition does not introduce any shocks in stress and velocity fields. Thus, no regularization is required for such transitions. In fact, we used the nonregularized form of this transition for our numerical example in section 3.4.2. The regularization can, however, be employed as a means to control the cost and accuracy of numerical results. In general, the element-level balance of momentum, the use of Riemann solutions, dual adaptivity controls [13], and linear complexity of the numerical scheme enabled us to very accurately resolve the transitions between distinct contact modes.

Several extensions can be considered to our current work. Many contact problems involve large displacements, where two points that initially do not correspond to opposite sides of an interface may come into contact. The solution to this class of problems generally involves searching algorithms [73, 74], which detect the contact points on the opposite sides of the interface. Large deformations [74], not only are accompanied by large displacements, but also involve geometry and possibly material nonlinear effects. The Riemann solutions presented here are no longer valid for nonlinear material response, which requires a new set of solutions for contact modes.

Chapter 4

A two-scale, delayed-damage cohesive model for dynamic fracture and contact problems

4.1 Introduction

As observed in many experimental results [75, 76], the high stress fields generated around a moving crack tip nucleate small cracks and voids at defects that are randomly distributed in the material. The crack advances by the process of void growth and coalescence. Damage models, generally, represent the process of material degradation, such as void growth, according to a specific evolution law. Several numerical methods have been proposed for modeling the damage process. Johnson studies the propagation of cracks by introducing a bulk damage model, where cracks are identified as regions in the bulk domain with large damage values. In contrast, the crack is modeled as a sharp material interface in *interfacial damage models* [77, 78, 79].

We present a new two-scale interfacial damage cohesive fracture model that represents mesoscale processes of void growth and coalescence. The evolution of a single damage parameter D , which represents the debonded area fraction on cohesive interfaces, is governed by an irreversible, time-delay evolution law characterized by a cohesive strength and a relaxation time $\tilde{\tau}$ that determines the maximum damage rate. The time scale $\tilde{\tau}$, combined with dynamic effects, introduces an implicit length scale and removes mesh sensitivity problems [80] that are otherwise encountered with the use of a static damage models [81].

We enforce the Riemann fluxes for the fully-bonded condition in the undamaged area fraction $(1 - D)$ of the cohesive interface, while the Riemann fluxes for the contact–stick, contact–slip or separation conditions determine the fluxes in the debonded area fraction. These mesoscale Riemann values are averaged to derive macroscopic cohesive conditions.

Many different types of cohesive models may change the bulk material properties as they fail to reproduce the physically correct fluxes for the

bonded interface mode. As an example, we mention the artificial compliance and possible convergence problems [82] encountered when *intrinsic traction separation relation*(TSR) cohesive models are inserted between all element boundaries in a finite element implementation. The interfacial damage models in [77, 78, 79] assume a linear elastic relation on the bonded area fraction and are primarily used for modeling of interlaminar fracture modes. These models may also produce artificial compliance when modeling fracture modes other than delamination. Our cohesive model, on the other hand, does not artificially change the bulk material properties as it enforces the physically correct Riemann fluxes for different contact modes at the interface.

Under dynamic, especially cyclic loading conditions, the fracture response is affected by the dynamic contacts of crack surfaces to a large degree [83]. A variety of numerical methods for the simultaneous modeling of contact and fracture have been proposed. For example, Dolbow *et al.* [84] present an eXtended finite element (X-FEM) modeling of crack growth with frictional contact. In the context of traction separation relations, contact and separation modes are represented with a single constitutive relation and large penalty values are employed to approximately enforce the material impenetration condition. The accurate rendering of the contact conditions requires large penalty values, which in turn may result in stiff global stiffness matrices and nonconvergence problems, as it is the general trend with penalty methods [34]. The extensions of TSRs to frictional contact can be found in [85, 86, 87]. In interfacial damage models [88, 89], the contact and separation modes are modeled with distinct constitutive relations on the damaged area fraction. Similar to [77, 78, 79], they employ a linear elastic relation on the bonded area fraction, which may change the bulk material properties as explained above. Our damage model, on the other hand, enforces the correct contact and separation Riemann solutions on each of the mesoscopic area fractions.

The crack propagation in brittle materials is generally associated with complex features such as crack path oscillations, microcrack, and crack branching events [75, 76, 90, 91, 92]. A large number of numerical methods have been proposed to investigate the formation of these complex features. In general, the crack topology is unknown *a priori* and should be obtained as a part of the solution. Specifically, the methods that model cracks as sharp discontinuities, comprise the majority of existing methods.

The sharp material interfaces can be implemented either between adjacent finite elements or within elements, as in the extended finite element method [93, 84, 94, 95], the generalized finite element method (G-FEM) [96, 97], and other methods with embedded strong discontinuities [98, 99, 100]. When the discontinuities are aligned with element boundaries the TSR cohesive models are widely practiced. In the case of intrinsic TSRs, the cohesive faces are inserted between all element boundaries in order to compute the crack topology [14, 101]. The initial stiffness of the TSR in these models introduces artificial compliance and can even lead to convergence problems in implicit simulations [82, 102].

We present an *spacetime discontinuous Galerkin (SDG)* implementation of our interfacial damage cohesive model to simulate solution-dependent crack path problems. This work is an extension to [12, 23, 13], where a general formulation of elastodynamics problem and specifically an implementation of cohesive models in the SDG framework are presented. We use the SDG scheme’s adaptive meshing capabilities to freely nucleate and extend cohesive interfaces to capture solution-dependent crack paths. The SDG adaptive meshing aligns the boundaries of spacetime elements with crack-path trajectories having arbitrary position and orientation. The cracks nucleation is based on a probabilistic model, which attempts to model the nucleation process from randomly distributed defects observed experimentally [75, 76]. The treatment of defects as random distribution variables can be found in several computational models such as [103, 104].

The element-level balance of momentum, use of Riemann solutions, dual adaptivity error indicators [13], and linear complexity of the SDG method leads to a very accurate and efficient solution scheme. Combined with our crack propagation scheme, the SDG implementation provides a method that does not suffer the limited resolution and mesh-dependent effects encountered in most other numerical fracture models. Numerical results in 4.5 demonstrate crack propagation, microcrack formation and crack branching phenomena.

4.2 Formulation

This chapter presents a two-scale, delay-damage cohesive model for dynamic fracture and contact problems that is designed for dynamic fracture problems in materials, such as polymethyl methacrylate (PMMA), where void nucleation and growth is the primary mechanism of fracture. It might also be appropriate for other classes of materials where the fracture mechanism can be modeled as localized debonding across a material interface. We do not address material damage in the bulk in the present development, although this plays a significant role in the physics of dynamic fracture in many materials, including PMMA. Thus, adding a model that describes damage in the bulk material would be a natural extension of this work.

A macroscopic damage parameter D describes the area fraction of debonded interface in the mesoscopic neighborhood $N(\mathbf{x})$ of a point \mathbf{x} on a cohesive interface. The damage parameter vanishes where the interface is undamaged, and $D = 1$ where the interface is, locally, completely damaged, *i.e.*, debonded. A time-delay equation governs the macroscopic evolution of D in response to the local stress state, while the standard Riemann solution for a material interface holds in fully bonded mesoscopic zones and the contact model developed in the previous chapter governs the interfacial response in mesoscopic, debonded regions. Rather than refer to a traction-separation relation, we use a simple averaging of the mesoscopic model to determine the macroscopic cohesive response.

We define the *cohesive set* of the spacetime domain \mathcal{D} , denoted by $\tilde{\Gamma}$, as the union of all vertical d -manifolds in $\overline{\mathcal{D}}$ where the damage evolution law is in effect, independent of whether any damage has yet accumulated. In general, $\tilde{\Gamma}$ must be determined as part of the solution process. We present a probabilistic nucleation and growth model for cohesive interfaces based on a random distribution of material defects. A propagation criterion determines the directions of extension at the tips of existing cohesive interfaces. Part or all of the cohesive set can be specified *a priori* to investigate crack propagation or contact along known material interfaces.

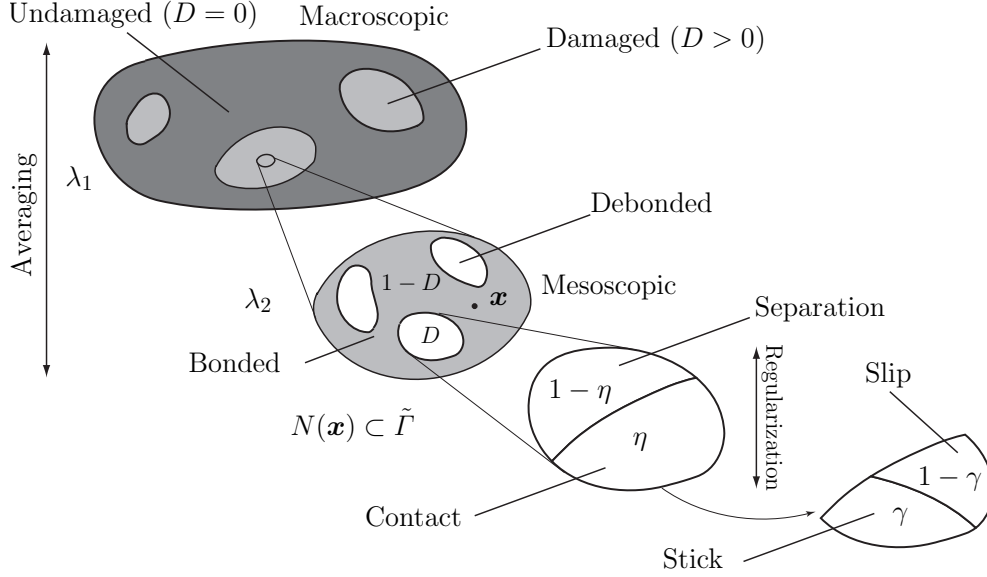


Figure 4.1: Mesoscale region hierarchy for the combined damage–contact model in the neighborhood $N(\mathbf{x})$ of a point $\mathbf{x} \in \tilde{\Gamma}$.

4.2.1 Mesoscopic model, area fractions and Riemann solutions

Figure (4.1) depicts the area subdivisions on a cohesive interface. At the *macroscopic* level, the value of D indicates whether the interface is *undamaged* ($D = 0$) or *damaged* ($0 < D \leq 1$). In damaged areas, the interface is partially debonded due to void nucleation and growth or to some other interface damage mechanism. The mesoscopic neighborhood $N(\mathbf{x})$ of a point \mathbf{x} in a damaged region can be subdivided into *bonded* and *debonded* regions. These regions exist at the *mesoscopic* level, and we have $\lambda_2 \ll \lambda_1$, where λ_1 and λ_2 are the macroscopic and mesoscopic length scales, respectively. The undamaged part of the cohesive set is assumed to be fully bonded.

The parameter $D(\mathbf{x})$ is the area fraction of the debonded part of $N(\mathbf{x})$ relative to the area of $N(\mathbf{x})$. Hence, the area fraction of the bonded part is $1 - D$. Furthermore, the debonded part has two possible states, *separation* and *contact*, that depend on the values of the normal separation and the traction. The respective area fractions of the contact and separation regions, relative to the total area of the debonded part of $N(\mathbf{x})$, are η and $1 - \eta$. Finally, we partition the contact part of $N(\mathbf{x})$ into contact–stick and contact–slip parts according to a suitable friction model, such as the Coulomb

friction law. We denote the area fractions of the contact–stick and contact–slip zones, relative to the total contact area in $N(\mathbf{x})$, as γ and $1 - \gamma$.

The separation, stick and slip regions all exist at the mesoscopic level, and the debonded part of $N(\mathbf{x})$ is comprised of just one of these states in sharp-transition models. However, regularization of the contact–separation transitions might result in the separation mode coexisting with either of the two contact modes in the neighborhood of the same point \mathbf{x} ; *cf.* 4.2.2.

Let a_κ denote the absolute area fractions, *i.e.*, the area fractions relative to $N(\mathbf{x})$, of the regions at the bottom of the hierarchy depicted in Figure 4.1. Then, based on the definitions of D , η and γ , we have

$$a_B = 1 - D \quad a_S = D(1 - \eta) \quad a_{ST} = D\eta\gamma \quad a_{SL} = D\eta(1 - \gamma), \quad (4.1)$$

subject to

$$\sum_{\kappa \in \mathcal{R}} a_\kappa = 1, \quad (4.2)$$

where $\mathcal{R} := \{B, S, ST, SL\}$ is the *mesoscopic region set* in which B stands for *bonded*, S for *separation*, ST for *contact–stick* and SL for *contact–slip*. We use Greek indices (up for covectors; down for vectors) to denote the components of mechanics fields associated with mesoscopic regions in \mathcal{R} ; we invoke a summation convention over \mathcal{R} for repeated Greek indices.

Now we derive relations between the macroscopic and mesoscopic traces on $\tilde{\Gamma}$ of the characteristic values $\underline{w}^{(j)}$, the momentum flux components \underline{s}^j and the velocity components \underline{v}_j based on the following statements.

1. The trace of the macroscopic momentum flux at $\mathbf{x} \in \tilde{\Gamma}$ must equal the average trace of the mesoscopic momentum flux over $N(\mathbf{x})$. This follows as a direct consequence of balance of linear momentum.
2. We assume that any high-frequency deviations over $N(\mathbf{x})$ in the traces of the mesoscale characteristic values from the corresponding macroscopic traces at \mathbf{x} are negligible. Therefore, we may equate the macroscopic trace and all of the individual mesoscopic traces of the characteristic values. That is,

$$\underline{w}_\kappa^{(j)} = \underline{w}^{(j)} \Leftrightarrow \underline{v}_j^\kappa = \underline{v}_j + (\underline{s}^j - \underline{s}_\kappa^j) / \rho \underline{c}^{(j)}, \quad j = 1, \dots, d. \quad (4.3)$$

These two statements, the vertical orientation of \tilde{I} , (4.2) and (4.3) imply

$$\mathbf{s} = a_\kappa \mathbf{s}_\kappa \quad (4.4a)$$

$$\mathbf{v} = a_\kappa \mathbf{v}_\kappa \quad (4.4b)$$

According to (4.3), the mesoscale regions in $N(\mathbf{x})$ share the same trace for each characteristic value. Nonetheless, each mesoscale region can have a distinct combination of stress and velocity. For example, consider a one-dimensional bar with a cohesive interface at its midpoint pulled on its two ends by a suddenly applied tensile stress $\bar{\sigma}$. Immediately after the wavefront reaches the cohesive interface, its macroscopic characteristic value (from either side) is $2\bar{\sigma}$ due to additive interference. This characteristic value resolves as $\underline{s}^1 = 2\bar{\sigma}$ and $\underline{v}_1 = 0$ in a bonded mesoscale region, and as $\underline{s}^1 = 0$ and $\underline{v}_1 = -2\bar{\sigma}/(c\rho)$ (opening mode) in a mesoscale region in separation mode. In either case, the trace of the mesoscale characteristic value is $2\bar{\sigma}$.

Next, we show that the mesoscopic Riemann values can be computed directly from the trace of the macroscopic solution on \tilde{I} . Equations (3.21), (3.32), (3.34) with $\bar{\mathbf{s}} = \mathbf{0}$, (4.3) and (4.5) yield,

$$(\underline{s}_R^j)_\kappa = \begin{cases} \llbracket \underline{\check{w}}^{(j)} / \rho \underline{c}^{(j)} \rrbracket / \llbracket (\rho \underline{c}^{(j)})^{-1} \rrbracket = \underline{s}_I^j & \text{R} = I, \kappa \in \{\text{B, ST}\}, j \in \{1, \dots, d\} \\ (\underline{s}_I^1)_\kappa = \underline{s}_I^1 = \underline{s}_II^1 & \text{R} = II, \kappa = \text{SL}, j = 1 \\ k \langle -\underline{s}_I^1 \rangle_+ (e_{\tau_I})^j = \underline{s}_II^j & \text{R} = II, \kappa = \text{SL}, j \neq 1 \\ 0 = \underline{s}_III^j & \text{R} = III, \kappa = \text{S}, j \in \{1, \dots, d\} \end{cases} \quad (4.5a)$$

$$(\underline{v}_j^R)_\kappa = \begin{cases} \llbracket \underline{\check{w}}^{(j)} \rrbracket / \llbracket (\rho \underline{c}^{(j)})^{-1} \rrbracket = \underline{v}_j^I & \text{R} = I, \kappa \in \{\text{B, ST}\}, j \in \{1, \dots, d\} \\ \underline{v}_1^I = \underline{v}_1^{II} & \text{R} = II, \kappa = \text{SL}, j = 1 \\ \underline{\check{w}}^{(j)} / \rho \underline{c}^{(j)} - \underline{s}_II^j / \rho \underline{c}^{(j)} = \underline{v}_j^{II} & \text{R} = II, \kappa = \text{SL}, j \neq 1 \\ \underline{\check{w}}^{(j)} / \rho \underline{c}^{(j)} = \underline{v}_j^{III} & \text{R} = III, \kappa = \text{S}, j \in \{1, \dots, d\} \end{cases} \quad (4.5b)$$

These important results can be summarized as,

$$(\mathbf{s}_R)_\kappa = \mathbf{s}_R \quad (4.6a)$$

$$(\mathbf{v}^R)_\kappa = \mathbf{v}^R \quad (4.6b)$$

in which $(R, \kappa) \in \{(I, B), (I, ST), (II, SL), (III, S)\}$. Thus, we can obtain the mesoscopic Riemann solutions directly from the traces of the macroscopic solution on $\tilde{\Gamma}$ without computing the traces of the mesoscopic solution.

4.2.2 Damage evolution model; identification and regularization of mesoscopic area fractions

In this subsection, we describe the damage evolution model and determine the area fractions of the mesoscopic regions. We modify the basic expressions for the area fractions to account for a regularization of the transition between contact and separation.

Damaged area fraction

The damage parameter D can be obtained through a static equation or by integrating an evolution equation. Static damage models are incapable of describing fracture properly unless they are modified in some way to introduce a microscopic length scale [77]. Without this modification, they develop highly mesh-dependent response in numerical simulations in the strain-softening regime [81]. On the other hand, the time scales associated with damage-evolution models, combined with dynamic effects, introduce implicit microscopic length scales that tend to reduce or eliminate mesh sensitivity [80]. In these models, g is obtained from the integration of an evolution rule of the form,

$$\dot{D} = D'(\mathbf{s}_\kappa^{\alpha,\beta}, \mathbf{v}_\kappa^{\alpha,\beta}, \mathbf{u}_\kappa^{\alpha,\beta}, D), \quad (4.7)$$

in which D' is a scalar function, κ ranges over the macroscopic fields as well as the mesoscopic fields in \mathcal{R} , while α, β denote traces from the two sides of the cohesive interface.

In this work, we consider damage-delay evolution models, similar in structure to those proposed in [77], in which the existence of a maximum damage rate is assumed so that the change in D due to load variations is not instantaneous. In particular, the damage parameter D evolves according to

$$\dot{D} = \begin{cases} \frac{1}{\tilde{\tau}}[1 - H(\langle f(y) - D \rangle_+)] & D < 1 \\ 0 & D = 1 \end{cases}, \quad (4.8)$$

where $\tilde{\tau}$ is a *relaxation time*, y is the *damage inducer*, and $f(y)$ is called the

stationary damage value. The function H attains the value of 1 at zero and monotonically decreases to 0 at infinity. The relaxation time $\tilde{\tau}$ is the time scale associated with local fracture processes, and in general, it is several orders of magnitude smaller than the time scales in classical viscoelasticity or viscoplasticity models [77]. When the time scales over which the applied loads vary are much larger than $\tilde{\tau}$, we have $\langle f(y) - D \rangle_+ \rightarrow 0$. In the limit of this quasi-singular behavior, the damage evolution takes the form,

$$D(t) = \sup_{s \leq t} f(y(s)). \quad (4.9)$$

That is, D takes the maximum value of the stationary damage over time.

The property, $H(0) = 1$, ensures that $\dot{D} = 0$ when the stationary damage value is less than or equal to the current damage value. Furthermore, the model attains its maximum damage rate $1/\tilde{\tau}$, in the limit, as $f(y) - D \rightarrow \infty$, since H monotonically decreases to zero at infinity. One can observe that the delay effect decreases as H tends less strongly to 0.

Following [77], the particular form of H used in this work is given as,

$$H(x) = \exp(-ax). \quad (4.10)$$

The damage inducer y is a function of the effective Riemann traction on the bonded part of the interface,

$$y = g\left(\frac{\tilde{s}_I}{\tilde{\sigma}}\right), \quad (4.11)$$

in which the *effective Riemann traction* combines normal and tangential components of the Riemann traction vector acting on the interface,

$$\tilde{s}_R = \sqrt{\langle \underline{s}_R^1 \rangle_+^2 + \beta^2 \sum_{j=2}^d (\underline{s}_R^j)^2}, \quad (4.12)$$

where β is the *shear stress factor* that controls mode mixity. The positive-part operator ensures that only tensile stresses drive the damage evolution. The *cohesive strength* $\tilde{\sigma}$ is a reference stress value that corresponds to $y = 1$, and g is a monotonically increasing mapping of $[0, \infty]$ into itself, satisfying $g(0) = 0$ and $g(1) = 1$. We take g to be the identity function in our implementation.

For the monotone, nondecreasing function f , we have $f(y) = 0$ for $0 \leq y \leq c_0$. That is, the stationary damage is zero for $\tilde{s}_I \leq \tilde{\sigma}_0 := c_0 \tilde{\sigma}$. Larger values of c_0 correspond to more brittle fracture processes, and for this reason, we call $c_0 : 0 \leq c_0 < 1$ the *brittleness factor*. This parameter is independent of how brittle the stick–slip transition is.

From a mathematical perspective, the function f can exceed unity for $y > 1$ in dynamic settings. However, we require that $f(y) \leq 1$, because the stationary damage function should be bounded by unity if it is physically associated with an area fraction. Furthermore, the requirement, $f(y) = 1$ for $y \geq 1$, ensures the continuity of \dot{D} at $D = 1$ in (4.8). The function f can be expressed as,

$$f(y) = \begin{cases} 0 & 0 < y \leq c_0 \\ \acute{r}(\acute{y}) & c_0 < y \leq 1 \\ 1 & 1 < y \end{cases} \quad (4.13)$$

where $\acute{y} = (y - c_0)/(1 - c_0)$, and \acute{r} is a function that smoothly interpolates between 0 and 1 over the interval $[0, 1]$. Examples of \acute{r} include,

$$\acute{r}(\xi) = \begin{cases} \xi & \text{linear} \\ -2\xi^3 + 3\xi^2 & \text{cubic} \end{cases} \quad (4.14)$$

in which $0 \leq \xi \leq 1$. We always use the cubic form in our SDG implementation, since it generates a \mathcal{C}^1 continuous transition that facilitates the convergence of the Newton-Raphson iterations in our nonlinear solution scheme.

Regularization of the contact area fraction and computation of the stick area fraction

We follow the method presented in 3.2.2 to compute the regularized contact area fraction η and the stick area fraction γ . The regularization of η in (3.36) is expressed in terms of the traces of solution fields within the debonded region. In the context of the present damage model, the debonded region is a mesoscopic zone with area fraction D . Thus, the regularization would appear to require a detailed and difficult computation of the mesoscopic solution to obtain the normal separation and the normal Riemann stresses on the debonded region for use in (3.37) and (3.39). However, according to (4.6), we can use the traces of the macroscopic solution to compute the

normal Riemann stresses without affecting the value obtained from (3.39). In a similar fashion, we can use the trace of the macroscopic solution in (3.25) to determine the stick area fraction γ . On the other hand, the traces of the macroscopic displacement field generally yield a somewhat smaller separation than the average mesoscopic separation on the debonded region, as required in (3.37). Nonetheless, the two separations are correlated, and we deem it acceptable to use the macroscopic separation for purposes of regularization (3.37). Overall, this approach significantly simplifies, and makes tractable, the computation of γ and the regularized η .

4.3 Probabilistic crack growth in brittle solids with random defects

As observed experimentally, cracks nucleate at material defects where reduced material strength or stress concentrations induced by stiffness fluctuations initiate fracture. Crack extension often involves small, post-nucleation cracks joining a main crack, so defects also play an important role in determining the critical conditions for extensions of primary cracks.

Consider, for example, the evolution of material damage leading to crack nucleation in a brittle material, such as PMMA, where void nucleation and growth is the primary mechanism leading to fracture [75, 76]. The material damage process begins at very small scales with the nucleation and growth of microscopic voids. During this stage, the material damage is diffuse and can reasonably be modeled as a bulk damage process. At some point, however, mesoscopic defects, either pre-existing or due to natural variations in the growth and coalescence of microscopic voids, localize the damage process so as to concentrate mesoscopic voids along an incipient fracture surface. This leads to enhanced growth rates as voids begin to interact with their neighbors within an active fracture process zone. Eventually, voids coalesce to form new, fully debonded, fracture surface. When the latter mesoscopic stages of crack formation are sufficiently localized, it may be appropriate to model them with a cohesive interface model.

In this section, we propose a new cohesive model, based on interfacial damage evolution, for the mesoscopic stages of crack nucleation and extension. Mesoscopic material defects, with a random distribution of resistance

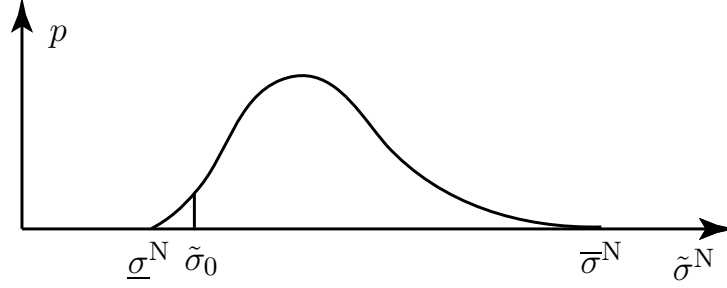


Figure 4.2: Probability density function for nucleation strength at defects.

to mesoscopic void formation (*i.e.*, strength), govern the nucleation and extension of cohesive surfaces, and a damage evolution model describes the subsequent growth of the debonded area fraction on the cohesive surface. Although the present model does not address diffuse void growth in the bulk material, it appears to be worthwhile to do so in extensions of this work.

4.3.1 Nucleation criterion for cohesive surfaces

At the macroscopic level, we assume the *spatial density of mesoscopic defects in the virgin material*, ρ^N , to be a known function of macroscopic position. If required, ρ^N could be randomized as well, but we do not pursue this option here. For simplicity, we take ρ^N to be uniform. We define the *nucleation strength of a defect j* , denoted as $\tilde{\sigma}_j^N > 0$, as the maximum effective traction a defect can withstand without nucleating a crack. This strength might depend on the orientation of the nucleated fracture surface, but for simplicity, here we assume an isotropic nucleation strength at each defect.

Let \tilde{s}_θ denote the effective Riemann traction acting at a defect on a surface with orientation θ under bonded conditions. We assume that a cohesive surface nucleates at macroscopic position \mathbf{x} when

$$\tilde{s}_*(\mathbf{x}) := \max_{\theta} \tilde{s}_\theta(\mathbf{x}) > \min_{j: \mathbf{y}_j \in N(\mathbf{x})} \tilde{\sigma}_j^N, \quad (4.15)$$

in which $N(\mathbf{x})$ is a suitable mesoscopic neighborhood of \mathbf{x} , and \mathbf{y}_j is the mesoscopic coordinate of defect j . Nucleation of a cohesive surface does not always signal the immediate onset of damage or an active cohesive process zone; these depend on whether or not $\tilde{s}_* > \tilde{\sigma}_0$.

Any physically reasonable *probability density function* (PDF), p , can be

used to describe the distribution of defect nucleation strengths in $N(\mathbf{x})$. Without loss of generality, we assume p to follow a truncated normal distribution, such that $\tilde{\sigma}^N \in [\underline{\sigma}^N, \bar{\sigma}^N]$, as depicted in figure 4.2. The *cumulative distribution function* (CDF) corresponding to p is given by,

$$P(\sigma) = \int_{-\infty}^{\sigma} p(x) dx = \frac{\frac{1}{s}\phi\left(\frac{\sigma-\mu}{s}\right)}{\Phi\left(\frac{\bar{\sigma}^N-\mu}{s}\right) - \Phi\left(\frac{\underline{\sigma}^N-\mu}{s}\right)}, \quad (4.16)$$

where μ and s are the mean value and the standard deviation of the untruncated normal distribution, and ϕ and Φ are the PDF and CDF for the standard normal distribution,

$$\phi(x) = \frac{1}{\sqrt{2\pi}} e^{-\frac{1}{2}x^2}, \quad (4.17a)$$

$$\Phi(x) = \frac{1}{2} \left[1 + \operatorname{erf}\left(\frac{x}{\sqrt{2}}\right) \right], \quad (4.17b)$$

in which erf is the error function.¹ The untruncated normal distribution that generates the truncated distribution p in (4.16) can be identified by specifying two parameters. For example, we can specify μ and the cumulative probability of $\tilde{\sigma}_0$ from the untruncated normal distribution, $\tilde{P} := \Phi((\tilde{\sigma}_0 - \mu)/s)$. The standard deviation is then obtained from $s = (\tilde{\sigma}_0 - \mu)/\Phi^{-1}(\tilde{P})$.

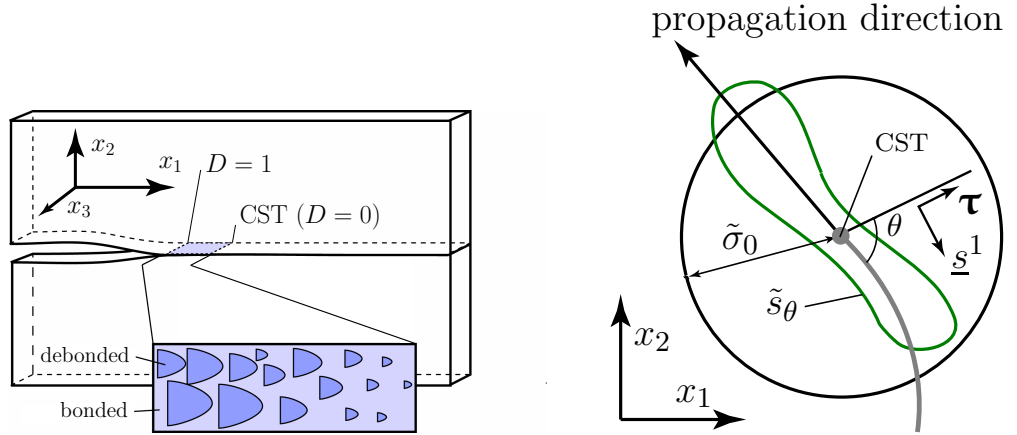
In principle, we can determine whether a cohesive surface nucleates at macroscopic location \mathbf{x} as follows. We evaluate the left-hand side of inequality (4.15) by examining the macroscopic stress state at \mathbf{x} to obtain \tilde{s}_* . Let a denote the spatial measure of $N(\mathbf{x})$. The number of defects in $N(\mathbf{x})$ is then

$$n = \rho^N a. \quad (4.18)$$

We invoke a random number generator tuned to the truncated normal distribution function p in (4.16) to generate a probabilistic set of defect nucleation strengths, $\{\tilde{\sigma}_j^N\}_{j=1}^n$. It is then straightforward to evaluate directly the right-hand side of (4.15) to determine whether the nucleation criterion is satisfied.

The probabilistic treatment of defect strength is a critical feature of this model. If, for example, we treated $\tilde{\sigma}^N$ as a continuous field, there would

¹The mean value μ should not be confused with the Lamé parameter μ that describes the elastic constitutive tensor. We follow standard notation, despite the conflict, since the context should make clear which meaning is intended.



(a) Cohesive process zone and the crack propagation mechanism. The *cohesive surface tip* (CST) is the leading edge of the cohesive process zone where interfacial damage begins to accumulate from $D = 0$ until complete damage, $D = 1$, is attained at the trailing edge of the process zone.

(b) The circumferential distribution of effective stress and crack propagation criterion.

Figure 4.3: The crack propagation criterion.

be an infinite number of nucleation sites in the vicinity of any point where $\tilde{s}_* > \tilde{\sigma}^N$. Not only would this condition prove computationally intractable, but the continuous, deterministic model would also fail to capture an essential feature of real material response. That is, it is the extraordinary, low-strength defects that govern the nucleation of fractures.

In practice, the measure of $N(\mathbf{x})$ is not well defined, and even if it were, the resulting value of n obtained from (4.18) with realistic values of ρ^N might be too large for practical computations. We introduce numerical approximations that address these issues in 4.4.2.

4.3.2 Cohesive surface propagation criterion

Figure 4.3(a) illustrates an active, fully developed fracture process zone in the continuum version of our interfacial-damage cohesive model. The *cohesive surface tip* (CST) corresponds to the leading edge of the cohesive process zone where interfacial damage begins to accumulate; that is, where $D = 0$ and $\tilde{s}_* = \tilde{\sigma}_0$ (cf. 4.2.2). The debonded area fraction D increases along the active process zone until it reaches unity at the trailing edge of the process zone, where complete separation is attained. The material ahead of the CST

is fully bonded and is not part of the cohesive surface. However, the CST might extend into this region to maintain the condition associated with the onset of damage, $\tilde{s}_* = \tilde{\sigma}_0$, under the assumption that the existing crack-tip field provides sufficient mesoscopic conditions to create new cohesive surface. That is, we need not refer to the nucleation condition for undamaged material (4.15) to extend an existing cohesive surface.

It is worth noting that the nucleation of a cohesive surface need not lead immediately to cohesive damage and extension of the cohesive surface. In particular, when nucleation occurs at a defect j where $\tilde{\sigma}_j^N < \tilde{\sigma}_0$, there will be no damage and no active process zone until, and only if, \tilde{s}_* exceeds $\tilde{\sigma}_0$. After that point, the cohesive surface begins to extend as the CST moves into new material, leaving an active process zone in its wake. During this initiation phase, there will only be partial damage, $0 < D < 1$, on the cohesive surface. Additional time is required to attain a fully-developed process zone, whose trailing edge moves to maintain the fully-damaged condition, $D = 1$, as depicted in 4.3(a). Overall, a CST can represent the propagating tip of an existing crack or simply a locus that might or might not develop into a cohesive surface of finite extent at some future time.

We must also determine the direction of extension for the cohesive surface. Figure 4.3(b) shows the normal and tangential tractions, \underline{s}^1 and $\boldsymbol{\tau}$, in the local system for a candidate crack-extension direction θ measured relative to the tangent plane of the cohesive surface at the CST. In addition, magnitudes of the orientation-dependent effective stress \tilde{s}_θ and the uniform value $\tilde{\sigma}_0$ are plotted against θ as radial distance from the CST. We assume that the cohesive surface extends when $\tilde{s}_* > \tilde{\sigma}_0$ in a direction θ where \tilde{s}_θ is a local maximum with respect to θ , subject to $\pi/2 < \theta < 3\pi/2$. The constraint on θ ensures that the crack propagates in a forward direction.

In general, a CST can nucleate at, or extend into, any location in the closure of the spatial domain, including the domain boundary and the surfaces of existing cracks. It can not extend into the domain exterior, and therefore, cannot extend across an existing crack. However, the intersection of the CST of a first crack with one side of a second fracture can trigger the nucleation of a new crack on the opposite side. In this way, our model can give the appearance of a single crack propagating across another, even though the two segments are modeled as distinct cracks.

4.4 Spacetime discontinuous Galerkin discretization and implementation

This section presents the discrete, spacetime discontinuous Galerkin formulation and implementation of the elastodynamic model, including contact and the delay-damage cohesive model. First, we use the weighted residual form to derive macroscopic target fluxes consistent with the mesoscopic bonded, separation and contact modes. Then we adapt an SDG method for conservation laws to model damage evolution on the cohesive interface. In combination, these elements comprise a new coupled model for elastodynamic fracture with contact and cohesive damage evolution. In the latter part of this section, we describe adaptive spacetime meshing procedures that support solution-dependent nucleation and propagation of cohesive surfaces. These procedures allow fractures to develop freely without imposing any mesh-based constraints on the developing crack geometry; they retain the high-order accuracy, efficiency and scalability of the underlying SDG scheme.

4.4.1 Discretization

The basic implementation of the SDG method is similar to that described in section 3.3.2. We show that the break down of boundary integrals on $\tilde{\Gamma}$ results in the same form of macroscopic values in (4.4.1). Furthermore, we extend the implementation of section 3.3.2 by introducing a weak form for integration of the damage field on $\tilde{\Gamma}$ and incorporation of the probabilistic fracture model within our SDG framework.

Evaluation of mesoscopic boundary integrals

When evaluating the weighted residual form (3.41), we must account for the distinct mesoscopic response modes on the cohesive part of the boundary, *i.e.*, in the integrals on $\partial\mathcal{Q} \cap \tilde{\Gamma}$. The term involving the displacement jump is identically zero, since $\star dt|_{\tilde{\Gamma}} = 0$. Noting that $\tilde{\Gamma} = \cup_{\kappa \in \mathcal{R}} \tilde{\Gamma}_{\kappa}$, in which $\tilde{\Gamma}_{\kappa}$ refers to the part of $\tilde{\Gamma}$ in mode κ with area fraction a_{κ} , and recalling (3.5) and (4.4), we write

$$\begin{aligned}
& \sum_{\kappa \in \mathcal{R}} \int_{\partial \mathcal{Q} \cap \tilde{\Gamma}_\kappa} \mathbf{i} \hat{\boldsymbol{\varepsilon}} \wedge (\mathbf{M}_\kappa^* - \mathbf{M}_\kappa) + (\boldsymbol{\varepsilon}_\kappa^* - \boldsymbol{\varepsilon}_\kappa) \wedge \mathbf{i} \hat{\mathbf{M}} \\
&= a_\kappa \int_{\partial \mathcal{Q} \cap \tilde{\Gamma}} \mathbf{i} \hat{\boldsymbol{\varepsilon}} \wedge (\mathbf{M}_\kappa^* - \mathbf{M}_\kappa) + (\boldsymbol{\varepsilon}_\kappa^* - \boldsymbol{\varepsilon}_\kappa) \wedge \mathbf{i} \hat{\mathbf{M}} \\
&= \int_{\partial \mathcal{Q} \cap \tilde{\Gamma}} \mathbf{i} \hat{\boldsymbol{\varepsilon}} \wedge [(a_\kappa \mathbf{M}_\kappa^*) - (a_\kappa \mathbf{M}_\kappa)] + [(a_\kappa \boldsymbol{\varepsilon}_\kappa^*) - (a_\kappa \boldsymbol{\varepsilon}_\kappa)] \wedge \mathbf{i} \hat{\mathbf{M}} \\
&= \int_{\partial \mathcal{Q} \cap \tilde{\Gamma}} \mathbf{i} \hat{\boldsymbol{\varepsilon}} \wedge (\mathbf{M}^* - \mathbf{M}) + (\boldsymbol{\varepsilon}^* - \boldsymbol{\varepsilon}) \wedge \mathbf{i} \hat{\mathbf{M}}, \tag{4.19}
\end{aligned}$$

in which the *macroscopic target fluxes* are defined by $\mathbf{M}^* := a_\kappa \mathbf{M}_\kappa^*$ and $\boldsymbol{\varepsilon}^* := a_\kappa \boldsymbol{\varepsilon}_\kappa^*$, and where the summation convention on κ applies. Thus, the mesoscopic weighted residual statement combined with (3.5) and (4.4) implies that the macroscopic target fluxes are the area-weighted averages of the mesoscopic target fluxes, \mathbf{M}_κ^* and $\boldsymbol{\varepsilon}_\kappa^*$. Furthermore, the mesoscopic target fluxes for bonded, separation and all contact modes can be directly computed from the traces of the macroscopic solution, as shown in (4.6). Thus, we can fully define and solve the macroscopic problem without explicitly solving the mesoscopic problem. This feature provides obvious computational efficiency.

The restrictions of \mathbf{M} and $\boldsymbol{\varepsilon}$ on the vertical interface $\tilde{\Gamma}$ reduce to $\boldsymbol{\sigma}$ and \mathbf{v} , respectively, and similarly for the macroscopic and modal mesoscopic target fluxes. Thus, the expressions for the macroscopic target fluxes simplify to

$$\boldsymbol{\sigma}^* = a_\kappa \boldsymbol{\sigma}_\kappa^*, \tag{4.20a}$$

$$\mathbf{v}^* = a_\kappa \mathbf{v}_\kappa^*. \tag{4.20b}$$

That is, the macroscopic target values for stress and velocity are simply the area-weighted averages of the corresponding mesoscopic target values, and these can be computed directly from the macroscopic solution without solving a mesoscale problem.

Spacetime discontinuous Galerkin method for damage evolution

The damage parameter D evolves according to (4.7) on the vertical d -manifold $\tilde{\Gamma}$, which takes the form of a conservation law with source term on $\tilde{\Gamma}$. As shown below, it is a degenerate example of a conservation law in that the spatial component of the spacetime damage flux vanishes. Thus, the SDG

formulation for conservation laws advanced in [105, 106] is directly applicable, provided that we properly identify the standard bases for forms in $T^*\tilde{\Gamma}$. For this purpose, we define at any $\mathbf{x} \in \tilde{\Gamma}$ a local frame, $\{\underline{e}^i, \underline{e}^t\}_{i=1}^d : \underline{e}^1 \perp T^*\tilde{\Gamma}|_{\mathbb{E}^d}$, with local coordinates $\{\underline{x}_i, t\}_{i=1}^d$. The standard basis for 1-forms on $\tilde{\Gamma}$ in the local frame is $\{d\underline{x}^2, \dots, d\underline{x}^d, dt\}$. The top form on $\tilde{\Gamma}$ is the d -form given by $\underline{\Omega} := \star d\underline{x}^1$. We also have the temporal insertion, $\mathbf{i}\underline{\Omega} = \star dt$, where \star is the Hodge star operator defined on $\tilde{\Gamma}$.

Now we rewrite (4.7) using forms notation. The *spacetime damage flux* is the $(d-1)$ -form, $\mathbf{D} := D\mathbf{i}\underline{\Omega}$, which has no spatial component. Its exterior derivative is simply, $d\mathbf{D} = \dot{D}\underline{\Omega}$. The *damage source term* is the required damage rate, a d -form given by $\mathbf{S} = D'\underline{\Omega}$. We also define the *target damage flux* as $\mathbf{D}^* := D^*\mathbf{i}\underline{\Omega}$, a $(d-1)$ -form in which the scalar coefficient D^* is always the earlier damage value. That is, the target damage flux \mathbf{D}^* is the interior trace of \mathbf{D} on time-outflow boundaries and the exterior trace of \mathbf{D} on time-inflow boundaries, where the exterior trace is obtained from either the outflow solution for \mathbf{D} of an adjacent, previously solved element or from initial data for \mathbf{D} on $\partial\tilde{\Gamma}^{\text{ti}}$. The possibility of nucleation and propagation of cohesive surfaces implies that parts of $\partial\tilde{\Gamma}^{\text{ti}}$ may occur at any time in the analysis interval, so that $\partial\tilde{\Gamma}^{\text{ti}}$ is not restricted to the initial time. Typically, we specify homogeneous initial data for \mathbf{D} everywhere on $\partial\tilde{\Gamma}^{\text{ti}}$.

We rewrite (4.7) in residual form, including its jump part, as

$$d\mathbf{D} - \mathbf{S} = \mathbf{0} \quad \text{on } \tilde{\mathcal{Q}} \quad (4.21a)$$

$$\mathbf{D}^* - \mathbf{D}|_{\partial\tilde{\mathcal{Q}}} = \mathbf{0} \quad (4.21b)$$

for all subdomains $\tilde{\mathcal{Q}} \subset \tilde{\Gamma}$. Overall, the definitions of \mathbf{D} and \mathbf{D}^* ensure that (4.21b) is satisfied trivially on the entire time-outflow boundary, $\partial\tilde{\mathcal{Q}}^{\text{to}}$.

The spacetime finite element partition, $\mathcal{P}(\mathcal{D}) = \{\mathcal{Q}_\alpha\}_{\alpha=1}^N$ on \mathcal{D} , induces a partition on $\tilde{\Gamma}$, $\tilde{\mathcal{P}}_1(\tilde{\Gamma}) = \{\tilde{\mathcal{Q}}_\alpha\}_{\alpha=1}^N$, in which $\tilde{\mathcal{Q}}_\alpha := \partial\mathcal{Q}_\alpha \cap \tilde{\Gamma}$ is empty unless \mathcal{Q}_α is adjacent to $\tilde{\Gamma}$. The non-empty members of $\tilde{\mathcal{P}}_1(\tilde{\Gamma})$ comprise a suitable spacetime finite element mesh for solving the damage evolution equation on $\tilde{\Gamma}$. We denote this reduced set as $\tilde{\mathcal{P}}(\tilde{\Gamma}) := \{\tilde{\mathcal{Q}} \in \tilde{\mathcal{P}}_1(\tilde{\Gamma}) : \tilde{\mathcal{Q}} \neq \emptyset\}$. We define a broken Sobolev space on $\tilde{\mathcal{P}}, \tilde{\mathcal{V}} := \{w \in L^2(\tilde{\Gamma}) : w|_{\tilde{\mathcal{Q}}} \in H^1(\tilde{\mathcal{Q}}) \forall \tilde{\mathcal{Q}} \in \tilde{\mathcal{P}}(\tilde{\Gamma})\}$, in which $L^2(\tilde{\Gamma})$ and $H^1(\tilde{\mathcal{Q}})$ are, respectively, the Hilbertian Sobolev spaces of order 0 on $\tilde{\Gamma}$ and order 1 on $\tilde{\mathcal{Q}}$. For purposes of discretization, we define

the finite dimensional subspace, $\tilde{\mathcal{V}}_h = \left\{ w \in \tilde{\mathcal{V}} : w|_{\tilde{\mathcal{Q}}} \in \tilde{\mathcal{V}}_h^{\tilde{\mathcal{Q}}} \forall \tilde{\mathcal{Q}} \in \tilde{\mathcal{P}}(\tilde{\Gamma}) \right\}$, in which $\tilde{\mathcal{V}}_h^{\tilde{\mathcal{Q}}} = P^{k_{\tilde{\mathcal{Q}}}}(\tilde{\mathcal{Q}})$, where $P^k(\mathcal{Q})$ is the space of polynomials of order k on \mathcal{Q} , and $k_{\tilde{\mathcal{Q}}}$ is the polynomial order assigned to element $\tilde{\mathcal{Q}}$.

We generate a discrete SDG weighted residuals statement for damage evolution by restricting to $\tilde{\mathcal{V}}_h$ both the damage coefficient D and its corresponding weighting function \hat{D} and by weakly enforcing the diffuse and jump parts of (4.7). We obtain,

Problem 3 (SDG method for damage evolution on $\tilde{\Gamma}$) Find $D \in \tilde{\mathcal{V}}_h$ such that for all $\tilde{\mathcal{Q}} \in \tilde{\mathcal{P}}(\tilde{\Gamma})$,

$$\int_{\tilde{\mathcal{Q}}} \hat{D}(\mathbf{dD} - \mathbf{S}) + \int_{\partial\tilde{\mathcal{Q}}} \hat{D}(\mathbf{D}^* - \mathbf{D}) = 0 \quad \forall \hat{D} \in \tilde{\mathcal{V}}_h. \quad (4.22)$$

We obtain a coupled SDG method for elastodynamics and damage evolution by combining (3.41) and (4.22) in a single weighted residuals statement defined over $\mathcal{V}_h \times \tilde{\mathcal{V}}_h$, in which we use the above relations for the macroscopic target fluxes on $\partial\tilde{\mathcal{Q}} \cap \tilde{\Gamma}$.

4.4.2 Adaptive meshing techniques for nucleation and propagation of cohesive surfaces

In this section we present an implementation of the probabilistic theory of crack nucleation and propagation of section 4.3. The nucleation and propagation operations are performed by modifying the front. The cohesive surface tips and crack nucleation points are a subset of the vertices on the space mesh in the discrete setting. Since a vertex advances in time only through pitching a tent on that vertex, the examination of crack nucleation and propagation criteria is restricted to the tent pole vertices.

The examination of nucleation and propagation criteria requires the computation of effective stress for all possible angles as described in section 4.3. The distribution of the effective traction may suffer jumps across element boundaries due to the weak enforcement of continuity conditions in the SDG formulation. The effective traction distribution can be computed for all time $\underline{t} \leq t \leq \bar{t}$, where \underline{t} and \bar{t} are the time coordinates corresponding to the bottom and top of the patch tent pole, respectively. Since the discrete solutions are in general less accurate at the corners of the finite elements we compute

the effective stress distribution at an intermediate time value. Spatially, the effective tractions can be computed at a finite distance or at the limiting zero radius from the crack tip. In the numerical results presented in section 4.5 we use $t = (\underline{t} + \bar{t})/2$, and the tractions are computed at 0^+ radius.

We introduce three approximations in our numerical evaluation of the probabilistic nucleation model.

1. We assume that ρ^N is uniform over the spatial region covered by the outflow faces of the patch. This is oftentimes a reasonable assumption for non-graded materials. We take the outflow spatial region as $N(\mathbf{x})$ to determine the area a in (4.18).
2. We assume that \tilde{s}_* is uniform over the outflow spatial region and is governed by the value at the midpoint of the each patch's tent pole. The high level of adaptive mesh refinement used in our simulations tends to limit the error associated with this approximation.
3. When nucleation occurs, we always take the nucleation point as the spatial position of the top of the tent pole. Again, strong mesh refinement and the fact that the nucleation is defined probabilistically tend to limit the impact of this approximation.

Since we cannot sample the true number of defects in a real material sample, we artificially reduce ρ^N to obtain a tractable number of defects in each patch. Ideally, we would simultaneously adjust the truncated PDF p to maintain an accurate approximation of the true probability of nucleation. However, since a method for accurately identifying ρ^N and p for a real material is a non-trivial task, we do not pursue the adjustment of p in this work. Nonetheless, the patch-wise scheme correctly correlates the number of sample points per patch with the local defect density and the outflow area of the patch.

Each space vertex has a flag that denotes whether it is an active CST or not. The CST flag of a vertex is activated if the discrete nucleation criterion is satisfied. The crack nucleation criterion is inspected every time a patch is erected on a vertex that is currently not an active CST. The spatial coordinate of a vertex does not change once it becomes an active CST. This condition holds regardless whether a crack propagates from the vertex or not.

The vertex, however, can be removed from the space mesh by the coarsening operation described in 4.4.2.

Crack propagation

The crack propagation criterion is tested every time a patch is pitched over an active CST vertex, such as A in figure 4.4. Vertex A may be the tip of a propagating crack as in the figure or be a newly nucleated CST. The relation between the crack propagation threshold in the discrete setting, $\tilde{\sigma}_0^d$, and that for the continuum, $\tilde{\sigma}_0$ is discussed later. Following 4.3.2, the crack propagates along the directions that the effective traction is a local maximum larger than $\tilde{\sigma}_0^d$ and the normal traction is tensile. In general, no two crack edges around a common vertex are permitted to have a relative angle smaller than a user-specified tolerance θ_2 in the SDG implementation; otherwise, the acute angle generated may introduce errors in the discrete finite element solution. The occurrence of such instances, other than the aforementioned shielding for the crack propagation, is very infrequent and is limited to cases where one crack collides with another crack on its trailing edges or at its CST.

An active CST will be examined for propagation directions every time the vertex is advanced in time by pitching a tent. Once the propagation criterion yields a nonzero number of propagation directions, the vertex is no longer inspected for crack propagation. The requested crack propagations on the vertex are in turn achieved by manipulations to the space mesh as shown below. The CST flag of the vertex is inactivated after all the requested propagations are achieved.

Figure 4.4(b) illustrates a patch, where the CST vertex A is erected to A' . As demonstrated, the propagation criterion yields one extension direction after the patch is solved. Typically, the propagation angle is not aligned with any of the element boundaries. Herein, propagation direction passes through element e . We manipulate the space mesh in a way that the edge, r , between the two triangles e_1, e_2 connected to the CST is aligned with the propagation direction. There are two approaches to introduce an element boundary along the crack direction.

In figure 4.4(a), the vertex E is inserted on the edge BC such that AE is aligned with the crack direction. Subsequently, the space element is subdivided to elements e_1 and e_2 . This operation is similar to the edge bisection

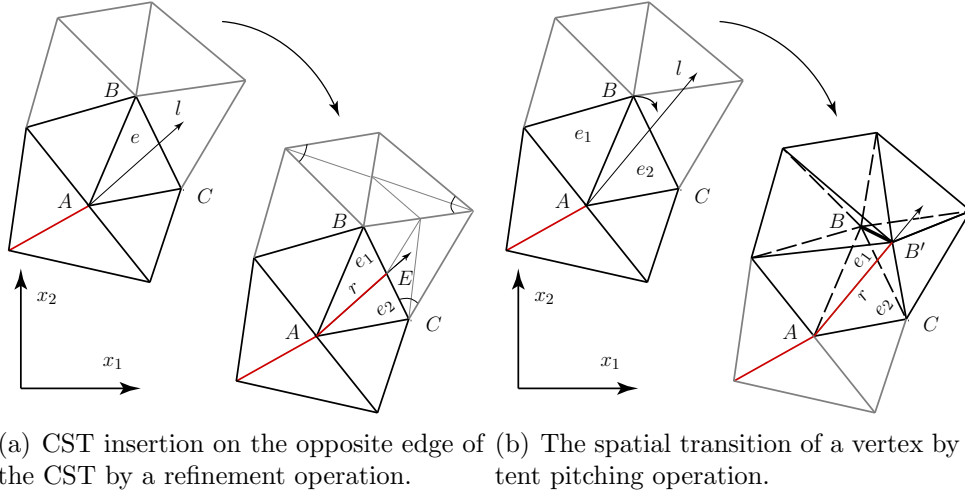


Figure 4.4: The extension of a crack in the space mesh through refinement and tent pitching operations.

procedure [69, 23] employed to refine the element e . The refinement in element e will instigate a series of refinements according to the newest-vertex bisection algorithm [23] on neighboring element in the space mesh to preserve the conformal structure of the space mesh. For example, the chain for refinement is propagated to three elements in the figure.

Figure 4.4(b) shows a situation where the direction of the element boundary AB is close to the requested crack direction, l . We align the edge AB with the crack direction by moving the vertex B to a point on line l . This can be achieved by erecting a tilted tent pole on vertex B such that the top vertex B' lies on line l . If the patch is accepted, we update the front and activate the cohesive flag of the edge AB' . As opposed to previous approach, the propagation direction is not achieved immediately and an intermediate tent pitching is involved. In fact, the move of the vertex B to line l may not be achieved in one step. In many instances the process may take several pitches on vertex B and subsequent tent pole tops; the tent pole top gets closer to the line l each time a patch is erected, until the element edge is aligned with the crack.

When the edge r is aligned with the crack direction in either of the approaches in figure 4.4, the corresponding edge–flag is marked as cohesive and the vertex opposite to vertex A is marked as CST. The CST vertex flag of A is inactivated at this time. Once a patch is pitched on either of the vertices

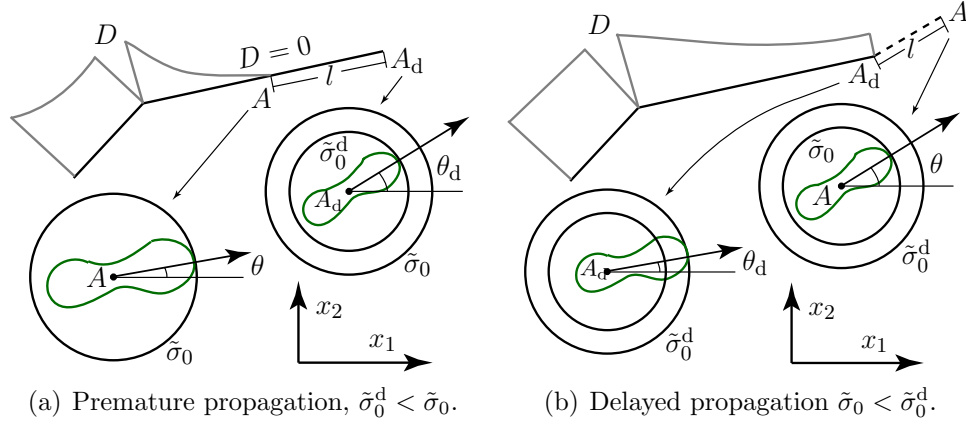


Figure 4.5: The influence of the relative values of $\tilde{\sigma}_0$ and $\tilde{\sigma}_0^d$ on crack propagation pattern.

on the edge r , the tent pole, and consequently all the interior faces of the patch, are going to be vertical to preserve the spatial topology of the crack. The inter-element boundary of the spacetime elements on opposite sides of r , inherits the cohesive flag from the edge r . This vertical cohesive face is augmented to the manifold $\tilde{\Gamma}$ and the damage evolution law is integrated on the face according to (4.22). The initial damage value, D^* is set to zero on the inflow edge r . The crack propagates by discrete finite size extensions on element edges until the CST exits the domain, stops by running into another crack, or is arrested if the propagation criterion does not yield any propagation for all subsequent times.

Discrete crack propagation threshold

Next, we examine the influence of the discrete crack propagation threshold, $\tilde{\sigma}_0^d$ on crack propagation pattern. Figure (4.5) illustrates the exact time, t_d , when the crack propagation criterion, based on $\tilde{\sigma}_0^d$, determines a crack extension at the cohesive surface tip A_d . This implies that the maximum effective traction at vertex A_d is $\tilde{\sigma}_0^d$. The angle corresponding to the maximum value is denoted by θ_d . The damage distribution is depicted alongside the crack edges.

Figure 4.5(a) depicts the case where $\tilde{\sigma}_0^d < \tilde{\sigma}_0$. The distribution of effective traction around A_d is mapped to radial distance relative to the vertex. The vertex A_d experiences effective tractions smaller than $\tilde{\sigma}_0$ from the time the

cohesive face is extended to this vertex. Since $\dot{D} = 0$ for such tractions, the damage, $D = 0$ at A_d . As shown, the physical cohesive surface tip, A (*cf.* figure 4.3(a)), corresponding to the onset of $D = 0$, lags the discrete CST. The crack propagation criterion should be examined on vertex A according to section 4.3.2. Not only the propagation direction, θ , computed at A is different from θ_d , but also the actual cohesive surface tips are apart by the distance l in the figure. The discrepancy grows larger for smaller values of $\tilde{\sigma}_0^d$ and we compute the crack propagation direction on a point that is far ahead of the actual crack tip.

The converse case of $\tilde{\sigma}_0^d > \tilde{\sigma}_0$, is illustrated in figure 4.5(b). The vertex A_d has experienced effective tractions larger than $\tilde{\sigma}_0$ and the damage value D is larger than zero. In fact, the crack should have been propagated at an earlier time $t < t_d$, when the effective traction had exceeded $\tilde{\sigma}_0$ at vertex A_d . That would have generated an extension along the dash line in the figure and at the present time the physical CST would have been at A . In contrary to previous case, the CST lags the physical CST that would have been existed if the crack had been extended at the right time. Herein, the absence of cohesive faces on A_dA prevents the accumulation of damage in the time interval $[t, t_d]$ and introduces an error relative to continuum crack extension. The discrete solution would demonstrate intermittent accumulation of damage along the crack path due to the lag in crack propagation.

Ideally, we want to set $\tilde{\sigma}_0^d = \tilde{\sigma}_0$. However, the calls to crack propagation may experience short delays due to the gradual move of a space vertex toward the requested crack path. Furthermore, the crack propagation criterion is examined on the discrete set of one point per tent pole and the extensions can only be accommodated at the tent pole tops. This is opposed to the continuum setting where the propagation criterion is examined continuously and cracks are propagated immediately. These features can introduce a lag in the discrete setting and we generally use $\tilde{\sigma}_0^d$ values that are slightly smaller than $\tilde{\sigma}_0$ to mitigate such effects (*cf.* figure 4.5).

We should mention that the delay effects are negligible in our adaptive SDG implementation. The number of tent pitching operations needed to achieve a given propagation direction is very limited in practice, due to an optimized use of the two crack propagation schemes in figure 4.4; the immediate insertion of a vertex on the edge BC always has priority and the second approach is only exercised when the crack propagation direction is

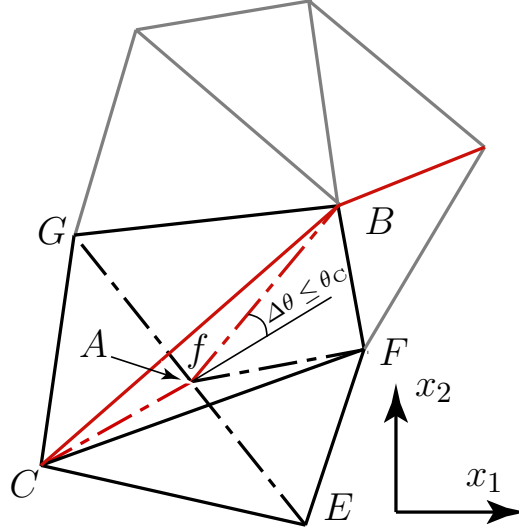


Figure 4.6: The coarsening operation on completely damaged ($D = 1$) edges of a crack.

very close to the existing element boundary directions or the first option is not possible due to some mesh geometry constraints. In addition, due to adaptivity requirements and the complexity of the solution around the cohesive process zone, these elements are typically highly refined and have very short tent poles. Thus, the tent pole tops very accurately model the continuous changes at the CST. In addition, we can ensure that the discrete set of tent poles accurately captures the continuous model by directly controlling the changes from the bottom to top a tent pole through adaptivity criteria.

Coarsening operations along the crack path

The enforcement of the adaptivity error indicators, typically, result in very small element sizes around the CST. The crack propagates in small increments that correspond to the element edges of these elements. This leaves a wake of refinement behind the moving crack tip. This high level of refinement, however, is not necessary when the crack edges are far behind the cohesive process zone and are completely damaged.

The two crack edges AB and AC make a kink angle of $\Delta\theta$ as shown in the figure. As for the coarsening operation, we replace the two edges with the single edge AC . This, not only simplifies the topology of the crack for $\Delta\theta > 0$, but also coarsens the front around the vertex A . A special

coarsening patch removes the vertex A from the front. For example, figure 4.6 depicted a case, where five elements surrounding the vertex A are replaced with three elements CGB , CBF , and CFE on the front after a coarsening patch consisting of the spacetime elements $ACGB$, $ACBF$, and $ACFE$ fills the spacetime region around A .

We discuss the conditions, where the coarsening operation is acceptable in terms of adaptivity tolerances and crack topology constraints. Every time the solution of a patch is accepted, the adaptivity flags of the spacetime elements within the patch are transferred to their corresponding space elements on the front. A vertex, is deemed coarsenable if all the surrounding space elements are marked as coarsenable (for example the five elements surrounding vertex A in the figure). In addition, the discrete implementation (4.22) of the damage evolution law (4.7) introduces adaptivity flags on the cohesive edges of the front such as AB and AC . Similar to full dimensional spacetime elements, the adaptivity flags of cohesive elements on $\tilde{\Gamma}$ is transferred to their corresponding edges on the front. Thus, we require the cohesive edges AB and AC being marked coarsenable in the figure. Furthermore, we introduce additional requirements that are specifically related to the crack propagation. First, the edges AB and AC should be completely damaged to ensure that no coarsening operation occurs in the cohesive process zone. Second, the kink angle $\Delta\theta$ must be smaller than a user-specified tolerance θ_C . Finally, no additional cracks should be connected to the vertex A .

4.5 Numerical results

In this section we present the numerical results based on the material and domain description in the experiments by Sharon and Fineberg [90] and our probabilistic fracture model. Figure 4.7(a) shows the domain description in the experimental work. The experiments were conducted in thin sheets of brittle polymethyl methacrylate (PMMA) with dimensions $L = 200\text{--}400$ mm and $W = 50\text{--}200$ mm and the thickness of either 0.8 mm or 3 mm. Prior to loading, a small “seed” crack was introduced midway between the vertical boundaries. Tensile stress loading \bar{s} was then applied quasistatically until arriving at the sustained values between 10 and 18 MPa.

Figure 4.7(b) shows the computational domain description. We model

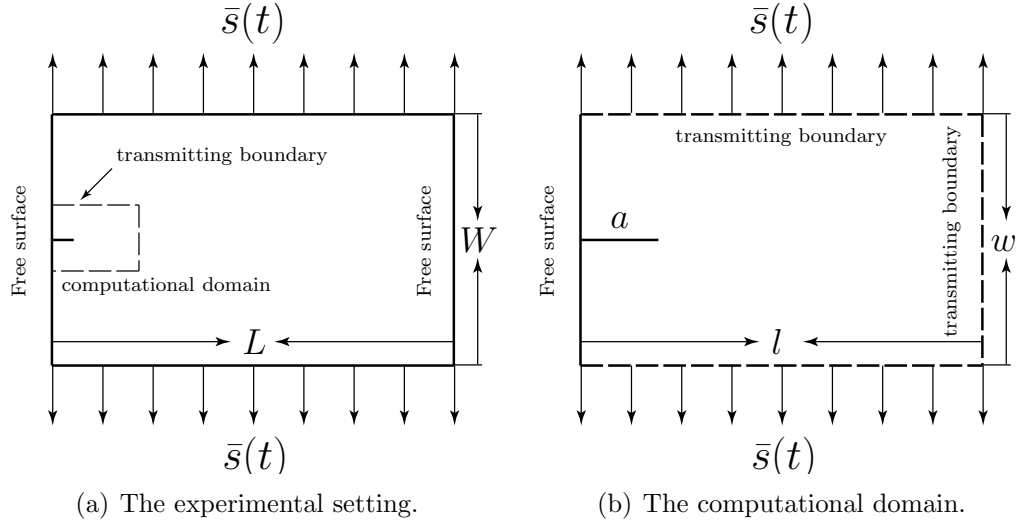


Figure 4.7: Schematic representation of the geometry and boundary condition for the study of crack propagation in PMMA by Sharon and Fineberg [90].

the plate as a two dimensional plane–strain material that approximates the elastic properties of PMMA: Young’s modulus, $E = 3.24$ GPa; Poisson’s ratio, $\nu = 0.35$; and mass density, $\rho = 1190$ kg/m³. For these values of the material parameters, the dilatational wave speed is $c_d = 2090$ m/s. The crack segments are modeled by the damage cohesive model with the cohesive strength, $\tilde{\sigma} = 62.1$ MPa, relaxation time $\tilde{\tau} = 10^{-2}$ μ s, brittleness factor, $c_0 = 0.8$ and $a = 10$ (*cf.* equation (4.10)).

The dimensions of the computational domain are chosen as $l = 16$ mm and $w = 10$ mm. The crack length is given by $a = 2$ mm as in [107, 108]. We assume the stress load \bar{s} to smoothly ramp from zero to the sustained value of 10 MPa over the ramp time $\tau_0 = 2$ μ s. The choice of a relatively large value for τ_0 is because of the quasistatic nature of the applied loads in the experiments and we have $\tau_0 \gg \tilde{\tau}$. The form of the ramp loading is given by the \mathcal{C}^1 -continuous cubic function in (4.14). The stress load is specified as an incoming wave with the characteristic value $\bar{w} = 2\bar{s}$ to model the transmitting boundary condition on the domain boundaries (*cf.* section 3.4.1). The reference time of $t = 0$ is chosen as the instant that the wave fronts reach the mid-crack plane.

We use the probabilistic defect distribution of section 4.3 to simulate the crack propagation in the plate. We choose the spatially uniform density of

$\rho^N = 10^{-7}$ for the defects. The strength distribution of the defects is given by (4.16), where $\mu = 5\tilde{\sigma}$, $\underline{\sigma}^N = 0.4\tilde{\sigma}$, and $\bar{\sigma}^N = \infty$; the choice of $\tilde{P} = 10^{-5}$ results in the standard deviation, $s \approx 0.81\tilde{\sigma}$. For the truncated normal distribution, we have $\mu^N = \mu + 6 \times 10^{-9}\tilde{\sigma}$ and $\tilde{P}^N = 9.4 \times 10^{-8}\tilde{\sigma} \approx \tilde{P}$. The effective traction threshold for crack propagation in the discrete setting is given by $\tilde{\sigma}_0^d = 0.9\tilde{\sigma}_0$, where $\tilde{\sigma}_0 = c_0\tilde{\sigma} = 49.68$ MPa. The angle shield used in the discrete implementation of the crack propagation is taken as $\theta_S = 35^\circ$.

Figure 4.8 illustrates the crack propagation path on the space mesh versus the number of solved patches. As mentioned before, the vertices on the space mesh, generally have distinct time coordinates. However, due to the causal structure of the wave propagation these time values are typically not far apart. The time values reported in the figure correspond to the minimum time coordinate on the front.

The crack propagates rather in a straight line before it branches at approximately 0.37 mm ahead of the initial crack tip at time $t \approx 2.26 \mu\text{s}$. Figure 4.8(a) illustrates the crack path slightly after the branching event. Figures 4.8(b) to 4.9(f) show the propagation of several microcracks off the two main macrocracks. The microcracks run a short distance before they eventually arrest. The microcracks typically do not experience a complete damage and the damage values is specifically small at the crack tips. It appears that the crack propagates in straight lines. However, severe variations in crack path are observed at smaller scales. Finally, we observe that the high gradient solution in the cohesive process zone is accompanied by a fair amount of refinement. Once the CST propagates farther and the crack faces are completely debonded, the coarsening operations simplify the topology of the crack.

Figure 4.9 examines the crack propagation details at smaller scales. For example, we observe different microbranching and side cracking patterns; figures 4.9(a) and 4.9(b) show instances where branching occurs either ahead or to the side of the crack. The branching occurs in a region with finite length in figures 4.10(c) and 4.10(d); specifically the three microbranches in 4.10(d) do not initiate at exactly the same location and they are preceded by two cracks than run in parallel. We also observe an instance where one crack is arrested by running into the side of another crack.

We also observe several instances where the crack follows a zigzag propagation pattern, albeit the overall path might look straight. These small

scale oscillations, which are associated with the surface roughness on the fracture surface, are well documented in the literature. The experimental results in [109] show that the increase to the crack velocity results in larger magnitudes for surface roughness. Sharon and Fineberg [90] observe path oscillations, prior to the occurrence of macroscopic branching. The phenomenological model of Gao [110] shows that the time rate of the dissipated energy at fracture surface is maximized when the crack follows a wavy path. Uenishi and Rossmannith [111] analyze the stability of the crack path in the framework of catastrophe theory. They demonstrate that the stable crack direction at small speeds is followed by a velocity range where there is no clear propagation direction and the path oscillations results in surface roughness before the crack bifurcates at higher velocities. A close examination of figure 4.9 reveals that the magnitude of oscillations increase for the cracks with higher damage levels. In fact, our results show that the cracks with higher path oscillations have faster propagation speeds as well.

The effect of coarsening operations can clearly be seen in figures 4.9(b) to 4.10(d). In each case, we have an instance of a microcrack which is partially damaged and cannot be coarsened. In contrast, we observe that the cracks with complete damage have larger segments as a result of the coarsening operations. In fact, it is the shielding effect of the main crack that prevents the complete accumulation of damage on microcracks. The shielding effect can clearly be seen in 4.9(a) where the microbranch trapped between two other microbranches does not accumulate damage until the surrounding branches are arrested. In addition, we observe that the tip region of all arrested cracks has low damage values.

We conclude this section by briefly discussing the results of the same problem with a new set of parameters. Figures 4.10 to 4.12 show the crack propagation patterns for a model where $\tilde{\tau} = 10^{-3}$, $\rho^N = 10^{-5}$, and other parameters are identical to the previous example. Herein, the macrobranching occurs almost immediately at $t = 1.27 \mu\text{s}$ and 0.04 mm ahead of the initial crack tip position. Compared to previous results, the microcracks and microbranches are denser, propagate longer, and possess higher damage values; the crack appears as an ensemble of microcracks propagating forward rather than the two main microcracks of the previous case. Figure 4.11 shows the details of the crack propagation. We observe that the initiation of the microcracks is less complex in this case. The wavy crack propagation and incomplete

damage at the tip of a microcrack is depicted in 4.11(b). Finally, figure 4.12 illustrates the crack path at $t = 2.05 \mu\text{s}$ on the deformed geometry.

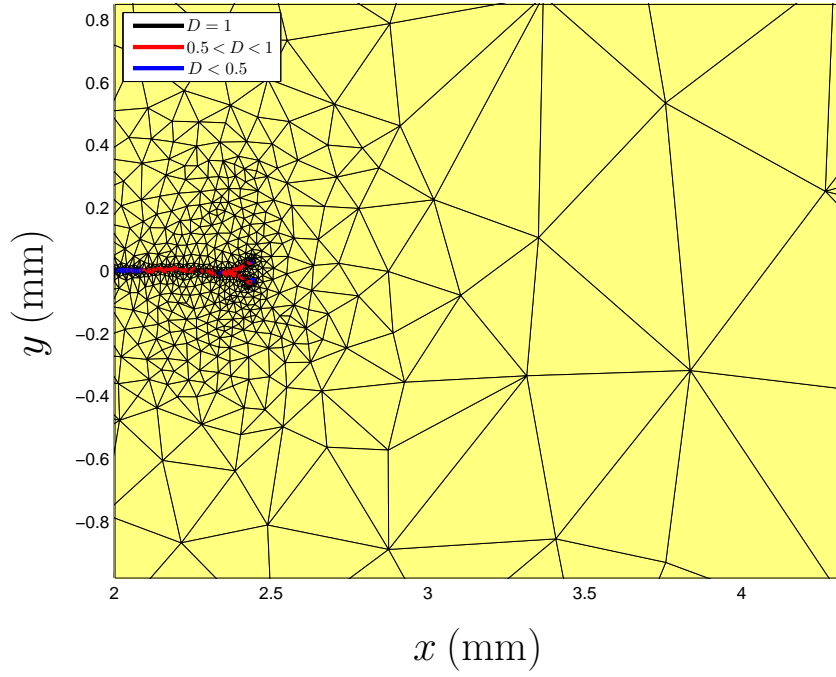
4.6 Conclusions

We have presented the formulation and SDG implementation of a new two-scale cohesive fracture model that represents mesoscale processes of void growth and coalescence. The evolution of a single damage parameter D , which represents the debonded area fraction on cohesive interfaces, is governed by an irreversible, time-delay evolution law characterized by a cohesive strength and a relaxation time τ that determines the maximum damage rate. Riemann fluxes for the fully-bonded condition are enforced in the undamaged area fraction $(1 - D)$ of the cohesive interface, while the Riemann fluxes for the contact–stick, contact–slip or separation conditions determine the fluxes in the debonded area fraction. These mesoscale Riemann values are averaged to derive macroscopic cohesive conditions.

The enforcement of Riemann fluxes, which are the physically and mathematically correct solutions for all contact and separation modes, yields a cohesive model with desirable properties. Unlike intrinsic and most of interfacial damage models, they do not introduce any artificial compliance in the bulk material. The distinct treatment of contact and separation modes at mesoscopic level, eliminates the computational problems associated with the enforcement of impenetration condition via large penalty values in TSR cohesive models. Although the same distinction of modes applies to the interfacial damage models in [88, 89], the use of linear spring relations, instead of the correct bonded Riemann solution, in the bonded area fraction introduces an artificial compliance.

We have presented a model for nucleation and crack propagation in brittle materials. Motivated from experimental observations, we assume that cracks nucleate only from the defects that pre-exist in the material. The spatial and strength distribution of the defects can follow any physically reasonable distribution. Herein, we assume the spatial and strength variations of the defects to follow uniform and truncated normal distributions, respectively. In addition, we adopt a cracks propagation criterion based on the direction of the maximum effective stress.

(a) $N = 6 \times 10^5, t \approx 2.38 \mu s$



(b) $N = 2 \times 10^6, t \approx 2.96 \mu s$

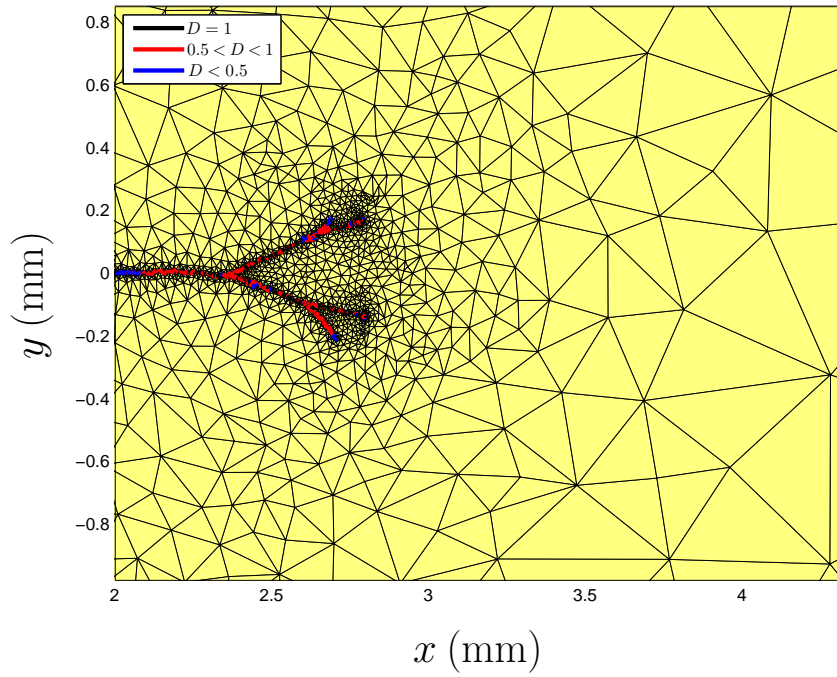
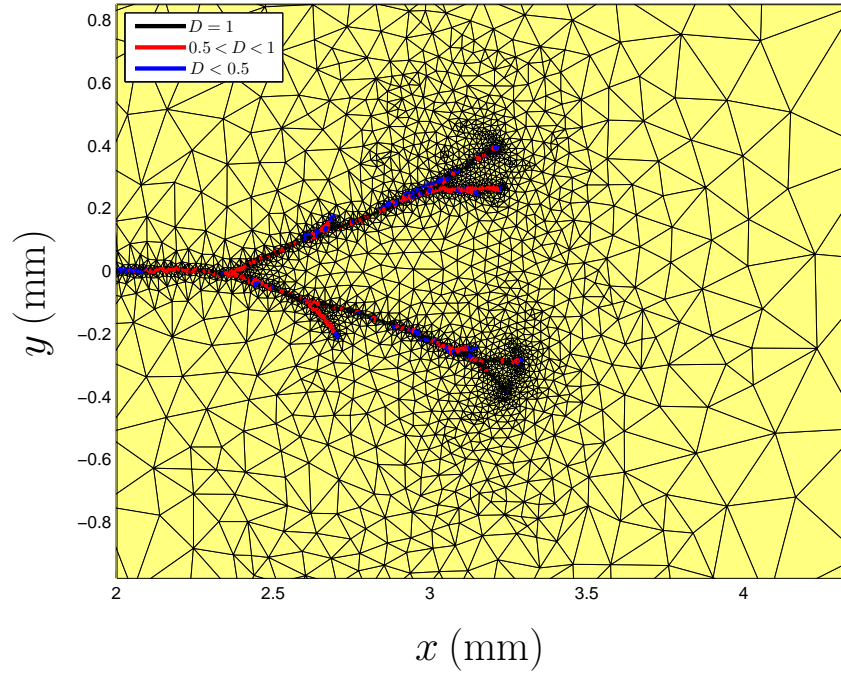


Figure 4.8: Crack propagation on the space mesh versus the number of patches for $\tilde{\tau} = 10^{-2} \mu s$.

(c) $N = 6 \times 10^6, t \approx 3.68 \mu s$



(d) $N = 1.2 \times 10^7, t \approx 4.27 \mu s$

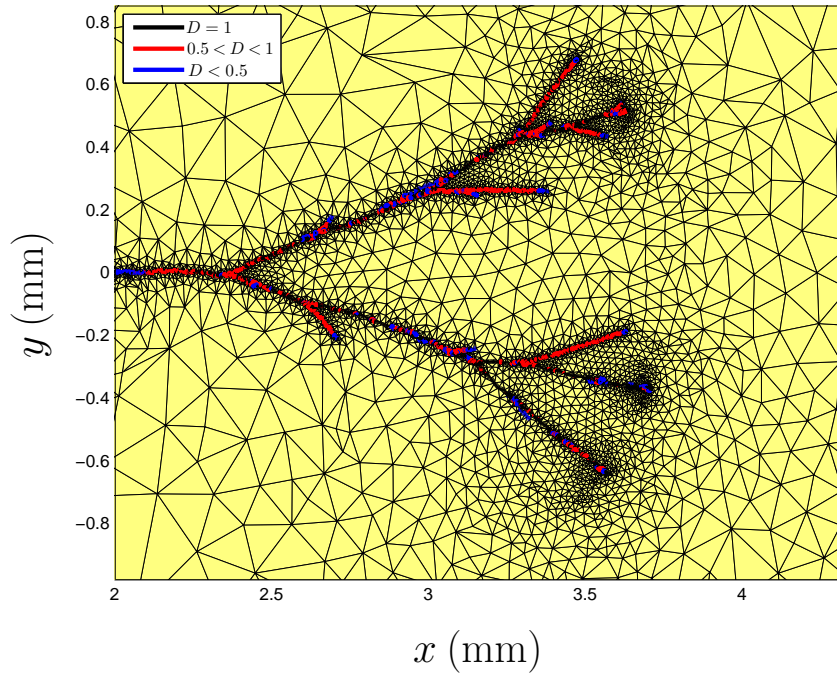
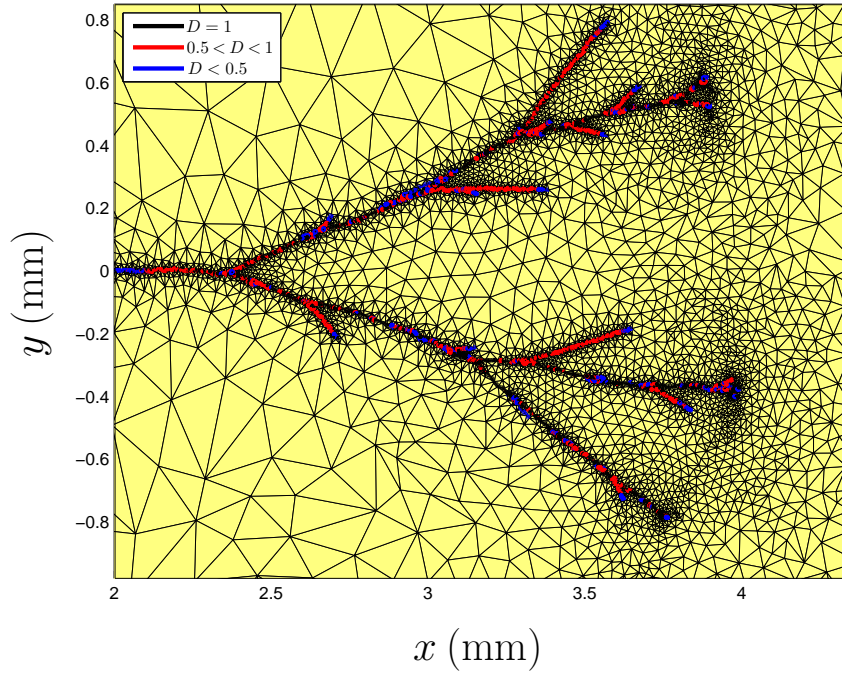


Figure 4.8: (continued) Crack propagation on the space mesh versus the number of patches for $\tilde{\tau} = 10^{-2} \mu s$.

(e) $N = 1.8 \times 10^7, t \approx 4.65 \mu s$



(f) $N = 24 \times 10^7, t \approx 4.96 \mu s$

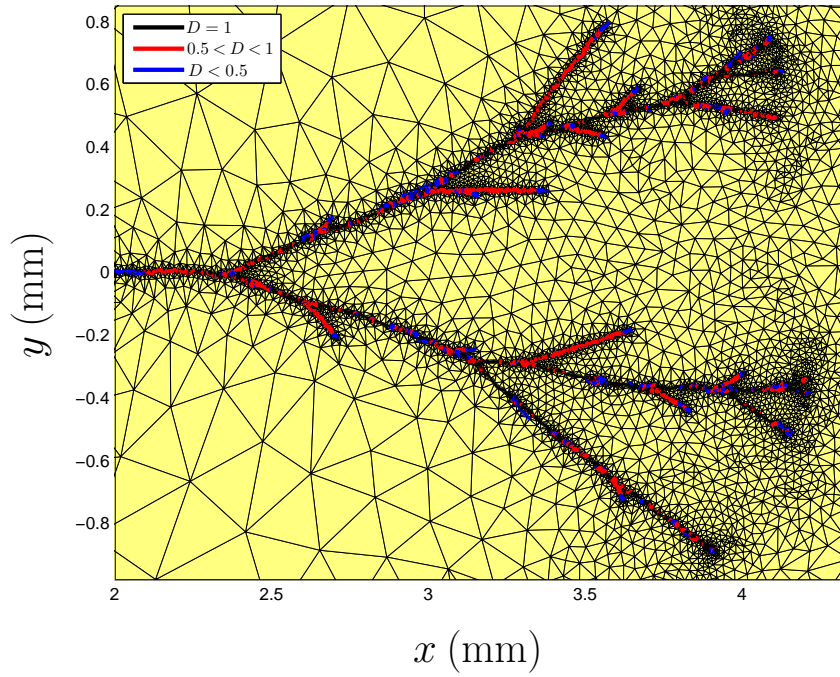
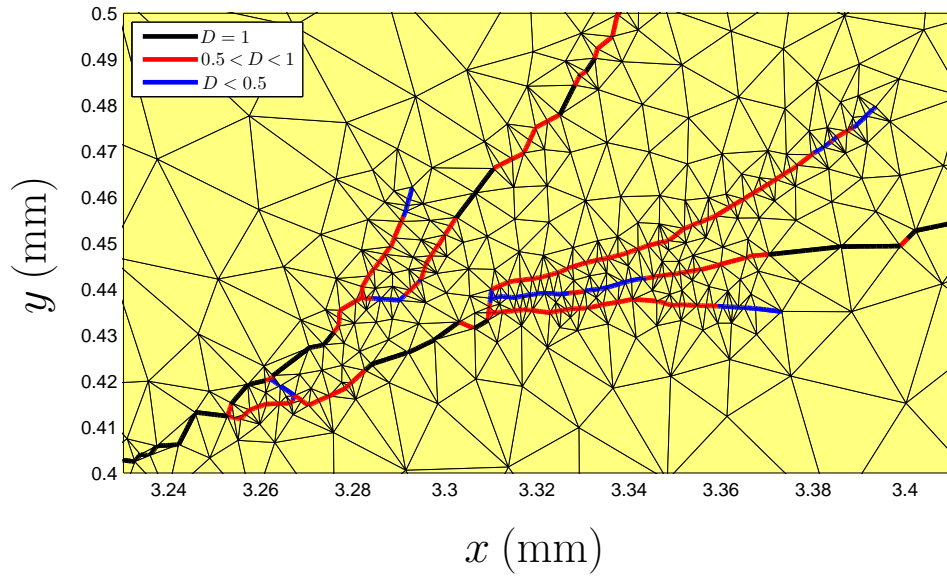
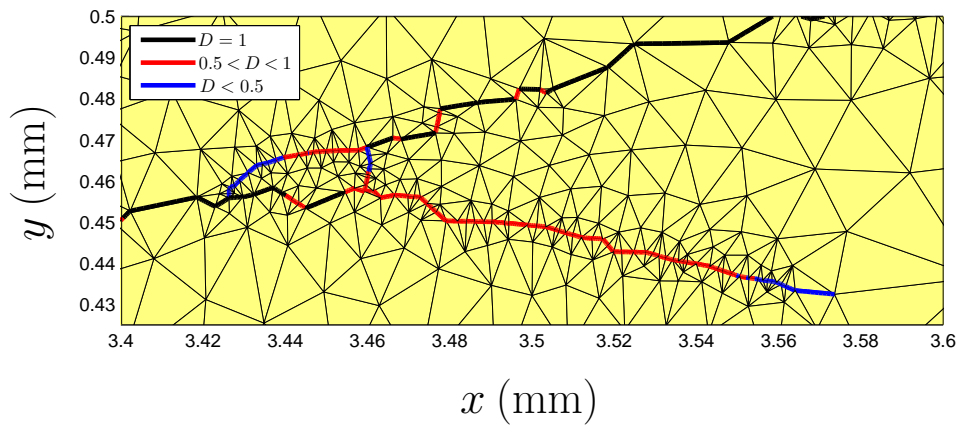


Figure 4.8: (continued) Crack propagation on the space mesh versus the number of patches for $\tilde{\tau} = 10^{-2} \mu s$.

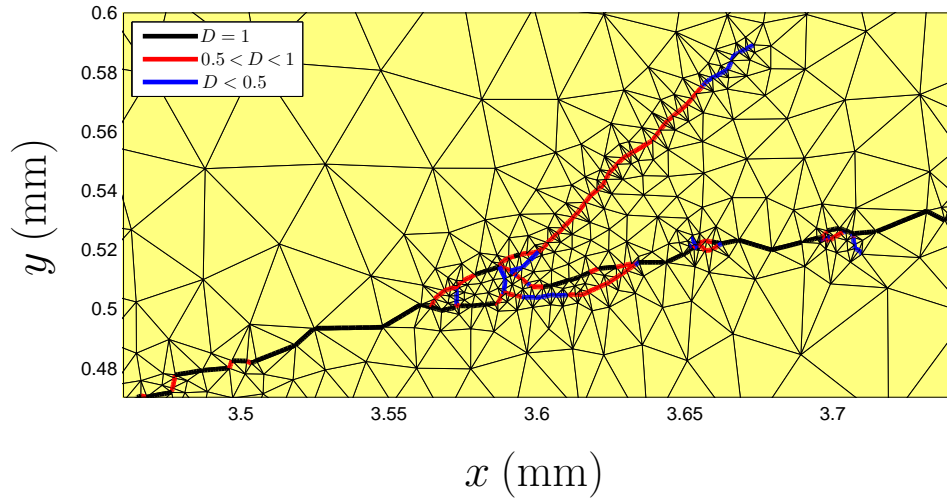


(a) The third microcrack on the top macrobranch.

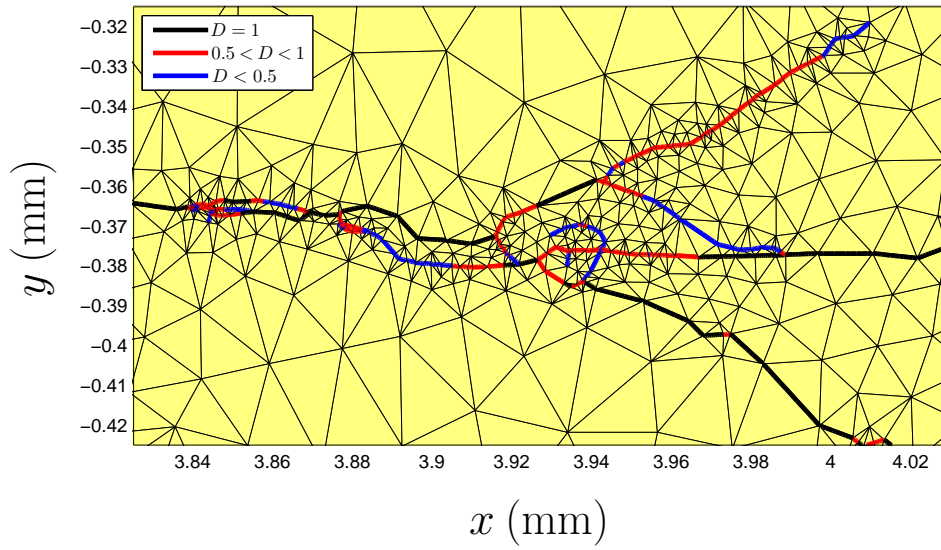


(b) The fourth microcrack on the top macrobranch.

Figure 4.9: The details of the crack path around the microcrack events at $t \approx 4.96 \mu\text{s}$ for $\tilde{\tau} = 10^{-2} \mu\text{s}$.



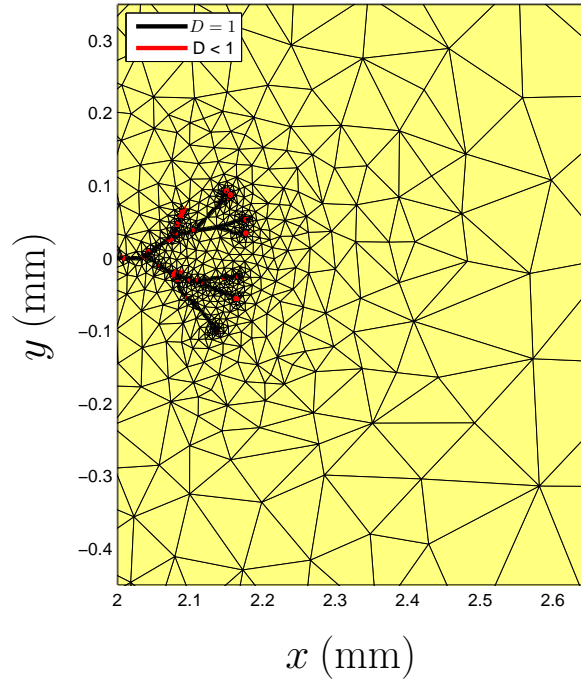
(c) The fifth microcrack on the top macrobranch.



(d) The second microcrack on the bottom macrobranch.

Figure 4.9: (continued) The details of the crack path around the microcrack events at $t \approx 4.96 \mu s$ for $\tilde{\tau} = 10^{-2} \mu s$.

(a) $N = 10^5, t \approx 1.34 \mu s$



(b) $N = 5 \times 10^5, t \approx 1.48 \mu s$

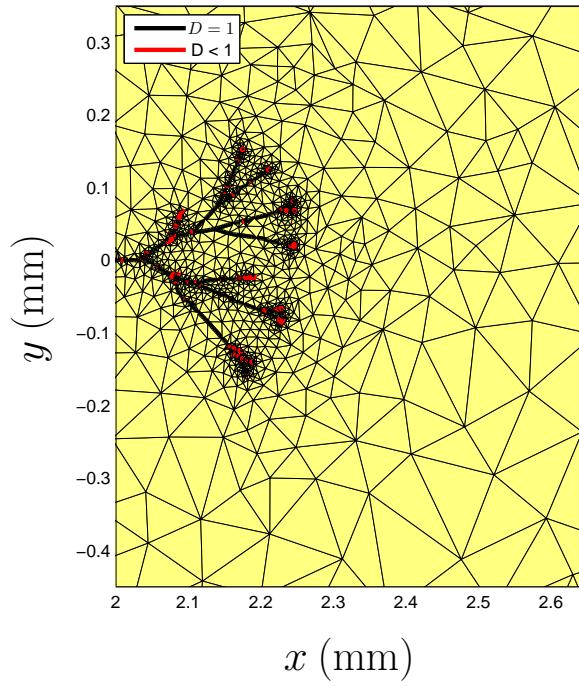
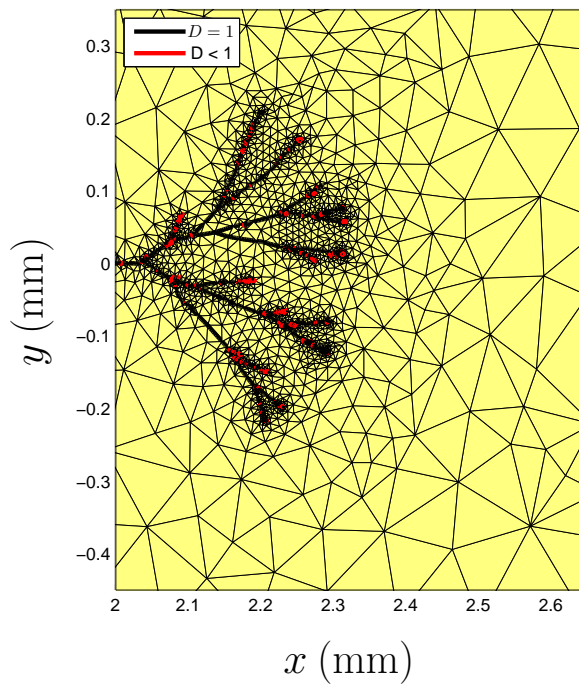


Figure 4.10: The crack propagation on the space mesh versus the number of patches for $\tilde{\tau} = 10^{-3} \mu s$.

(c) $N = 2 \times 10^6, t \approx 1.67 \mu s$



(d) $N = 5 \times 10^6, t \approx 1.85 \mu s$

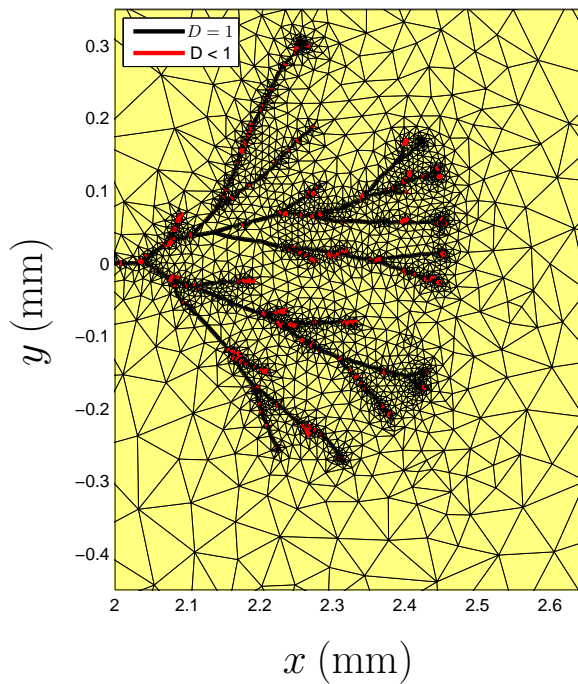
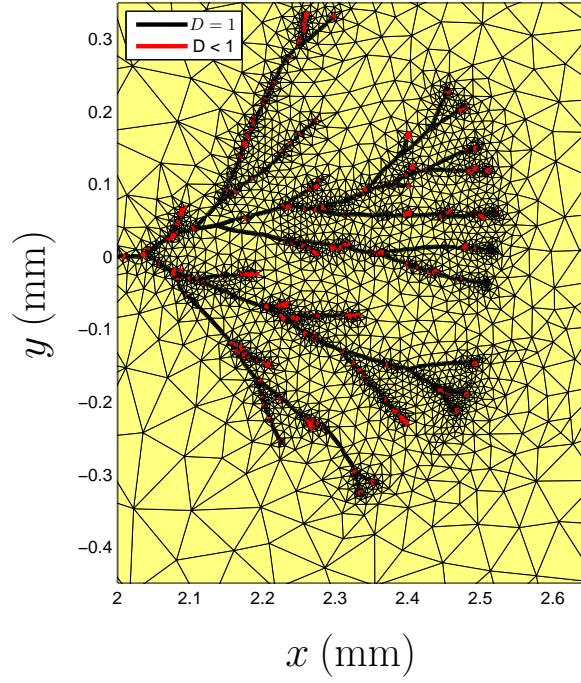


Figure 4.10: (continued) Crack propagation on the space mesh versus the number of patches for $\tilde{\tau} = 10^{-3} \mu s$.

(e) $N = 7 \times 10^6, t \approx 1.94 \mu s$



(f) $N = 10^7, t \approx 2.05 \mu s$

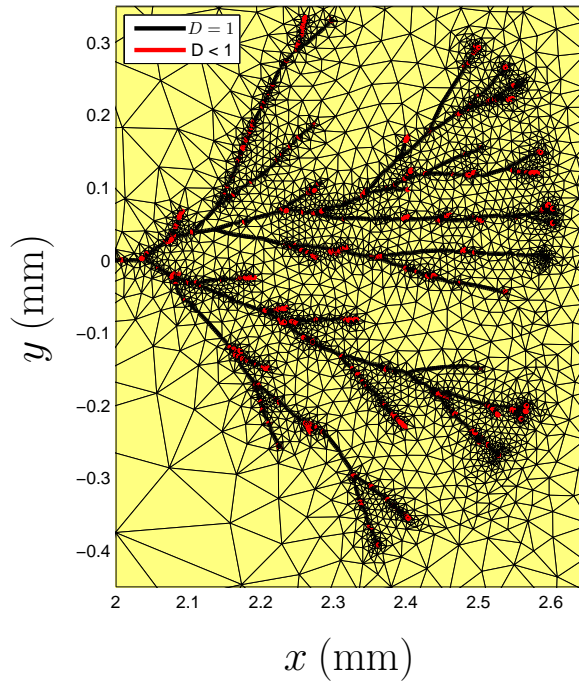
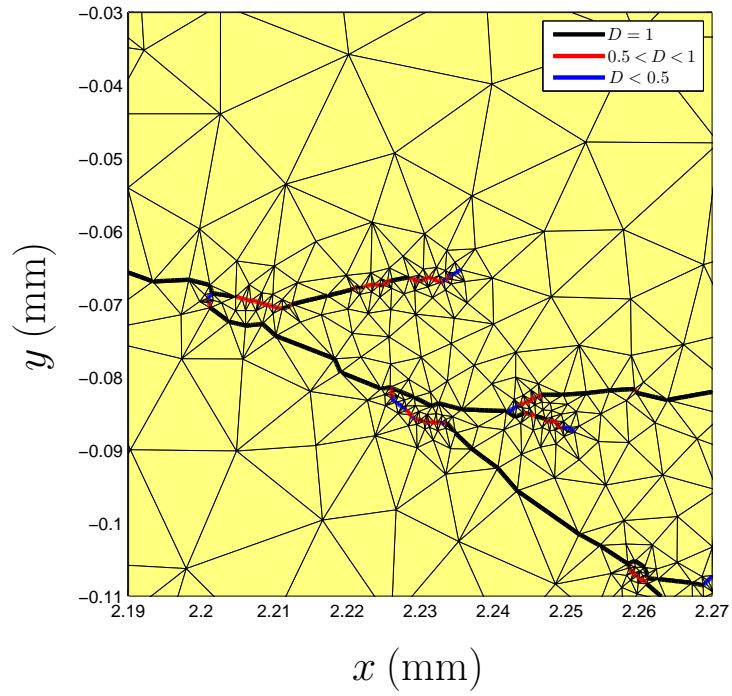
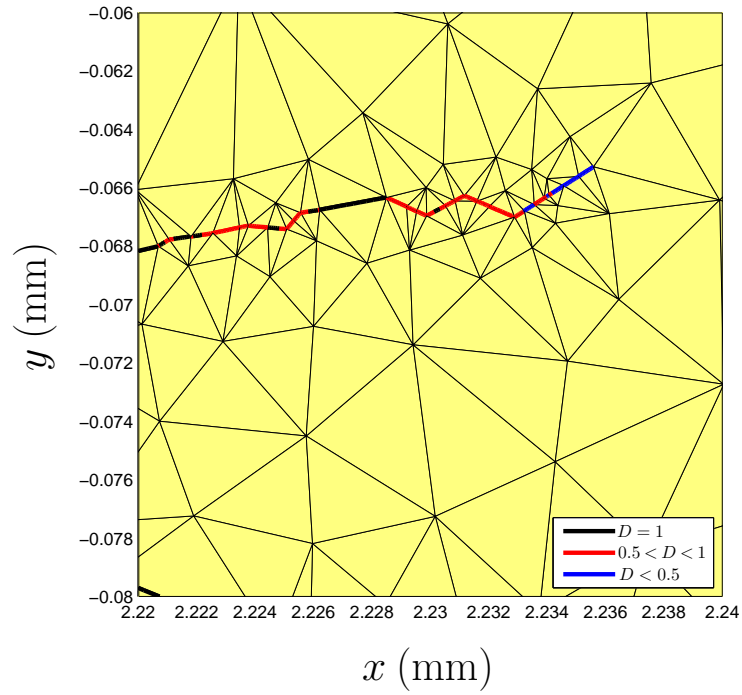


Figure 4.10: (continued) Crack propagation on the space mesh versus the number of patches for $\tilde{\tau} = 10^{-3} \mu s$.



(a) Details on microcrack events.



(b) Wavy crack path.

Figure 4.11: The details of the crack path at $t \approx 2.05 \mu\text{s}$ for $\tilde{\tau} = 10^{-3} \mu\text{s}$.

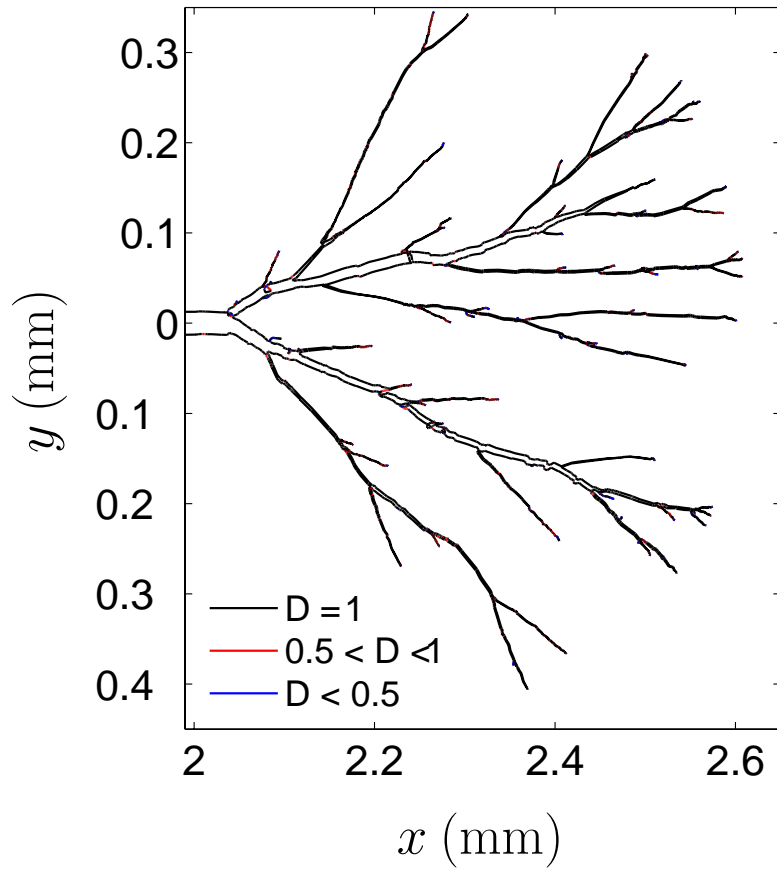


Figure 4.12: Crack path at $t = 2.05 \mu\text{s}$ on deformed geometry for $\tilde{\tau} = 10^{-3} \mu\text{s}$.

These features of the SDG method combined with the element-level balance of momentum, use of Riemann solutions, dual adaptivity error indicators, and linear complexity of the method [12, 13] leads to a very accurate and efficient method for solving dynamic fracture problems.

We simulated the crack propagation in an example based on the experimental work in [90]. Our numerical results demonstrate crack propagation, microcrack and microbranch formation, crack arrest, and crack branching phenomena. It is only the nucleation and crack propagation criteria and the local distribution of mechanical fields that control the crack path. In contrast, many numerical schemes such as [99] use separate criteria for the onset of crack branching, which may not even provide the angles of the new branches. We also observed some interesting physics of the dynamic fracture such as crack shielding and the wavy crack motion that is observed in experiments [109, 90] and predicted with theoretical models [110, 111].

Various extensions can be considered to our formulation and SDG implementation. The simulation of dynamic fracture can easily become intractable; the increasing number of cohesive surface tips, generated by crack branching and microcrack events, may call for parallel simulations, where each cohesive process zone can be solved with the desired accuracy. A parallel implementation, based on the ParFUM and CHARM++ frameworks [112, 113], is under development. The experimental results of [90] and a corresponding numerical simulation [108] demonstrate the existence of a dominant main crack which is absent in our results in section 4.5. We believe that the incorporation of energy dissipative mechanisms in the bulk material such as [114], absorbs some of the energy, that otherwise is diverted to the crack, and will retard the branching events. A more comprehensive understanding of the cohesive and crack nucleation and propagation parameters is of interest. As observed in section 4.5 the choice of such parameters can greatly change the topology of moving cracks.

Chapter 5

Conclusion

We have presented a dimensional analysis for the general initial and boundary value elastodynamic problem using differential forms notation. We consider scalings of both the forms overall and of just the form coefficients. Our analysis within the differential forms notation reveals certain intrinsic relations between the spacetime mechanical fields, which otherwise are obscured by tensorial notation. For example, we find that only four distinct scalings are required to define an elastodynamic process when we work directly with forms, while eight are required when tensor notation is used.

Furthermore, we extend the dimensional analysis to TSR-based cohesive fracture mechanics problem. The solution fields are represented in terms of nondimensional groups which in turn are expressed in terms of cohesive scales. The cohesive length scale, \tilde{L} , determines the scaling of domain dimensions. We also show that cohesive process zone size is proportional to \tilde{L} . The intrinsic cohesive velocity value, \tilde{v} scales all velocity related fields. In addition we obtain an intrinsic time scale, $\tilde{\tau}$, which is of fundamental importance in dynamic fracture.

The LEFM solution can provide an accurate approximation in regions outside the cohesive process zone if the SSY assumption holds. That is, the relative size of this process zone to radii of singularity from LEFM theory is considerably smaller than unity. We show that this ratio, Λ/r , is proportional to $(\check{\sigma}/\tilde{\sigma})^2$ where $\check{\sigma}$ in turn is proportional to the scale of loading. This relation is of utmost importance. On one hand, it quantifies small-scale yielding assumption and determines how LEFM solution loses its accuracy. On the other hand, $\check{\sigma}/\tilde{\sigma}$ is one of the nondimensional parameters associated with TSR models and changes to these parameters can not be described by self-similar solutions.

We only investigated the nondimensional parameters relating the ratio of the loads to cohesive strength in our numerical simulations. In finite

domains the interplay between the domain and cohesive length and time scales changes the dynamic of moving cracks. For example, waves reflected from the domain boundaries and crack tips can appreciably change the crack speed. The study of such nondimensional parameters can be an extension to the current work. Moreover, similar studies can be carried out for other types of fracture models such as the interfacial damage evolution models described in this work. Finally, it is desirable to extend the results on pure modes *I* and *II* to general mixed mode conditions.

We presented a novel formulation of the linear elastodynamic contact problem employing the local Riemann solutions. The Riemann solutions specify the mathematically and physically correct mechanical fluxes on a material interface under different contact modes. The target fluxes are incorporated in a spacetime discontinuous Galerkin implementation of the linear elastodynamic problem. The elastodynamic governing equations yield a diffuse part in the interior of the spacetime elements as well as a jump part on the boundary of the elements. The distinct contact conditions are specified by the weak enforcement of the jump conditions with respect to the Riemann solutions.

Specifically, we obtained the Riemann fluxes for bonded, contact–stick, contact–slip, and separation modes. We should emphasize that the Riemann solutions exactly preserve the characteristic structure of the incoming elastodynamic waves from opposite sides of the interface. The treatment of contact conditions in many numerical methods violates this structure. For example, we demonstrate that the Riemann fluxes are identical for contact–stick and bonded modes. This identification does not hold in penalty methods, where the application of large stiffness values for penetrating displacements replaces the displacement continuity conditions required otherwise. Unlike the Lagrange multiplier method the treatment of contact conditions is localized to the patches that have nonempty intersection with the contact surface. Furthermore, no additional degrees of freedom such as Lagrange multipliers are required in our method.

The contact-slip Riemann solutions can be obtained according to the specific form of the friction law. Herein, we use the Coulomb’s law of friction to derive the Riemann solutions. The direction of the tangential contact traction (friction) is obtained from the slip velocity at the interface, which results in a discontinuous representation of the slip traction at stick/slip

transitions. There have been many attempts to remedy the discontinuous behavior by regularizing the Coulomb friction law as in [66, 67, 65]. This discontinuous behavior is, however, removed in our formulation without any modification to the actual form of the Coulomb law; we demonstrate that the slip velocity is aligned with the tangential traction that would have acted on the interface if the contact-stick condition held. Unlike the slip velocity, the latter does not vanish at stick/slip transitions and does not introduce any discontinuities.

We have presented the formulation and SDG implementation of a new two-scale cohesive fracture model that represents mesoscale processes of void growth and coalescence. At mesoscopic level the interface is divided into bonded, contact-stick, contact-slip, and separation modes. The target values on each mesoscopic area are obtained from the solution to a local Riemann problem. The enforcement of Riemann fluxes, which are the physically and mathematically correct solutions for all contact modes, yields a cohesive model with desirable properties. Unlike intrinsic and most of interfacial damage models, they do not introduce any artificial compliance in the bulk material. The distinct treatment of contact and separation modes at mesoscopic level, eliminates the computational problems associated with the enforcement of impenetration condition via large penalty values in TSR-based cohesive models.

We have presented a model for nucleation and crack propagation in brittle materials. The cohesive surfaces can only nucleate from defects that pre-exist in the material. The spatial and strength distribution of the defects can follow any physically reasonable distribution. Our SDG implementation adaptively aligns the element boundaries with crack-path trajectories that are obtained as a part of the solution according to a crack propagation criterion. Thus, the present model does not suffer the mesh-dependent effects encountered in most other numerical fracture models. Furthermore, no discontinuous features are introduced within the elements as opposed to X-FEM and generalized finite element methods.

A numerical simulation based on the experiments by Sharon and Fineberg [90] reveals microcrack and microbranch formation, crack arrest, and crack branching phenomena. Some other interesting features of the dynamic fracture, observed in experiments, such as crack shielding and wavy crack motion are also evident in our results. In general, the element-level balance of mo-

mentum, use of Riemann solutions, dual adaptivity error indicators, and linear complexity of the method [12, 13] leads to a very accurate and efficient method for solving dynamic fracture and contact problems.

Various extensions to our fracture model can be considered. The damage evolution relation in this work is mainly based on that in [77]. We believe that a detailed examination of the fracture processes between the bonded and debonded regions at microscale provides a more realistic damage evolution relation. The simulation of dynamic fracture can easily become intractable; the increasing number of cohesive surface tips, generated by crack branching and microcrack events, may call for parallel simulations. The main crack branches after a relatively short interval in our simulations. This is different from the persistence of a main crack in the experimental results [90]. We believe that the incorporation of energy dissipative mechanisms in the bulk material such as [114], absorbs some of the energy, that otherwise is diverted to the crack, and retard the branching events.

Author's Biography

Reza Abedi received his B.S. in Civil Engineering and M.S. in Structural Engineering from Sharif University of Technology in 1999 and 2001 respectively. He obtained an M.S. in Mathematics in 2006 from the University of Illinois at Urbana-Champaign. He will continue as a post-doctorate fellow under the supervision of Professor Robert Haber at the University of Illinois at Urbana-Champaign.

References

- [1] S. J. Wilkins and R. A. Schultz. 3d cohesive end-zone model for source scaling of strike-slip interplate earthquakes. *Bulletin of the Seismological Society of America*, 95(6):2232–2258, 2005.
- [2] S. S. Kiyono, K. Yonehara, R. S. Graf, and W. J. Howell. Consideration of mechanical chip crack on fbga packages. pages 193–197, San Diego, CA, United States, 2001.
- [3] A. Pandolfi and M. Ortiz. An efficient adaptive procedure for three-dimensional fragmentation simulations. *Engineering with Computers*, 18:148–159, 2002.
- [4] C. Denoual and F. Hild. A damage model for the dynamic fragmentation of brittle solids. *Computer Methods in Applied Mechanics and Engineering*, 183:247–258, 2000.
- [5] P. H. Geubelle and J. S. Baylor. Impact-induced delamination of composites: a 2d simulation. *Composites Part B*, 29B:589–602, 1998.
- [6] T. C. Gasser and G. A. Holzapfel. A numerical framework to model 3-d fracture in bone tissue with application to failure of the proximal femur. In *Proceedings of the IUTAM Symposium*, pages 199–212, Lyon, France, 2006. Symposium on Discretization Methods for Evolving Discontinuities.
- [7] D. S. Dugdale. Yielding of steel sheets containing slits. *Journal of the Mechanics and Physics of Solids*, 8:100–104, 1960.
- [8] G. I. Barenblatt. The mathematical theory of equilibrium of cracks in brittle fracture. *Advanced Applied Mechanics*, 7:55–129, 1962.
- [9] L. B. Freund. *Dynamic Fracture Mechanics*. Cambridge University Press, Cambridge, UK, 1990.
- [10] G. T. Camacho and M. Ortiz. Computational modelling of impact damage in brittle materials. *International Journal of Solids and Structures*, 33:2899–2938, 1996.

- [11] A. Pandolfi, P. Krysl, and M. Ortiz. Finite element simulations of ring expansion and fragmentation: The capturing of length and time scales through cohesive models of fracture. *International Journal of Fracture*, 95:279–297, 1999.
- [12] Reza Abedi, Robert B. Haber, and Boris Petracovici. A spacetime discontinuous Galerkin method for elastodynamics with element-level balance of linear momentum. *Computer Methods in Applied Mechanics and Engineering*, 195:3247–3273, 2006.
- [13] Reza Abedi, Morgan A. Hawker, Robert B. Haber, and Karel Matouš. An adaptive spacetime discontinuous Galerkin method for cohesive models of elastodynamic fracture. *International Journal for Numerical Methods in Engineering*, 1:1–42, 2009.
- [14] X. P. Xu and Alan Needleman. Numerical simulations of fast crack growth in brittle solids. *Journal of the Mechanics and Physics of Solids*, 42:1397–1434, 1994.
- [15] M. Spivak. *Calculus on Manifolds*. W. A. Benjamin, New York, 1965.
- [16] W. H. Fleming. *Functions of Several Variables*. Addison-Wesley, Reading, Massachusetts, 1964.
- [17] V. I. Arnold. *Mathematical Methods of Classical Mechanics*. Springer, New York, second edition, 1989.
- [18] S. T. Miller, B. Kraczek, R. B. Haber, and D. D. Johnson. Multi-field spacetime discontinuous Galerkin methods for linearized elastodynamics. *Computer Methods in Applied Mechanics and Engineering*, 199:34–47, 2009.
- [19] J.R. Rice. Mathematical analysis in the mechanics of fracture. In H. Liebowitz, editor, *Fracture, an Advanced Treatise*, volume 2, pages 191–311. Academic Press, New York, United States, 1968.
- [20] J.R. Rice. The mechanics of earthquake rupture. In *Physics of the Earths Interior*, Italian Physical Society, pages 555–649. North-Holland Publ. Co.: Amsterdam, 1980.
- [21] H. H. Yu and Z. Suo. Intersonic crack growth on an interface. *Proceedings of the Royal Society of London, Series A (Mathematical, Physical and Engineering Sciences)*, 456(1993):223–46, 2000.
- [22] L.B. Freund. Crack propagation in an elastic solid subjected to general loading - 3. stress wave loading. *Journal of the Mechanics and Physics of Solids*, 21(2):47–61, 1973.

- [23] R. Abedi, R. B. Haber, S. Thite, and J. Erickson. An h -adaptive spacetime-discontinuous Galerkin method for linearized elastodynamics. *Revue Européenne de Mécanique Numérique (European Journal of Computational Mechanics)*, 15(6):619–642, 2006.
- [24] Kyoungsoo Park, Glaucio H. Paulino, and Jeffery R. Roesler. A unified potential-based cohesive model of mixed-mode fracture. *Journal of the Mechanics and Physics of Solids*, 57(6):891 – 908, 2009.
- [25] J.R. Barber and M. Ciavarella. Contact mechanics. *International Journal of Solids and Structures*, 37(1):29 – 43, 2000.
- [26] B. Bhushan. *Principles and Applications of Tribology*. Wiley, New York, 1999.
- [27] Mark Denny. Stick-slip motion: An important example of self-excited oscillation. *European Journal of Physics*, 25(2):311 – 322, 2004.
- [28] P. Wriggers, T. Vu Van, and E. Stein. Finite element formulation of large deformation impact-contact problems with friction. *Computers and Structures*, 37(3):319 – 331, 1990.
- [29] Noboru Kikuchi. A smoothing technique for reduced integration penalty methods in contact problems. *International Journal for Numerical Methods in Engineering*, 18(3):343 – 350, 1982.
- [30] Naoki Asano. A penalty function type of virtual work principle for impact contact problem of two bodies. *Bulletin of the JSME*, 29(257):3701 – 3709, 1986.
- [31] J.O. Hallquist, G.L. Goudreau, and D.J. Benson. Sliding interfaces with contact-impact in large-scale Lagrangian computations. *International Journal for Numerical Methods in Engineering*, 51:107 – 137, 1985.
- [32] I. Huneke. On a penalty formulation for contact-impact problems. *Computers and Structures*, 48(2):193 – 203, 1993.
- [33] Fehmi Cirak and Matthew West. Decomposition contact response (DCR) for explicit finite element dynamics. *International Journal for Numerical Methods in Engineering*, 64(8):1078 – 1110, 2005.
- [34] S.H. Lee. Rudimentary considerations for adaptive gap/friction element based on the penalty method. *Computers and Structures*, 47(6):1043 – 1056, 1993.
- [35] L.T. Campos, J.T. Oden, and N. Kikuchi. A numerical analysis of a class of contact problems with friction in elastostatics. *Computer Methods in Applied Mechanics and Engineering*, 34(1-3):821 – 845, 1981.

- [36] G. Yagawa and H. Hirayama. A finite element method for contact problems related to fracture mechanics. *International Journal for Numerical Methods in Engineering*, 20(12):2175 – 2195, 1984.
- [37] T.J.R. Hughes, R.L. Taylor, J.L. Sackman, A. Curnier, and W. Kanoknukulchai. A finite element method for a class of contact-impact problems. *Computer Methods in Applied Mechanics and Engineering*, 8(3):249 – 276, 1976.
- [38] A. B. Chaudhary and K. J. Bathe. A solution method for static and dynamic analysis of three-dimensional contact problems with friction. *Computers and Structures*, 24(6):855 – 873, 1986.
- [39] Naoki Asano. Hybrid type of virtual work principle for impact contact problems of two bodies. *Bulletin of the JSME*, 29(252):1679 – 1684, 1986.
- [40] J.A.C. Martins and J.T. Oden. A numerical analysis of a class of problems in elastodynamics with friction. *Computer Methods in Applied Mechanics and Engineering*, 40(3):327 – 360, 1983.
- [41] Nicholas J. Carpenter, Robert L. Taylor, and Michael G. Katona. Lagrange constraints for transient finite element surface contact. *International Journal for Numerical Methods in Engineering*, 32(1):103 – 128, 1991.
- [42] Ted Belytschko and Jerry I. Lin. A three-dimensional impact-penetration algorithm with erosion. *Computers and Structures*, 25(1):95 – 104, 1987.
- [43] A. Czekanski, S.A. Meguid, N. El-Abbasi, and M.H. Refaat. On the elastodynamic solution of frictional contact problems using variational inequalities. *International Journal for Numerical Methods in Engineering*, 50(3):611 – 627, 2001.
- [44] N. Kikuchi and J. T. Oden. *Contact Problems in Elasticity: A Study of Variational Inequalities and Finite Element Methods*. SIAM, Philadelphia, 1988.
- [45] L. Jiang and R.J. Rogers. Combined Lagrangian multiplier and penalty function finite element technique for elastic impact analysis. *Computers and Structures*, 30:1219 – 1229, 1988.
- [46] T.A. Laursen and V. Chawla. Design of energy conserving algorithms for frictionless dynamic contact problems. *International Journal for Numerical Methods in Engineering*, 40(5):863 – 886, 1997.

- [47] K. Farahani, M. Mofid, and A. Vafai. A solution method for general contact-impact problems. *Computer Methods in Applied Mechanics and Engineering*, 187(1-2):69 – 77, 2000.
- [48] Z.H. Zhong. *Finite Element Procedures for Contact-Impact Problems*. Oxford University Press, Oxford, 1993.
- [49] T. A. Laursen. *Computational Contact and Impact Mechanics*. Springer, Berlin, 2002.
- [50] P. Wriggers. *Computational Contact Mechanics*. Wiley, New York, 2002.
- [51] J.T. Oden. New models of friction nonlinear elastodynamics problems. *Journal de mecanique theorique et appliquee*, 7(1):47 – 54, 1988.
- [52] E. Gerde and M. Marder. Friction and fracture. *Nature*, 413(6853):285 – 288, 2001.
- [53] Jianping Gao, W.D. Luedtke, D. Gourdon, M. Ruths, J.N. Israelachvili, and Uzi Landman. Frictional forces and amontons’ law: From the molecular to the macroscopic scale. *Journal of Physical Chemistry B*, 108(11):3410 – 3425, 2004.
- [54] C. Yang, U. Tartaglino, and B.N.J. Persson. A multiscale molecular dynamics approach to contact mechanics. *European Physical Journal E*, 19(1):47 – 58, 2006.
- [55] B.N.J. Persson, O. Albohr, F. Mancosu, V. Peveri, V.N. Samoilov, and I.M. Sivebaek. On the nature of the static friction, kinetic friction and creep. *Wear*, 254(9):835 – 851, 2003.
- [56] C. Yang, U. Tartaglino, and B.N.J. Persson. Modeling of stick-slip phenomena using molecular dynamics. *Physical Review*, B 69(205407):1 – 8, 2006.
- [57] K.L. Johnson. *Contact Mechanics*. Cambridge University Press, Cambridge, 1985.
- [58] G. M. L. Gladwell. *Contact Problems in the Classical Theory of Elasticity*. Sijthoff & Noordhoff, 1980.
- [59] Zhi-Hua Zhong and Jaroslav Mackerle. Static contact problems - a review. *Engineering computations*, 9(1):3 – 37, 1992.
- [60] Boris Petracovici. *Analysis of a spacetime discontinuous Galerkin method for elastodynamics*. PhD thesis, Department of Mathematics, University of Illinois at Urbana–Champaign, 2004.

- [61] R. L. LeVeque. *Finite Volume Methods for Hyperbolic Problems*. Cambridge University Press, 2002.
- [62] E. F. Toro. *Riemann solvers and numerical methods for fluid dynamics*. Springer, 1999.
- [63] G. Peillex, L. Baillet, and Y. Berthier. Homogenization in non-linear dynamics due to frictional contact. *International Journal of Solids and Structures*, 45(12):2451 – 2469, 2008.
- [64] P. Wriggers, L. Krstulovic-Opara, and J. Korelc. Smooth c1-interpolations for two-dimensional frictional contact problems. *International Journal for Numerical Methods in Engineering*, 51(12):1469 – 1495, 2001.
- [65] D. Dane Quinn. A new regularization of Coulomb friction. *Journal of Vibration and Acoustics, Transactions of the ASME*, 126(3):391 – 397, 2004.
- [66] Dean Karnopp. Computer simulation of stick-slip friction in mechanical dynamic systems. *Journal of Dynamic Systems, Measurement and Control, Transactions of the ASME*, 107(1):100 – 103, 1985.
- [67] N. Mostaghel and T. Davis. Representations of Coulomb friction for dynamic analysis. *Earthquake Engineering and Structural Dynamics*, 26(5):541 – 548, 1997.
- [68] Jeff Erickson, Damrong Guoy, A. Üngör, and J. Sullivan. Building spacetime meshes over arbitrary spatial domains. *Proceedings of the 11th International Meshing Roundtable*, pages 391–402, 2002.
- [69] R. Abedi, S. H. Chung, J. Erickson, Y. Fan, M. Garland, D. Guoy, R. B. Haber, J. Sullivan, S. White, and Y. Zhou. Space-time meshing with adaptive refinement and coarsening. In *Proceedings 20th Annual ACM Symposium on Computational Geometry*, pages 300–309. Association for Computing Machinery, 2004.
- [70] A. Üngör and A. Sheffer. Tent-pitcher: A meshing algorithm for space-time discontinuous Galerkin methods. In *Proceedings of the 9th International Meshing Roundtable*, pages 111–122, Sandia National Laboratories, 2000.
- [71] J. Palaniappan, S. T. Miller, and R. B. Haber. Sub-cell shock capturing and spacetime discontinuity tracking for nonlinear conservation laws. *International Journal for Numerical Methods in Fluids*, 57:1115–1135, 2008.

- [72] Yuan Zhou, Michael Garland, and Robert B. Haber. Pixel-exact rendering of spacetime finite element solutions. In *In Proceedings of IEEE Visualization 2004*, pages 425–432. Institute of Electrical and Electronics Engineers, Inc., 2004.
- [73] Zhi-Hua Zhong and L. Nilsson. Automatic contact searching algorithm for dynamic finite element analysis. *Computers and Structures*, 52(2):187 – 197, 1994.
- [74] Y.H. Yoo and M. Lee. A three-dimensional FE analysis of large deformations for impact loadings using tetrahedral elements. *Computational Mechanics*, 30(2):96 – 105, 2003.
- [75] K. Ravi-Chandar and B. Yang. On the role of microcracks in the dynamic fracture of brittle materials. *Journal of the Mechanics and Physics of Solids*, 45(4):535 – 563, 1997.
- [76] K. Ravi-Chandar. Dynamic fracture of nominally brittle materials. *International Journal of Fracture*, 90:83–102, 1998.
- [77] O. Allix and A. Corigliano. Modeling and simulation of crack propagation in mixed modes interlaminar fracture. *International Journal of Fracture*, 77:111–140, 1996.
- [78] A Corigliano and M Ricci. Rate-dependent interface models: formulation and numerical applications. *International Journal of Solids and Structures*, 38:547–576, 1999.
- [79] O. Allix, P. Feissel, and P. Thevenet. A delay damage mesomodel of laminates under dynamic loading: basic aspects and identification issues. *Computers and Structures*, 81(12):1177 – 1191, 2003.
- [80] A. Needleman. Material rate dependence and mesh sensitivity in localization problems. *Computer Methods in Applied Mechanics and Engineering*, 67(1):69 – 85, 1988.
- [81] Zdenek P. Bazant, Ted B. Belytschko, and Ta-Peng Chang. Continuum theory for strain-softening. *Journal of Engineering Mechanics*, 110(12):1666 – 1692, 1984.
- [82] G.H. Paulino, Seong Hyeok Song, and W.G. Buttlar. A bilinear cohesive zone model tailored for fracture of asphalt concrete considering viscoelastic bulk material. *Engineering Fracture Mechanics*, 73(18):2829 – 2848, 2006.
- [83] Bo Liu Jing, Shailendra K. Sharan, Wang Duo, and Yao Ling. Dynamic contact force model for contactable cracks with static and kinetic friction. *Computer Methods in Applied Mechanics and Engineering*, 123(1-4):287 – 298, 1995.

- [84] J. Dolbow, N. Moes, and T. Belytschko. An extended finite element method for modeling crack growth with frictional contact. *Computer Methods in Applied Mechanics and Engineering*, 190(51-52):6825 – 6846, 2001.
- [85] V. Tvergaard. Effect of fibre debonding in a whisker-reinforced metal. *Materials science and engineering: A*, 125:203–213, 1990.
- [86] G. Lin, P.H. Geubelle, and N.R. Sottos. Simulation of fiber debonding with friction in a model composite pushout test. *International Journal of Solids and Structures*, 38(46-47):8547 – 8562, 2001.
- [87] J. L. Chaboche, R. Girard, and A. Schaff. Numerical analysis of composite systems by using interphase/interface models. *Computational Mechanics*, A125(2):3 – 11, 1990.
- [88] Giulio Alfano and Elio Sacco. Combining interface damage and friction in a cohesive-zone model. *International Journal for Numerical Methods in Engineering*, 68(5):542 – 582, 2006.
- [89] Francesco Parrinello, Boris Failla, and Guido Borino. Cohesive-frictional interface constitutive model. *International Journal of Solids and Structures*, 46(13):2680 – 2692, 2009.
- [90] E. Sharon and J. Fineberg. Microbranching instability and the dynamic fracture of brittle materials. *Physical Review B*, 54(10):7128–7139, 1996.
- [91] E. Sharon, S.P. Gross, and J. Fineberg. Energy dissipation in dynamic fracture. *Phys. Rev. Lett.*, 76:2117, 1996.
- [92] N. Murphy, M. Ali, and A. Ivankovic. Dynamic crack bifurcation in pmma. *Engineering Fracture Mechanics*, 73(16):2569 – 2587, 2006.
- [93] N. Moes, J. Dolbow, and T. Belytschko. A finite element method for crack growth without remeshing. *International Journal for Numerical Methods in Engineering*, 46:131–150, 1999.
- [94] J. J. C. Remmers, Rene de Borst, and A. Needleman. A cohesive segments method for the simulation of crack growth. *Computational Mechanics*, 31:69–77, 2003.
- [95] P.M.A. Areias and T. Belytschko. Analysis of three-dimensional crack initiation and propagation using the extended finite element method. *International Journal for Numerical Methods in Engineering*, 63(5):760 – 788, 2005.

- [96] T. Strouboulis, I. Babuška, and K. Copps. The design and analysis of the generalized finite element method. *Computer Methods in Applied Mechanics and Engineering*, 181:43–69, 2000.
- [97] T. Strouboulis, K. Copps, and I. Babuška. The generalized finite element method. *Computer Methods in Applied Mechanics and Engineering*, 190:4081–4193, 2001.
- [98] C. Linder and F. Armero. Finite elements with embedded strong discontinuities for the modeling of failure in solids. *International Journal for Numerical Methods in Engineering*, 72(12):1391 – 1433, 2007.
- [99] C. Linder and F. Armero. Finite elements with embedded branching. *Finite Elements in Analysis and Design*, 45(4):280 – 293, 2009.
- [100] Gabriella Bolzon and Alberto Corigliano. Finite elements with embedded displacement discontinuity: a generalized variable formulation. *International Journal for Numerical Methods in Engineering*, 49(10):1227 – 1266, 2000.
- [101] Z. Y. Zhang and G. H. Paulino. Cohesive zone modeling of dynamic failure in homogeneous and functionally graded materials. *International Journal of Plasticity*, 21:1195–1254, 2005.
- [102] Glaucio H. Paulino, Waldemar Celes, Rodrigo Espinha, and Zhengyu Jenny Zhang. A general topology-based framework for adaptive insertion of cohesive elements in finite element meshes. *Engineering with Computers*, 24(1):59 – 78, 2008.
- [103] S.B. Biner. A FEM analysis of crack growth in microcracking brittle solids. *Engineering Fracture Mechanics*, 51(4):555 – 573, 1995.
- [104] D.W. Nicholson, P. Ni, and Y. Ahn. Probabilistic theory for mixed mode fatigue crack growth in brittle plates with random cracks. *Engineering Fracture Mechanics*, 66(3):305 – 200, 2000.
- [105] J. Palaniappan, Robert B. Haber, and R. L. Jerrard. A spacetime discontinuous Galerkin method for scalar conservation laws. *Computer Methods in Applied Mechanics and Engineering*, 193:3607–3631, 2004.
- [106] S. T. Miller and R. B. Haber. A spacetime discontinuous Galerkin method for hyperbolic heat conduction. *Computer Methods in Applied Mechanics and Engineering*, 198:194–209, 2008.
- [107] O Miller, L. B. Freund, and A. Needleman. Energy dissipation in dynamic fracture of brittle materials. *Modelling and Simulation in Materials Science and Engineering*, 7:573 – 586, 1999.

- [108] Zhengyu Zhang, G.H. Paulino, and W. Celes. Extrinsic cohesive modelling of dynamic fracture and microbranching instability in brittle materials. *International Journal for Numerical Methods in Engineering*, 72(8):893 – 923, 2007.
- [109] K. Arakawa and K. Takahashi. Relationships between fracture parameters and fracture surface roughness of brittle polymers. *International Journal of Fracture*, 48(2):103 – 114, 1991.
- [110] Huajian Gao. Surface roughening and branching instabilities in dynamic fracture. *Journal of the Mechanics and Physics of Solids*, 41(3):457 – 486, 1993.
- [111] K. Uenishi and H.P. Rossmanith. Stability of dynamically propagating cracks in brittle materials. *Acta Mechanica*, 156(3-4):179 – 192, 2002.
- [112] O. S. Lawlor, S. Chakravorty, T. L. Wilmarth, N. Choudhury, I. Doolley, Gengbin Zheng, and L. V. Kale. ParFUM: a parallel framework for unstructured meshes for scalable dynamic physics applications. *Engineering with Computers*, 22:215–35, 2006.
- [113] Gengbin Zheng. *Achieving High Performance on Extremely Large Parallel Machines: Performance Prediction and Load Balancing*. PhD thesis, Department of Computer Science, University of Illinois at Urbana-Champaign, 2005.
- [114] A.L. Gurson. Continuum theory of ductile rupture by void nucleation and growth: Part 1 - yield criteria and flow rules for porous ductile media. *Journal of Engineering Materials and Technology, Transactions of the ASME*, 99 Ser H(1):2 – 15, 1977.